An Idealised Morphodynamic Model of a Tidal Inlet and the Adjacent Sea

by

Marco Pieter Rozendaal

to obtain the degree of Master of Science
at the Delft University of Technology,
to be defended publicly on Friday August 30, 2019 at 11:30 AM.

Student number:	4377710	
Project duration:	December 10, 2018 – August 30, 2019	
Thesis committee:	Dr. H.M. Schuttelaars,	TU Delft, supervisor
	Dr. J.L.A. Dubbeldam,	TU Delft
	Dr. M. Möller,	TU Delft

Abstract

Tidal inlet systems are often highly valuable and sometimes even unique ecosystems. However, field measurements show that tidal inlet systems are sensitive to changing exogenous conditions, such as rising sea levels. This thesis aims to investigate to what extent the adjacent sea influences the stability and equilibrium state of the tidal inlet. A one-dimensional idealised model is used to model the interaction between the sea and the inlet. The water motion is forced by the tide and the inlet is assumed to be narrow and short. At equilibrium, an increasingly sloping bottom is found in the sea and a constantly sloping bottom in the inlet. This equilibrium bottom profile seems to be in reasonable agreement with observations. The sea-inlet bottom profile is less stable than the inlet bottom profile, nevertheless, the sea-inlet bottom profile is still asymptotically linear stable. Moreover, the results in this thesis suggest that for one-dimensional idealised models consisting solely of a tidal inlet, the correct seaward boundary condition is a properly chosen fixed entrance depth. For a two-dimensional semi-infinite sea, it is shown that a Perfectly Matched Layer is a convenient method to incorporate the Sommerfeld radiation condition and that the narrow tidal inlet cannot be modelled as a point source forcing in the two-dimensional sea domain.

Preface

When I was little, I loved building sandcastles. During our summer holidays, I would be digging for hours on end. Something about the interaction between the sandcastle and the waves always fascinated me. During this master project, I got the opportunity to study the interaction between the beach and the sea once again, but this time from a theoretical point of view. In this thesis, I develop an idealised morphodynamic model to study the interaction between a tidal inlet and the adjacent sea. This thesis is written in partial fulfillment of the requirements of the master Applied Mathematics at Delft, University of Technology, the Netherlands.

Here, I would like to thank a few people that were important during my nine-month master project.

First of all, I would like to express my gratitude to my supervisor, Henk. Without you, this project would not have been such a wonderful experience. Your endless enthusiasm, critical attitude and expertise always motivated me and pushed me to seek a better explanation. Whenever I was stuck, I could always hop by your office to get advice or brainstorm about new ideas.

Furthermore, I would like to thank my study friends, Carlos, Massimo, Mike, Pieter, Rick and Roel, for the numerous card games played during the lunch break and for listening when something did not work as expected. In particular, I would like to thank Massimo and Mike for proofreading my thesis and for their helpful suggestions.

Finally, I would like to thank my parents and my sister for their unconditional love and support.

Delft, August 2019

Contents

Chapter 1

Introduction

1.1 Morphodynamics

> Who has not built a sandcastle on the beach? You pick a nice spot, just before the waterline, and start digging. Once a big wave forms, you hope that your caste is large enough to survive the impending wave. Yes, it survived and you keep on digging. When you are finally done (is a sandcastle ever done?) the water line is miles away from your handmade structure and you get bored. You start swimming and once you come back, your almighty castle is swallowed by the sea and you are left with only a shadow of your former masterpiece. The next day, you come back to rebuild your empire but you cannot find the remains and conclude that it is gone.

This example nicely illustrates the interaction between the beach, the waves and the tides. Predicting what happens to the sandcastle in a day or two is not too difficult, but how about predicting what the beach looks like in one, ten or a hundred years? Or, how the sea level rise affects the seabed and shorelines? Morphodynamics is the study of the interaction between and the response of the seabed topology and the fluid hydrodynamics[1] (Wright and Thom, 1977). It is the study of oceanic landscape changes due to erosion and sedimentation. The seabed morphodynamics is affected by the wind, waves, currents, tides, storms, local bed slope and human activities, to name a few.

Morphodynamic models are used to study the landscape changes of coastal systems. In this thesis, we focus on process-based morphodynamic models, however several model types have been proposed (see Section 1.3 for an overview of these model types). A process-based morphodynamic model usually consists of three modules: a hydrodynamic module, a sediment transport module and a bed evolution module. In the first module, the water motion is resolved for a given bed topology. In the second module, the sediment transport is calculated using the known hydrodynamics and in the last module, the calculated sediment transport is used to update the bed topology. The new bed topology is utilized in the first module to calculate the water motion again. This is known as the morphodynamic loop and is illustrated in Figure 1.1.

In this thesis, tidal inlet systems are studied and, in particular, their morphodynamic evolution towards equilibrium. In the next section, tidal inlet systems are introduced and their importance is highlighted.

1.2 Tidal inlet systems

About 12% of the world's coastline can be characterized as barrier islands separated by tidal inlets (Glaeser, 1978). Examples include the Dutch, German and Danish Wadden coast (Ehlers, 1988), the

[1] The term morphodynamics is not uniquely defined. In other scientific realms, the term morphodynamics may have a different notion associated to it (Syvitski *et al.*, 2010, p. 1).

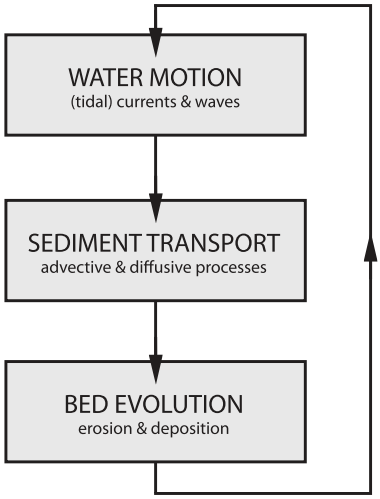

Figure 1.1: The morphodynamic loop. Courtesy of Ter Brake (2011).

United States' east coast (Hayes, 1980) and the barrier coast of New Zealand (Hicks *et al.*, 1999). Tidal inlets are typically found along sandy coasts (Glaeser, 1978).

Tidal inlets can be defined as semi-enclosed coastal bodies of water where the water motion is predominately driven by tides. A schematic representation of a tidal inlet system is shown in Figure 1.2. For example, one could think of the Ameland inlet system, where the barrier islands are Terschelling and Ameland respectively, see also Figure 3.2. A tidal inlet system, in principle, consists of three main components: a sea, an inlet (strait) and a basin. During flood tide, seawater flows, mostly via the seaward marginal flood channels (located in between the barrier islands and the ebb-tidal delta), through the inlet into the basin. At the entrance of the basin, a shallow flood-delta is formed and inside the basin, a complex network of channels and shoals is often present. In general, the depth of the fractal channel structure decreases towards the beach (Hayes, 1980). During ebb tide, water flows out of the basin, through the inlet into the sea again. The seawards current creates a deep ebb channel in the sea which transitions into a large, shallow, ebb-tidal delta. The basin is either semi-enclosed by land or surrounded by watersheds and a coast as depicted in Figure 1.2.

Tidal inlets systems are often highly valuable and sometimes even unique ecosystems (De Vriend *et al.*, 2002). They act as breeding and nursery grounds for fish and as resting and feeding grounds for many other species, including migratory birds (De Jonge *et al.*, 1993). Tidal inlet systems are also important for the stability of the surrounding shoreline since tidal inlets strongly influence the sediment budget of the coast (FitzGerald, 1988). Moreover, tidal inlets attract a host of human activities, such as navigation, recreation, fishing, sand mining, land reclamation and mineral extraction (De Vriend *et al.*, 2002).

1.3 Morphodynamic model types

Due to the complexity and vast variety of tidal inlets and the processes observed within them, a multitude of approaches have been employed to study tidal inlets. De Vriend (1996) proposed the following classification of the various model approaches:

- *Data-based models* use measurements only to describe the observed phenomena.
- *Empirical relationships and empirical models* use statistical relationships between different state variables, derived from the analysis of field data.
- *Semi-empirical long-term models* describe the dynamic interaction between large elements of the system, using empirical relationships to represent the effects of smaller-scale processes.
- *Process-based models* are mathematical models based on first physical principles.

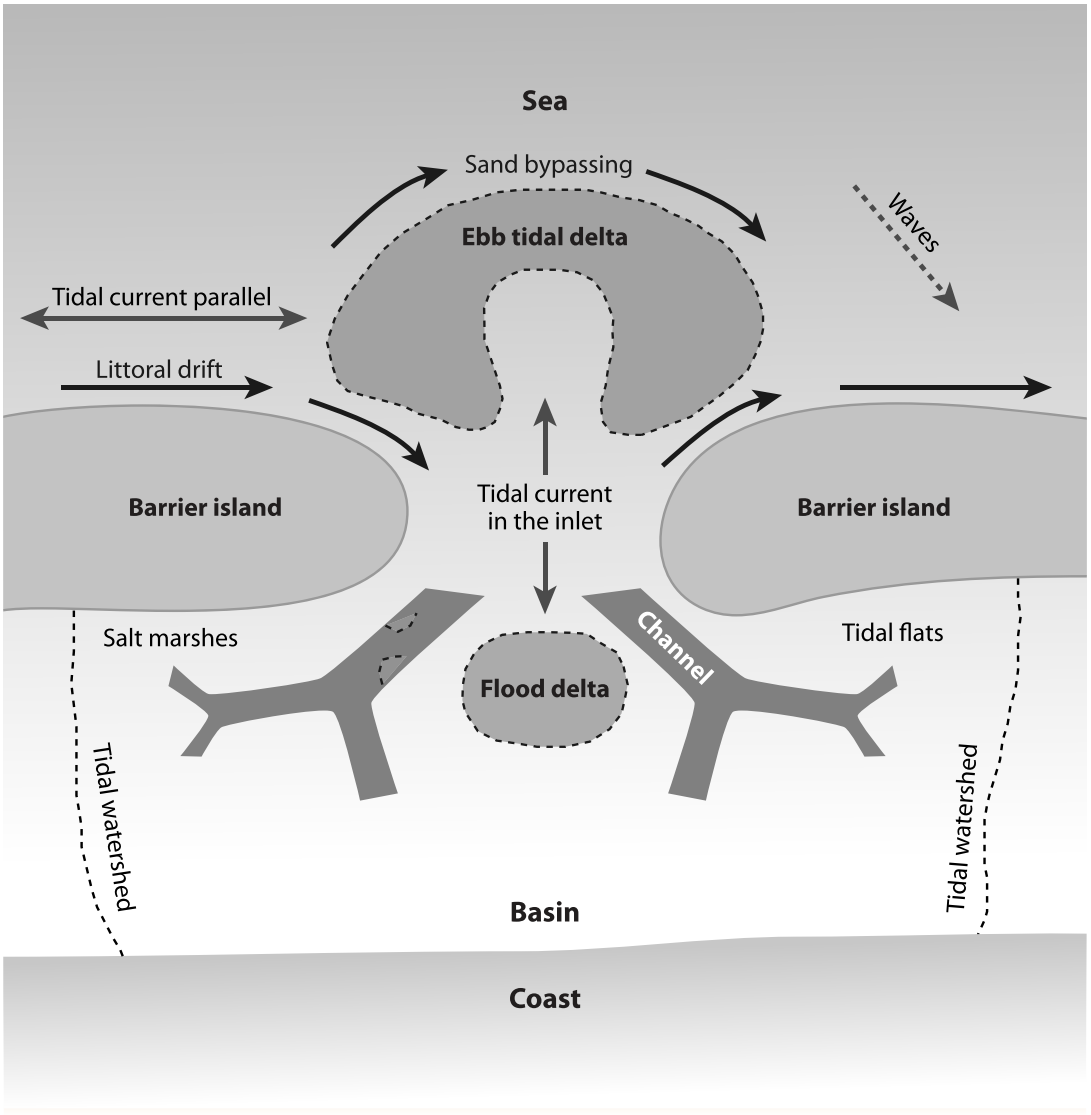

Figure 1.2: Sketch of an idealised tidal inlet system and the dominant physical processes. Adaptation based on De Swart and Zimmerman (2009)

- *Formally integrated long-term models* or *idealised models* are derived from the process-based models by formal integration over time (and space), with possible empirical or parametric closure relations and simplified geometries.

Mathematical modelling using conservation laws belongs to the latter two classes. *Process-based models* use complex state-of-the-art model formulations. These models have successfully been used to predict the formation of channels and shoals in tidal inlets (Roelvink, 2006). However, these complex process-based models cannot be used to perform sensitivity or bifurcation analysis since even a single model run towards morphodynamic equilibrium is very time-consuming. Furthermore, the complex process-based models are too complicated to determine which physical processes are responsible for the simulated behaviour. *Formally integrated long-term models* retain only those processes that are relevant for the studied phenomena. As a result, idealised models cannot be used to simulate the exact evolution of any specific tidal inlet. Instead, idealised models are the perfect tool to gain insight into which processes are responsible for the commonly observed phenomena within tidal inlets. In this thesis, an idealised model approach is adopted.

1.4 Current research

Motivated by the method of formal averaging described by Krol (1990) and the numerical results of Van Dongeren and De Vriend (1994), Schuttelaars and De Swart (1996) developed an idealised one-dimensional morphodynamic model for a short, semi-enclosed, tidal embayment. The water motion is forced by the tide at the seaward side and a fixed depth is prescribed at the entrance of the embayment. It was found that the system has a unique morphodynamic equilibrium for all parameter values. The morphodynamic equilibria found were consistent with observed bottom profiles in the short embayments of the Dutch Wadden Sea (De Swart and Blaas, 1998). Later, Schuttelaars and De Swart (2000) have extended this model to include longer embayments and the derived bottom profiles were overall in good agreement with field observations.

However, what these idealised models fail to address is the interaction of the embayment with the adjacent sea. In these idealised models, simple boundary conditions at the basin entrance are imposed, but it is important to study to what extent the processes occurring in the adjacent sea influence the hydrodynamics and, therefore, the morphodynamics of the embayment. In Van Leeuwen (2002) the sea-basin interaction is investigated using a two-dimensional complex morphodynamic model. The geometry consists of a rectangular sea, that is connected via a small strait to a rectangular basin. It was found that the alongshore travelling tidal wave has a significant influence on the residual flow patterns in the basin. In Ter Brake (2011) a different approach is adopted, using the one-dimensional idealised model. Instead of extending the domain into the sea, the effect of imposing different seaward boundary conditions is investigated. It was found that changing the seaward boundary condition strongly influenced the shape and number of possible equilibrium bottom profiles.

Although the interaction between the adjacent sea and the basin has been studied, many of the dynamics are still poorly understood in terms of physical mechanisms and the exact implications for idealised morphodynamic models remains unclear. Hence, further research into this interaction is called for, which leads to the main research questions of this thesis:

***Q1**: How does the adjacent sea affect the stability and equilibrium state of the tidal inlet system?*

***Q2**: What are the correct seaward boundary conditions for one-dimensional idealised models consisting solely of an embayment?*

***Q3**: Can a narrow tidal inlet be modelled as a point source forcing in a two-dimensional semi-infinite sea domain?*

1.5 Thesis structure

To be able to answer the research questions posed in the previous section, the following research approach and thesis structure are adopted. In Chapter 2, the shallow water equations, which govern the fluid flow in coastal areas, are derived by formally integrating the full three-dimensional Navier-Stokes equations. In Chapter 3, a detailed derivation of the morphodynamics of a one-dimensional idealised tidal embayment is presented. This chapter follows along the lines of Schuttelaars and De Swart (1996). In Chapter 4, the morphodynamics of a one-dimensional sea-basin system is analysed. To this end, the boundary at the entrance of the basin is replaced by a boundary located inside the sea, far away from the inlet entrance. The different sea dynamics are parametrised within the context of this one-dimensional model. Lastly in Chapter 5, the morphodynamics of a two-dimensional semi-infinite sea and a one-dimensional basin are analysed. The narrow embayment is modelled as a point source forcing in the two-dimensional sea domain.

Chapter 2

Derivation of the shallow water equations

In this chapter, the shallow water equations are derived. The three-dimensional shallow water equations are derived from the three-dimensional Navier-Stokes equations. The three-dimensional shallow water equations are integrated over the depth to obtain the two-dimensional shallow water equations. Finally, the one-dimensional shallow water equations are derived from the two-dimensional shallow water equations by averaging over the channel width.

2.1 Derivation of the three-dimensional water equations

In this section, the unsteady Reynolds Averaged Navier-Stokes (RANS) equations, which govern fluid flow, are derived using Reynolds decomposition. Then the three-dimensional shallow water equations are derived from the RANS equations under the assumption of shallow water.

2.1.1 The unsteady Reynolds Averaged Navier-Stokes equations

The flow is assumed to be incompressible, i.e., the effects of density differences are ignored. The incompressible continuity equation is used to represent the conservation of mass and the Navier-Stokes equations are used to represent the conservation of momentum. The incompressible continuity equation and the Navier-Stokes equations in convective form are respectively given by

$$\begin{cases} \dfrac{\partial u}{\partial x} + \dfrac{\partial v}{\partial y} + \dfrac{\partial w}{\partial z} = 0, & \text{(2.1.1a)} \\ \dfrac{\partial u}{\partial t} + u\dfrac{\partial u}{\partial x} + v\dfrac{\partial u}{\partial y} + w\dfrac{\partial u}{\partial z} + f_* w - fv = -\dfrac{1}{\rho}\dfrac{\partial p}{\partial x} + \nu\left(\dfrac{\partial^2 u}{\partial x^2} + \dfrac{\partial^2 u}{\partial y^2} + \dfrac{\partial^2 u}{\partial z^2}\right), & \text{(2.1.1b)} \\ \dfrac{\partial v}{\partial t} + u\dfrac{\partial v}{\partial x} + v\dfrac{\partial v}{\partial y} + w\dfrac{\partial v}{\partial z} + fu = -\dfrac{1}{\rho}\dfrac{\partial p}{\partial y} + \nu\left(\dfrac{\partial^2 v}{\partial x^2} + \dfrac{\partial^2 v}{\partial y^2} + \dfrac{\partial^2 v}{\partial z^2}\right), & \text{(2.1.1c)} \\ \dfrac{\partial w}{\partial t} + u\dfrac{\partial w}{\partial x} + v\dfrac{\partial w}{\partial y} + w\dfrac{\partial w}{\partial z} - f_* u = -\dfrac{1}{\rho}\dfrac{\partial p}{\partial z} + \nu\left(\dfrac{\partial^2 w}{\partial x^2} + \dfrac{\partial^2 w}{\partial y^2} + \dfrac{\partial^2 w}{\partial z^2}\right) - g, & \text{(2.1.1d)} \end{cases}$$

where u, v and w are the flow velocities in the three Cartesian dimensions, ρ is the fluid density, p is the pressure, ν is the kinematic viscosity and g is the gravitational acceleration, which is assumed to be constant. Furthermore, $f = 2\Omega \sin\varphi$ is the Coriolis parameter and $f_* = 2\Omega \cos\varphi$ is the reciprocal Coriolis parameter with Ω the angular velocity of earth and φ the geographic latitude, which is positive in the northern hemisphere and negative in the southern hemisphere. The variables u, v, w and p are functions of the three Cartesian dimensions and time, i.e. they depend on x, y, z and t. For the present form of

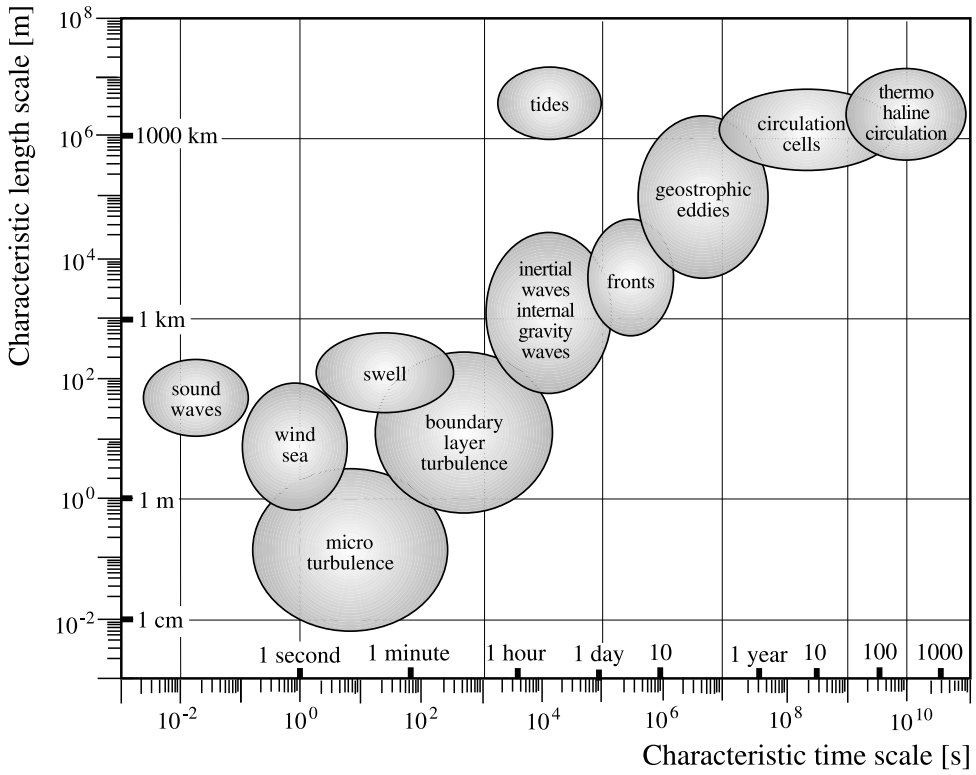

Figure 2.1: Temporal and spatial scales of typical oceanic processes. Adaptation based on Burchard (2002).

the Coriolis force to be valid, the local Cartesian coordinate system has to be orientated such that the positive x, y and z axis point eastward, northward and upward respectively.

The current form of the equations allows turbulent flow to occur. Turbulent flow is characterised by chaotic changes in pressure and velocity at a wide range of length and time scales. The temporal and spatial length scales for typical processes in the ocean are shown in Figure 2.1. A small perturbation of the initial condition is sufficient to cause significantly different flow due to the highly complex flow patterns exhibited by turbulent flow. We are not interested in simulating these turbulent fluctuations, instead, we are interested in the statistically averaged flow. To this end, Reynolds decomposition is used. Following Pedlosky (1987), it is assumed that there exists an average[1], denoted with $\langle \cdot \rangle$, such that the flow u can be decomposed into a mean part $\langle u \rangle$, which represents the large-scale flow, and a fluctuating part u', which represents the smaller-scale turbulent flow:

$$u = \langle u \rangle + u',$$

such that the average of the fluctuating part vanishes, i.e.,

$$\langle u' \rangle = 0.$$

The following four properties should hold for this averaging procedure

$$\langle \langle u \rangle \rangle = \langle u \rangle, \qquad \langle u + v \rangle = \langle u \rangle + \langle v \rangle, \qquad \langle \langle u \rangle v \rangle = \langle u \rangle \langle v \rangle, \qquad \left\langle \frac{\partial u}{\partial s} \right\rangle = \frac{\partial}{\partial s} \langle u \rangle, \tag{2.1.2}$$

where s can be any of the spatial variables or the temporal variable. Averaging the continuity equation (2.1.1a) and using the Reynolds decomposition shows that the averages satisfy the continuity equation

$$\frac{\partial \langle u \rangle}{\partial x} + \frac{\partial \langle v \rangle}{\partial y} + \frac{\partial \langle w \rangle}{\partial z} = 0. \tag{2.1.3}$$

[1]The only average that satisfies the four properties given in equation (2.1.2) is the ensemble average, the average over infinitely many realisations for each x, y, z and t. However using the ergodic assumption, stationary and homogeneous turbulence, the ensemble average may be replaced by a spatial or temporal average (Burchard, 2002, p. 17).

The x component of the Navier-Stokes equations can be written in conservative form by adding the continuity equation (2.1.1a) multiplied with u and using the product rule backwards. The conservative form of the conservation of momentum in the x dimension, equation (2.1.1b), is found to be

$$\frac{\partial u}{\partial t} + \frac{\partial}{\partial x}\left(u^2\right) + \frac{\partial}{\partial y}(uv) + \frac{\partial}{\partial z}(uw) + f_* w - fv = -\frac{1}{\rho}\frac{\partial p}{\partial x} + \nu\left(\frac{\partial^2 u}{\partial x^2} + \frac{\partial^2 u}{\partial y^2} + \frac{\partial^2 u}{\partial z^2}\right). \tag{2.1.4}$$

Applying the averaging procedure to this equation and substitution of the Reynolds decomposition for each variable yields

$$\begin{aligned}\frac{\partial \langle u\rangle}{\partial t} + \frac{\partial}{\partial x}\langle u\rangle^2 + \frac{\partial}{\partial y}\langle u\rangle\langle v\rangle + \frac{\partial}{\partial z}\langle u\rangle\langle w\rangle + f_*\langle w\rangle - f\langle v\rangle \\ = -\frac{1}{\rho}\frac{\partial \langle p\rangle}{\partial x} + \nu\left(\frac{\partial^2\langle u\rangle}{\partial x^2} + \frac{\partial^2\langle u\rangle}{\partial y^2} + \frac{\partial^2\langle u\rangle}{\partial z^2}\right) - \frac{\partial}{\partial x}\langle u'^2\rangle - \frac{\partial}{\partial y}\langle u'v'\rangle - \frac{\partial}{\partial z}\langle u'w'\rangle.\end{aligned}$$

The unsteady Reynolds averaged equations are obtained after expanding the convective derivatives, using the averaged continuity equation (2.1.3) and rewriting the viscous diffusive terms as

$$\begin{aligned}\frac{\partial \langle u\rangle}{\partial t} + \langle u\rangle\frac{\partial\langle u\rangle}{\partial x} + \langle v\rangle\frac{\partial\langle u\rangle}{\partial y} + \langle w\rangle\frac{\partial\langle u\rangle}{\partial z} + f_*\langle w\rangle - f\langle v\rangle \\ = -\frac{1}{\rho}\frac{\partial\langle p\rangle}{\partial x} + \frac{\partial}{\partial x}\left(\nu\frac{\partial\langle u\rangle}{\partial x} - \langle u'^2\rangle\right) + \frac{\partial}{\partial y}\left(\nu\frac{\partial\langle u\rangle}{\partial y} - \langle u'v'\rangle\right) + \frac{\partial}{\partial z}\left(\nu\frac{\partial\langle u\rangle}{\partial z} - \langle u'w'\rangle\right).\end{aligned}$$

After averaging the momentum equations, six terms still depend on the unknown turbulent fluctuations, namely $\langle u'^2\rangle$, $\langle v'^2\rangle$, $\langle w'^2\rangle$, $\langle u'v'\rangle$, $\langle u'w'\rangle$ and $\langle v'w'\rangle$. These unknown terms are called the Reynolds stresses. Thus there are three equations for nine unknowns. The discrepancy between the number of unknowns and the number of equations is known as the Turbulence Closure Problem.

It is possible to derive partial differential equations for the Reynolds stresses from the conservation of momentum equations, the so-called Reynold Stress Equations. The problem is that when deriving the Reynold Stress Equations new unknowns arise, like the third moment fluctuating terms $\langle u'v'w'\rangle$, $\langle u'^2v'\rangle$, $\langle u'v'^2\rangle$ etcetera. New equations for these new terms can be derived, but the number of unknowns grows faster than the number of equations. Thus at some point, a closing hypothesis is needed, in which the highest moment fluctuating terms are parametrised in terms of the lower-order terms, in order to obtain a closed set of equations.

Here a First-Order Closure is chosen, where the Reynolds stresses are directly parametrised in terms of the mean flow variables. Turbulent flow consists of eddies, which consist of smaller eddies and so on until the eddies are small enough for the energy to be dissipated by the viscosity of the fluid. In light of this energy cascade, it seems reasonable to assume that turbulence acts as energy dissipation and can be parametrised as additional viscosity. Hence

$$\begin{aligned}&\langle u'^2\rangle = -2A_\mathrm{h}\frac{\partial\langle u\rangle}{\partial x}, && \langle v'^2\rangle = -2A_\mathrm{h}\frac{\partial\langle v\rangle}{\partial y}, && \langle w'^2\rangle = -2A_\mathrm{v}\frac{\partial\langle w\rangle}{\partial z}, \\ &\langle u'v'\rangle = -A_\mathrm{h}\left(\frac{\partial\langle u\rangle}{\partial y} + \frac{\partial\langle v\rangle}{\partial x}\right), && \langle u'w'\rangle = -A_\mathrm{v}\frac{\partial\langle u\rangle}{\partial z} - A_\mathrm{h}\frac{\partial\langle w\rangle}{\partial x}, && \langle v'w'\rangle = -A_\mathrm{v}\frac{\partial\langle v\rangle}{\partial z} - A_\mathrm{h}\frac{\partial\langle w\rangle}{\partial y}.\end{aligned}$$

Here, $A_\mathrm{h}, A_\mathrm{v}$ are respectively the horizontal and vertical eddy viscosity coefficients. This is the so-called eddy viscosity parametrisation of the Reynolds stresses. A distinction is made between the horizontal and vertical eddy viscosity coefficient because the turbulent motion is, in general, much larger in the horizontal dimension than in the vertical dimension (Cushman-Roisin and Beckers, 2009). The eddy viscosity terms generally depend on the expected turbulence, time and location. Even though the turbulent fluctuations are not explicitly resolved, this system of equations is used successfully to reproduce observed geophysical flows and provides a simple way to close the system of equations with minimal increase in computation time (Pedlosky, 1987; Vreugdenhil, 1994).

Substitution of the eddy viscosity parametrisation and using the averaged continuity equation (2.1.3)

gives

$$\frac{\partial\langle u\rangle}{\partial t}+\langle u\rangle\frac{\partial\langle u\rangle}{\partial x}+\langle v\rangle\frac{\partial\langle u\rangle}{\partial y}+\langle w\rangle\frac{\partial\langle u\rangle}{\partial z}+f_*\langle w\rangle-f\langle v\rangle$$
$$=-\frac{1}{\rho}\frac{\partial\langle p\rangle}{\partial x}+\frac{\partial}{\partial x}\left((\nu+A_{\mathrm{h}})\frac{\partial\langle u\rangle}{\partial x}\right)+\frac{\partial}{\partial y}\left((\nu+A_{\mathrm{h}})\frac{\partial\langle u\rangle}{\partial y}\right)+\frac{\partial}{\partial z}\left((\nu+A_{\mathrm{v}})\frac{\partial\langle u\rangle}{\partial z}\right).$$

An effective eddy viscosity coefficient that captures both the viscosity effects of the fluid itself and the viscosity due to the turbulent fluctuations is defined as

$$\mathcal{A}_{\mathrm{h}}=\nu+A_{\mathrm{h}}\qquad\text{and}\qquad\mathcal{A}_{\mathrm{v}}=\nu+A_{\mathrm{v}}.$$

The right angled brackets are omitted for notational convenience but it should be understood that the average operator still applies in the remainder of this thesis. The derivation of the momentum equations for the y and z direction is similar to that of the x direction and is omitted for brevity. The Reynolds averaged continuity equation and the unsteady Reynolds Averaged Navier-Stokes equations are given by

$$\begin{cases}\dfrac{\partial u}{\partial x}+\dfrac{\partial v}{\partial y}+\dfrac{\partial w}{\partial z}=0, & \text{(2.1.5a)}\\[2ex] \dfrac{\partial u}{\partial t}+u\dfrac{\partial u}{\partial x}+v\dfrac{\partial u}{\partial y}+w\dfrac{\partial u}{\partial z}+f_*w-fv=-\dfrac{1}{\rho}\dfrac{\partial p}{\partial x}+\dfrac{\partial}{\partial x}\left(\mathcal{A}_{\mathrm{h}}\dfrac{\partial u}{\partial x}\right)+\dfrac{\partial}{\partial y}\left(\mathcal{A}_{\mathrm{h}}\dfrac{\partial u}{\partial y}\right)+\dfrac{\partial}{\partial z}\left(\mathcal{A}_{\mathrm{v}}\dfrac{\partial u}{\partial z}\right), & \text{(2.1.5b)}\\[2ex] \dfrac{\partial v}{\partial t}+u\dfrac{\partial v}{\partial x}+v\dfrac{\partial v}{\partial y}+w\dfrac{\partial v}{\partial z}+fu=-\dfrac{1}{\rho}\dfrac{\partial p}{\partial y}+\dfrac{\partial}{\partial x}\left(\mathcal{A}_{\mathrm{h}}\dfrac{\partial v}{\partial x}\right)+\dfrac{\partial}{\partial y}\left(\mathcal{A}_{\mathrm{h}}\dfrac{\partial v}{\partial y}\right)+\dfrac{\partial}{\partial z}\left(\mathcal{A}_{\mathrm{v}}\dfrac{\partial v}{\partial z}\right), & \text{(2.1.5c)}\\[2ex] \dfrac{\partial w}{\partial t}+u\dfrac{\partial w}{\partial x}+v\dfrac{\partial w}{\partial y}+w\dfrac{\partial w}{\partial z}-f_*u=-\dfrac{1}{\rho}\dfrac{\partial p}{\partial z}+\dfrac{\partial}{\partial x}\left(\mathcal{A}_{\mathrm{h}}\dfrac{\partial w}{\partial x}\right)+\dfrac{\partial}{\partial y}\left(\mathcal{A}_{\mathrm{h}}\dfrac{\partial w}{\partial y}\right)+\dfrac{\partial}{\partial z}\left(\mathcal{A}_{\mathrm{v}}\dfrac{\partial w}{\partial z}\right)-g. & \text{(2.1.5d)}\end{cases}$$

Comparing the unsteady Reynolds Averaged Navier-Stokes equations to the incompressible Navier-Stokes equations (2.1.1b–d) shows that only the viscosity terms are altered. Furthermore, it should be noted that all the variables are replaced with their respective Reynolds average.

2.1.2 The three-dimensional shallow water equations

The Reynolds Averaged Navier-Stokes equations are simplified for large-scale geophysical flow using scaling analysis. Thereafter, the three-dimensional shallow water equations are derived in the case of shallow water.

Dominating horizontal flow

It can be the case that not all terms in an equation are equally important. That is to say, there are terms which are 'larger' than the other terms in an equation. There can be one largest term or several similarly large terms. Considering only the largest terms in an equation results in a new equation. This new equation is often a simpler version of the original equation and is called a balance, as the sides of this simpler equation should cancel against each other. The balance with the largest magnitude is called the leading order balance or dominant balance. Not all balances are allowed and finding a dominant balance can be a difficult task if the equation contains many terms.

For geophysical flow, the flow and length scales found in the horizontal plane, that is in the x and y directions, are comparable. The flow and length scale found in the vertical direction, z, are fundamentally different by, respectively, the presence of the gravity term in equation (2.1.5d) and the boundedness of the vertical domain by the seabed and free surface. Thus, a horizontal length scale L, vertical length scale H, horizontal flow velocity U and a vertical flow velocity W are introduced.

Using the characteristic scales, the scaling of the Reynolds averaged continuity equation (2.1.5a) is given by

$$\begin{matrix}\dfrac{\partial u}{\partial x}+\dfrac{\partial v}{\partial y}+\dfrac{\partial w}{\partial z}=0.\\[2ex] \dfrac{U}{L}\quad\dfrac{U}{L}\quad\dfrac{W}{H}\end{matrix}$$

The dominant balance of the continuity equation for geophysical flow can now be determined. There are three cases to consider:

1. $U/L \ll W/H$: Then the leading order balance is given by $\partial w/\partial z = 0$. Thus the vertical flow is constant in z, i.e. $w = w(x, y)$. Water cannot flow through the seabed or sea surface, hence water cannot come from or escape via these boundaries. It follows that the water needed to supply this vertical flow needs to come from the sides. However, the horizontal water motion is assumed to be small and can, therefore, not supply this mainly vertical flow of water. Thus, this case is infeasible.
2. $U/L \sim W/H$: For this case the dominant balance is given by $\partial u/\partial x + \partial v/\partial y + \partial w/\partial z = 0$. Thus the dominant balance is a three-way balance. This balance is very general and this case is feasible.
3. $U/L \gg W/H$: The leading order balance is given by $\partial u/\partial x + \partial v/\partial y = 0$. Thus, the water flow in one horizontal direction is compensated by the water flow in the perpendicular horizontal direction. This case is feasible as long as the bottom variations are small compared to the water depth. However, for coastal areas, the seabed changes over the whole water depth H. The kinematic boundary condition (2.2.3), which is explained in the next section, then implies the balance $W \sim UH/L$, since $\partial h/\partial t$ is very small (as the bed changes on a very long time scale). This balance contradicts our assumption that $W \ll UH/L$, which makes this case infeasible.

In conclusion, the only feasible dominant balance for significantly changing bottom profiles is case 2, which can be rewritten as

$$W \sim \frac{H}{L} U.$$

For geophysical flow, the horizontal length scale L is much larger than the vertical length scale H. Hence the water can be considered shallow, in the sense that the ratio of the vertical length scale H to the horizontal length scale L is small, i.e. $H/L \ll 1$. Using that the water is shallow, it follows that

$$W \ll U.$$

Thus for shallow water, the flow is mainly horizontal.

The three-dimensional shallow water equations

For shallow water, the flow in the vertical dimension w is small, as shown in the previous section. An order of magnitude analysis of the momentum equation in the z dimension (2.1.5d) shows that the dominant balance is given by the hydrostatic balance:

$$\frac{\partial p}{\partial z} = -\rho g.$$

For a detailed derivation of the hydrostatic balance, we refer to Pedlosky (1987, p. 59). Furthermore Cushman-Roisin and Beckers (2009) show that the reciprocal Coriolis term is negligible when compared to the other terms in the horizontal momentum conservation equation and can be omitted. The dominant balances result in the three-dimensional shallow water equations:

$$\begin{cases} \dfrac{\partial u}{\partial x} + \dfrac{\partial v}{\partial y} + \dfrac{\partial w}{\partial z} = 0, & \text{(2.1.6a)} \\ \dfrac{\partial u}{\partial t} + u\dfrac{\partial u}{\partial x} + v\dfrac{\partial u}{\partial y} + w\dfrac{\partial u}{\partial z} - fv = -\dfrac{1}{\rho}\dfrac{\partial p}{\partial x} + \dfrac{\partial}{\partial x}\left(\mathcal{A}_{\mathrm{h}}\dfrac{\partial u}{\partial x}\right) + \dfrac{\partial}{\partial y}\left(\mathcal{A}_{\mathrm{h}}\dfrac{\partial u}{\partial y}\right) + \dfrac{\partial}{\partial z}\left(\mathcal{A}_{\mathrm{v}}\dfrac{\partial u}{\partial z}\right), & \text{(2.1.6b)} \\ \dfrac{\partial v}{\partial t} + u\dfrac{\partial v}{\partial x} + v\dfrac{\partial v}{\partial y} + w\dfrac{\partial v}{\partial z} + fu = -\dfrac{1}{\rho}\dfrac{\partial p}{\partial y} + \dfrac{\partial}{\partial x}\left(\mathcal{A}_{\mathrm{h}}\dfrac{\partial v}{\partial x}\right) + \dfrac{\partial}{\partial y}\left(\mathcal{A}_{\mathrm{h}}\dfrac{\partial v}{\partial y}\right) + \dfrac{\partial}{\partial z}\left(\mathcal{A}_{\mathrm{v}}\dfrac{\partial v}{\partial z}\right), & \text{(2.1.6c)} \\ \dfrac{\partial p}{\partial z} = -\rho g. & \text{(2.1.6d)} \end{cases}$$

Thus the assumption that the water is shallow, as is the case in coastal areas, allows equation (2.1.5d) to be reduced to equation (2.1.6d).

2.2 Derivation of the depth-averaged equations

In this section, the depth-averaged equations are derived by integrating their three-dimensional counterparts over the water depth. First, the continuity equation is integrated over the water depth, followed by the depth integration of the momentum equations. Lastly, the two-dimensional shallow water equations are presented.

2.2.1 Geometry, forcing and boundary conditions

Geometry

In Figure 2.2 a cross-sectional view of the water column is shown. The free surface is given by $z = H + \zeta$ with ζ the deviation of the free surface from the reference height H. The erodible bed is located at $z = h$.

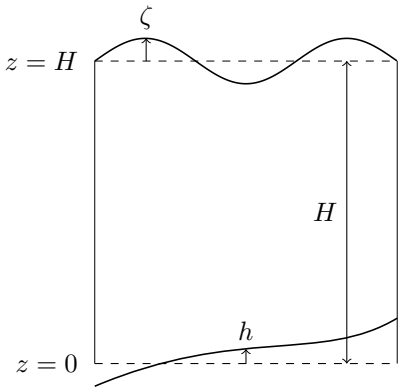

Figure 2.2: Cross-sectional view of a vertical water column.

Tidal forcing

The water motion inside the domain is driven by the tides. A tidal wave consists of many frequencies or constituents, but the most important and well-known frequency is the semidiurnal tidal constituent. The semidiurnal tide has a period of 12 hours and 25 minutes and is responsible for the majority of the ebb and flood behaviour observed on beaches. Henceforth, the semidiurnal tidal constituent is prescribed for the free surface at the boundary of the domain of interest:

$$\zeta = A \cos \sigma t \quad \text{on} \quad \partial\Omega, \tag{2.2.1}$$

where A is the amplitude of the semidiurnal tide, σ the angular frequency of the semidiurnal tide and $\partial\Omega$ is part of the domain boundary.

Kinematic boundary conditions

The water column has two boundaries, one at the top of the water column (at the interface between water and air) and one at the bottom of the water column (at the interface between water and the seabed). The boundary at the top of the water column is considered first.

The boundary between water and air is a free-surface boundary where a kinematic boundary condition is prescribed. A kinematic boundary condition states that fluid particles on the free surface always remain part of the free surface. Consider a water parcel at the interface between water and air with coordinates x_p, y_p and z_p. The kinematic boundary condition states that the height of the water parcel z_p is fully dependent on the free surface height at the water particle location $H + \zeta(x_\mathrm{p}, y_\mathrm{p}, t)$, hence $z_\mathrm{p} = H + \zeta(x_\mathrm{p}, y_\mathrm{p}, t)$. A more convenient way to express the kinematic boundary condition is found by

taking the material derivative (D/Dt) of $z_\mathrm{p} = H + \zeta(x_\mathrm{p}, y_\mathrm{p}, t)$, which can be taken since the equality is valid for all x, y and t. Furthermore, dropping the subscript p, as the equation holds for all fluid parcels at the surface, results in

$$w = \frac{\partial \zeta}{\partial t} + u\frac{\partial \zeta}{\partial x} + v\frac{\partial \zeta}{\partial y} \quad \text{at} \quad z = H + \zeta. \tag{2.2.2}$$

Similarly, a kinematic boundary condition is prescribed at the bottom since the seabed is assumed to be dynamic, albeit at very long time scales. Taking the material derivative of the kinematic boundary condition at the seabed yields the boundary condition

$$w = \frac{\partial h}{\partial t} + u\frac{\partial h}{\partial x} + v\frac{\partial h}{\partial y} \quad \text{at} \quad z = h. \tag{2.2.3}$$

Dynamic boundary conditions

Similar to the kinematic boundary conditions, dynamic boundary conditions have to be prescribed at the sea surface and seabed.

Bed shear stresses Let $\tau_{\mathrm{bed},x}$ denote the shear stress that acts on the plane tangential to the seabed, in the x direction. The shear stress of a Newtonian fluid at the seabed is given by

$$\tau_{\mathrm{bed},x} = \mu\frac{\partial u}{\partial n} \implies \frac{\tau_{\mathrm{bed},x}}{\rho} = \nu \nabla u \cdot \boldsymbol{n},$$

where μ is the dynamic viscosity, ν is the kinematic viscosity and the vector $\boldsymbol{n}$ is normal to the seabed. During the derivation of the Reynolds Averaged Navier-Stokes equations the kinematic viscosity ν was replaced by the effective horizontal and vertical eddy viscosity coefficients $\mathcal{A}_\mathrm{h}, \mathcal{A}_\mathrm{v}$ respectively. It follows that

$$\frac{\tau_{\mathrm{bed},x}}{\rho} = \begin{bmatrix} \mathcal{A}_\mathrm{h}\frac{\partial u}{\partial x} \\ \mathcal{A}_\mathrm{h}\frac{\partial u}{\partial y} \\ \mathcal{A}_\mathrm{v}\frac{\partial u}{\partial z} \end{bmatrix} \cdot \begin{bmatrix} -\frac{\partial h}{\partial x} \\ -\frac{\partial h}{\partial y} \\ 1 \end{bmatrix} = -\mathcal{A}_\mathrm{h}\frac{\partial u}{\partial x}\frac{\partial h}{\partial x} - \mathcal{A}_\mathrm{h}\frac{\partial u}{\partial y}\frac{\partial h}{\partial y} + \mathcal{A}_\mathrm{v}\frac{\partial u}{\partial z} \quad \text{at} \quad z = h, \tag{2.2.4}$$

where the normal at the seabed points into the fluid domain. A similar result can be derived for $\tau_{\mathrm{bed},y}$, the shear stress that acts on the plane tangential to the seabed, in the y direction.

Dimensional analysis shows that the bottom shear stress depends quadratically on the flow velocity. Thus the bottom shear stresses are parametrised using the quadratic bottom stress law:

$$\frac{\tau_{\mathrm{bed},x}}{\rho} = C_d\sqrt{u_\mathrm{b}^2 + v_\mathrm{b}^2}\, u_\mathrm{b} \qquad \text{and} \qquad \frac{\tau_{\mathrm{bed},y}}{\rho} = C_d\sqrt{u_\mathrm{b}^2 + v_\mathrm{b}^2}\, v_\mathrm{b}.$$

See for example Burchard *et al.* (2011). Here, C_d is a drag coefficient which is typically taken as 0.0025 and $u_\mathrm{b}, v_\mathrm{b}$ are the horizontal components of the flow velocity at the seabed.

Lorentz linearisation When considering water motion forced by a dominant frequency, the nonlinear bottom shear stresses give rise to solutions consisting of a fundamental frequency and higher harmonics. To simplify the equations the quadratic terms can be linearised which suppresses the higher harmonics. In 1922, Lorentz proposed a linearisation of the quadratic bottom shear stress such that the mean energy dissipation in both systems is the same. Terra *et al.* (2005) have experimentally verified Lorentz linearisation and found good agreement with the theory for the Helmholtz mode in an almost enclosed basin. The Helmholtz mode, or pumping mode, is a simple mode for basins that are short compared to the tidal wavelength, in which the sea level elevation is uniform inside of the embayment and co-oscillates with the sea at the inlet. Lorentz linearisation of the quadratic friction terms results in

$$\frac{\tau_{\mathrm{bed},x}}{\rho} = \hat{r}u_\mathrm{b} \qquad \text{and} \qquad \frac{\tau_{\mathrm{bed},y}}{\rho} = \hat{r}v_\mathrm{b}, \tag{2.2.5}$$

where the friction coefficient $\hat{r}$ has to be determined such that the amount of energy dissipated in the linearised model is the same as in the original quadratic model. For periodic flow, Vreugdenhil (1994, p. 57) has given an explicit expression for $\hat{r}$:

$$\hat{r} = \frac{8}{3\pi} C_{\mathrm{d}} U,$$

where U is the characteristic flow velocity, which can be determined from equation (2.2.17).

Wind shear stresses The stresses $\tau_{\mathrm{wind},x}$ and $\tau_{\mathrm{wind},y}$ denote the shear stresses that act on the plane tangential to the sea surface, in the x and y dimension respectively. The shear stress due to the wind at the sea surface in the x direction reads

$$\frac{\tau_{\mathrm{wind},x}}{\rho} = -\mathcal{A}_{\mathrm{h}} \frac{\partial u}{\partial x}\frac{\partial \zeta}{\partial x} - \mathcal{A}_{\mathrm{h}} \frac{\partial u}{\partial y}\frac{\partial \zeta}{\partial y} + \mathcal{A}_{\mathrm{v}} \frac{\partial u}{\partial z} \quad \text{at} \quad z = H + \zeta. \tag{2.2.6}$$

An analogue result can be derived for $\tau_{\mathrm{wind},y}$. Often the wind shear stress is parametrised with a quadratic dependence on the wind speed at 10 meters above sea level as

$$\frac{\tau_{\mathrm{wind},x}}{\rho} = \frac{\rho_{\mathrm{a}}}{\rho} C_{\mathrm{D}} \sqrt{U_{10}^2 + V_{10}^2}\, U_{10} \qquad \text{and} \qquad \frac{\tau_{\mathrm{wind},y}}{\rho} = \frac{\rho_{\mathrm{a}}}{\rho} C_{\mathrm{D}} \sqrt{U_{10}^2 + V_{10}^2}\, V_{10}.$$

Here, U_{10}, V_{10} are the horizontal components of the average wind velocity 10 meters above sea level and C_D is a drag coefficient, which generally depends on wind velocity.

Zero wind shear stress The wind flowing over the water surface generates wind-driven flows. In this thesis, we focus on tidal-driven flows and not on wind-driven flows. Hence, the wind shear stresses are assumed to vanish:

$$\tau_{\mathrm{wind},x} = \tau_{\mathrm{wind},y} = 0. \tag{2.2.7}$$

2.2.2 Depth-averaged conservation of mass

As explained in section 2.1.2, the continuity equation (2.1.6a) is used to represent the conservation of mass and is restated here:

$$\frac{\partial u}{\partial x} + \frac{\partial v}{\partial y} + \frac{\partial w}{\partial z} = 0.$$

Integrating the incompressible flow condition over the height of the water column $H + \zeta - h$ gives

$$\int_h^{H+\zeta} \frac{\partial u}{\partial x} + \frac{\partial v}{\partial y} + \frac{\partial w}{\partial z}\, dz = 0.$$

The three terms can be integrated separately since integration is a linear operator. Invoking the fundamental theorem of calculus yields

$$\int_h^{H+\zeta} \frac{\partial u}{\partial x}\, dz + \int_h^{H+\zeta} \frac{\partial v}{\partial y}\, dz + \big[w\big]_h^{H+\zeta} = 0. \tag{2.2.8}$$

Leibniz's integration rule has to be employed to exchange the order of integration and differentiation for variable domains of integration. For a general function $f(x, y, z, t)$ and limits of integration $a(x)$ and $b(x)$, Leibniz's integral rule states that

$$\frac{\partial}{\partial x}\left(\int_a^b f\, dz\right) = \int_a^b \frac{\partial f}{\partial x}\, dz + f\big|_b \frac{\partial b}{\partial x} - f\big|_a \frac{\partial a}{\partial x}.$$

Solving for the term that first differentiates and then integrates gives the desired form of Leibniz integral rule

$$\int_a^b \frac{\partial f}{\partial x}\, dz = \frac{\partial}{\partial x}\left(\int_a^b f\, dz\right) + f\big|_a \frac{\partial a}{\partial x} - f\big|_b \frac{\partial b}{\partial x}. \tag{2.2.9}$$

Using the rewritten Leibniz integral rule given by equation (2.2.9) for terms one and two in the integrated incompressible flow equation (2.2.8), noting that H is constant and combining the boundary terms results in

$$\frac{\partial}{\partial x}\left(\int_h^{H+\zeta} u\,dz\right) + \frac{\partial}{\partial y}\left(\int_h^{H+\zeta} v\,dz\right) + \left[u\frac{\partial h}{\partial x} + v\frac{\partial h}{\partial y} - w\right]_h - \left[u\frac{\partial \zeta}{\partial x} + v\frac{\partial \zeta}{\partial y} - w\right]_{H+\zeta} = 0.$$

The depth-averaged velocities are defined as

$$\bar{u} = \frac{1}{H+\zeta-h}\int_h^{H+\zeta} u\,dz \qquad \text{and} \qquad \bar{v} = \frac{1}{H+\zeta-h}\int_h^{H+\zeta} v\,dz. \tag{2.2.10}$$

Using the kinematic boundary conditions, given by equations (2.2.2) and (2.2.3), for the boundary terms, substituting the depth-averaged velocities and rearranging results in the two-dimensional depth-averaged mass conservation equation:

$$\frac{\partial \zeta}{\partial t} - \frac{\partial h}{\partial t} + \frac{\partial}{\partial x}\big[(H+\zeta-h)\bar{u}\big] + \frac{\partial}{\partial y}\big[(H+\zeta-h)\bar{v}\big] = 0. \tag{2.2.11}$$

2.2.3 Depth-averaged conservation of momentum

The horizontal momentum equations are depth-averaged by integrating over the depth of the corresponding conservative form of the equations. Only the averaging of the x momentum equation is considered as the averaging of momentum in the y dimension follows analogously.

Conservative form

The evolution of u as given by equation (2.1.6b) of the three-dimensional shallow water equations can be written in conservative form by adding the product of the continuity equation (2.1.6a) with u and using the product rule backwards. The conservative form of the conservation of momentum in the x dimension, equation (2.1.6b), is found to be

$$\frac{\partial u}{\partial t} + \frac{\partial}{\partial x}\big(u^2\big) + \frac{\partial}{\partial y}(uv) + \frac{\partial}{\partial z}(uw) - fv = -\frac{1}{\rho}\frac{\partial p}{\partial x} + \frac{\partial}{\partial x}\left(\mathcal{A}_{\mathrm{h}}\frac{\partial u}{\partial x}\right) + \frac{\partial}{\partial y}\left(\mathcal{A}_{\mathrm{h}}\frac{\partial u}{\partial y}\right) + \frac{\partial}{\partial z}\left(\mathcal{A}_{\mathrm{v}}\frac{\partial u}{\partial z}\right). \tag{2.2.12}$$

Integration of the LHS

Integrating the Left-Hand Side (LHS) of the momentum equation for u, equation (2.2.12), employing the rewritten form of Leibniz integral rule (2.2.9), using the fundamental theorem of calculus and rearranging gives

$$\begin{aligned}\int_h^{H+\zeta} \frac{\partial u}{\partial t} + \frac{\partial}{\partial x}\big(u^2\big) + \frac{\partial}{\partial y}(uv) + \frac{\partial}{\partial z}(uw) - fv\,dz \\ = \frac{\partial}{\partial t}\left(\int_h^{H+\zeta} u\,dz\right) + \frac{\partial}{\partial x}\left(\int_h^{H+\zeta} u^2\,dz\right) + \frac{\partial}{\partial y}\left(\int_h^{H+\zeta} uv\,dz\right) - f\int_h^{H+\zeta} v\,dz \\ + u\big|_h\left[\frac{\partial h}{\partial t} + u\frac{\partial h}{\partial x} + v\frac{\partial h}{\partial y} - w\right]_h - u\big|_{H+\zeta}\left[\frac{\partial \zeta}{\partial t} + u\frac{\partial \zeta}{\partial x} + v\frac{\partial \zeta}{\partial y} - w\right]_{H+\zeta}.\end{aligned}$$

The terms in the square brackets are zero due to the kinematic boundary conditions, see equations (2.2.2) and (2.2.3).

The velocities are decomposed into a depth-averaged mean part and a fluctuating part, similar to Reynolds decomposition that was used during the derivation of the Reynolds Averaged Navier–Stokes equations, but then with the averaging carried out over space instead of time. The depth-averaged mean part, denoted with an overbar, is the same as the depth-average and is already defined in equation (2.2.10). It should be noted that the depth-averaged mean part itself is independent of the depth and as such can

be taken outside of the depth integral. The fluctuating part is denoted with a tilde and is defined as the difference between the quantity itself and its mean part. For example for u the fluctuation is defined as $\tilde{u} = u - \bar{u}$. For these fluctuating parts, it holds that the depth integral vanishes, thus for u we have

$$\int_h^{H+\zeta} \tilde{u}\, dz = 0.$$

Using the decompositions $u = \bar{u} + \tilde{u}$ and $v = \bar{v} + \tilde{v}$, we obtain

$$\begin{aligned}\frac{\partial}{\partial t}\left(\int_h^{H+\zeta} u\, dz\right) + \frac{\partial}{\partial x}\left(\int_h^{H+\zeta} u^2\, dz\right) + \frac{\partial}{\partial y}\left(\int_h^{H+\zeta} uv\, dz\right) - f\int_h^{H+\zeta} v\, dz = \frac{\partial}{\partial t}\big[(H+\zeta-h)\bar{u}\big] \\ + \frac{\partial}{\partial x}\left[(H+\zeta-h)\bar{u}^2 + \int_h^{H+\zeta} \tilde{u}^2\, dz\right] + \frac{\partial}{\partial y}\left[(H+\zeta-h)\bar{u}\bar{v} + \int_h^{H+\zeta} \tilde{u}\tilde{v}\, dz\right] - (H+\zeta-h)f\bar{v}.\end{aligned}$$

Again a closure problem is encountered. Similar to the Reynolds stresses, the integral terms are parametrised as additional viscosity terms. However, instead of the symmetric parametrisation taken earlier the following asymmetric form is chosen:

$$\int_h^{H+\zeta} \tilde{u}^2\, dz = -\tilde{A}_{\mathrm{h}}(H+\zeta-h)\frac{\partial \bar{u}}{\partial x} \qquad \text{and} \qquad \int_h^{H+\zeta} \tilde{u}\tilde{v}\, dz = -\tilde{A}_{\mathrm{h}}(H+\zeta-h)\frac{\partial \bar{u}}{\partial y},$$

in line with Nihoul (1975, p. 47), simplifying the analysis considerably.

Application of the product rule, using the two-dimensional depth-averaged conservation of mass equation (2.2.11) to cancel some terms and substitution of the additional viscosity terms results in

$$\begin{aligned}&\frac{\partial}{\partial t}\big[(H+\zeta-h)\bar{u}\big] + \frac{\partial}{\partial x}\left[(H+\zeta-h)\bar{u}^2 + \int_h^{H+\zeta} \tilde{u}^2\, dz\right] + \frac{\partial}{\partial y}\left[(H+\zeta-h)\bar{u}\bar{v} + \int_h^{H+\zeta} \tilde{u}\tilde{v}\, dz\right] \\ &- (H+\zeta-h)f\bar{v} \qquad (2.2.13)\\ &\quad = (H+\zeta-h)\left(\frac{\partial \bar{u}}{\partial t} + \bar{u}\frac{\partial \bar{u}}{\partial x} + \bar{v}\frac{\partial \bar{u}}{\partial y} - f\bar{v}\right) - \frac{\partial}{\partial x}\left(\tilde{A}_{\mathrm{h}}(H+\zeta-h)\frac{\partial \bar{u}}{\partial x}\right) - \frac{\partial}{\partial y}\left(\tilde{A}_{\mathrm{h}}(H+\zeta-h)\frac{\partial \bar{u}}{\partial y}\right).\end{aligned}$$

Integration of the RHS

The hydrostatic balance can be used to find an explicit expression for the pressure under the assumption that the water density ρ is independent of the depth z. Integrating the hydrostatic balance (2.1.6d) and using that the pressure at the sea surface is atmospheric pressure p_{a} yields the hydrostatic pressure relationship

$$p = p_{\mathrm{a}} + \rho g(H+\zeta-z). \qquad (2.2.14)$$

The atmospheric pressure p_{a} is assumed to be constant at the sea surface.

Integrating the Right-Hand Side (RHS) of equation (2.2.12), substituting the hydrostatic pressure relationship (2.2.14), invoking Leibniz's integral rule, applying the fundamental theorem of calculus and rearranging yields

$$\begin{aligned}&\int_h^{H+\zeta} -\frac{1}{\rho}\frac{\partial p}{\partial x} + \frac{\partial}{\partial x}\left(\mathcal{A}_{\mathrm{h}}\frac{\partial u}{\partial x}\right) + \frac{\partial}{\partial y}\left(\mathcal{A}_{\mathrm{h}}\frac{\partial u}{\partial y}\right) + \frac{\partial}{\partial z}\left(\mathcal{A}_{\mathrm{v}}\frac{\partial u}{\partial z}\right) dz \\ &\qquad = -(H+\zeta-h)g\frac{\partial \zeta}{\partial x} + \frac{\partial}{\partial x}\left(\int_h^{H+\zeta} \mathcal{A}_{\mathrm{h}}\frac{\partial u}{\partial x}\, dz\right) + \frac{\partial}{\partial y}\left(\int_h^{H+\zeta} \mathcal{A}_{\mathrm{h}}\frac{\partial u}{\partial y}\, dz\right) \\ &\qquad\quad + \left[\mathcal{A}_{\mathrm{h}}\frac{\partial u}{\partial x}\frac{\partial h}{\partial x} + \mathcal{A}_{\mathrm{h}}\frac{\partial u}{\partial y}\frac{\partial h}{\partial y} - \mathcal{A}_{\mathrm{v}}\frac{\partial u}{\partial z}\right]_h - \left[\mathcal{A}_{\mathrm{h}}\frac{\partial u}{\partial x}\frac{\partial \zeta}{\partial x} + \mathcal{A}_{\mathrm{h}}\frac{\partial u}{\partial y}\frac{\partial \zeta}{\partial y} - \mathcal{A}_{\mathrm{v}}\frac{\partial u}{\partial z}\right]_{H+\zeta}.\end{aligned}$$

The Lorentz linearised bottom stresses (2.2.4) are parametrised in terms of the depth-averaged velocities to obtain a closed system of equations, hence

$$\frac{\tau_{\mathrm{bed},x}}{\rho} = r^*\bar{u} \qquad \text{and} \qquad \frac{\tau_{\mathrm{bed},y}}{\rho} = r^*\bar{v}, \qquad (2.2.15)$$

Table 2.1: Characteristic values of the Ameland inlet system. Courtesy of Ter Brake (2011).

Channel	Tide	Parameters
$L = 1.9 \cdot 10^4\,\mathrm{m}$	$\sigma = 1.4 \cdot 10^{-4}\,\mathrm{rad\,s^{-1}}$	$f = 10^{-4}\,\mathrm{rad\,s^{-1}}$
$H = 12\,\mathrm{m}$	$A = 0.84\,\mathrm{m}$	$g = 9.81\,\mathrm{m\,s^{-2}}$
	$U = 0.19\,\mathrm{m\,s^{-1}}$	$r^* = 4 \cdot 10^{-4}\,\mathrm{m\,s^{-1}}$
		$\hat{\mathcal{A}}_\mathrm{h} = 10\,\mathrm{m^2\,s^{-1}}$

where it is assumed that the difference between the friction velocity and the depth-averaged velocity can be captured with a new friction coefficient r^*. Assuming that the horizontal eddy viscosity is uniform over the depth and substituting the adjusted bottom stress (2.2.15) and wind stress (2.2.6) gives

$$\begin{aligned} &-(H+\zeta-h)g\frac{\partial\zeta}{\partial x} + \frac{\partial}{\partial x}\left(\mathcal{A}_\mathrm{h}(H+\zeta-h)\frac{\partial\bar{u}}{\partial x}\right) + \frac{\partial}{\partial y}\left(\mathcal{A}_\mathrm{h}(H+\zeta-h)\frac{\partial\bar{u}}{\partial y}\right) + \frac{\tau_{\mathrm{wind},x}}{\rho} - \frac{\tau_{\mathrm{bed},x}}{\rho} \\ &\quad = -(H+\zeta-h)g\frac{\partial\zeta}{\partial x} + \frac{\partial}{\partial x}\left(\mathcal{A}_\mathrm{h}(H+\zeta-h)\frac{\partial\bar{u}}{\partial x}\right) + \frac{\partial}{\partial y}\left(\mathcal{A}_\mathrm{h}(H+\zeta-h)\frac{\partial\bar{u}}{\partial y}\right) - r^*\bar{u}. \quad (2.2.16) \end{aligned}$$

At the last line, the explicit relations for the bottom stress (2.2.5) and wind stress (2.2.7) have been substituted, as discussed in section 2.2.1.

Combining LHS and RHS

Combing the results of the previous two paragraphs, i.e. equations (2.2.13) and (2.2.16), and dividing by the water depth yields the depth-averaged conservation of momentum equation for $\bar{u}$:

$$\frac{\partial\bar{u}}{\partial t} + \bar{u}\frac{\partial\bar{u}}{\partial x} + \bar{v}\frac{\partial\bar{u}}{\partial y} - f\bar{v} = -g\frac{\partial\zeta}{\partial x} + \frac{1}{H+\zeta-h}\left[-r^*\bar{u} + \frac{\partial}{\partial x}\left(\hat{\mathcal{A}}_\mathrm{h}(H+\zeta-h)\frac{\partial\bar{u}}{\partial x}\right) + \frac{\partial}{\partial y}\left(\hat{\mathcal{A}}_\mathrm{h}(H+\zeta-h)\frac{\partial\bar{u}}{\partial y}\right)\right],$$

where a new eddy viscosity coefficient has been defined as

$$\hat{\mathcal{A}}_\mathrm{h} = \mathcal{A}_\mathrm{h} + \tilde{A}_\mathrm{h}.$$

Scaling analysis

To simplify the momentum equation, the order of magnitude of each term is computed to investigate if there are any small terms which may be neglected. The order of magnitude of each term can be computed using its characteristic scales and values.

The water motion at the boundary of the domain is forced by the semidiurnal tidal constituent with amplitude A and angular frequency σ, see equation (2.2.1). It follows from the two-dimensional depth-averaged conservation of mass equation (2.2.11) and from the tidal forcing (2.2.1) that the dominant balance is

$$\sigma A \sim \frac{HU}{L}, \quad (2.2.17)$$

This balance implies that the characteristic scale for the flow velocity is given by $U \sim \sigma AL/H$. Furthermore, using the balance given by equation (2.2.17) and the dispersion relation for shallow water, $\lambda = \sqrt{gH}/\sigma$, it follows that

$$\frac{g}{\sigma U}\frac{\partial\zeta}{\partial x} \sim \frac{gA}{\sigma UL} \sim \left(\frac{\lambda}{L}\right)^2.$$

The scale of each term in the depth-averaged momentum equation is divided by σU to obtain dimensionless quantities that are easier to compare. Both the scaling and the order of magnitude are shown below the corresponding term of the momentum equation:

$$\frac{\partial \bar{u}}{\partial t}+\bar{u}\frac{\partial \bar{u}}{\partial x}+\bar{v}\frac{\partial \bar{u}}{\partial y}-f\bar{v}=-g\frac{\partial \zeta}{\partial x}-\frac{1}{H+\zeta-h}\left[r^*\bar{u}-\frac{\partial}{\partial x}\left(\hat{\mathcal{A}}_{\mathrm{h}}(H+\zeta-h)\frac{\partial \bar{u}}{\partial x}\right)-\frac{\partial}{\partial y}\left(\hat{\mathcal{A}}_{\mathrm{h}}(H+\zeta-h)\frac{\partial \bar{u}}{\partial y}\right)\right].$$

1	$\frac{U}{\sigma L}$	$\frac{U}{\sigma L}$	$\frac{f}{\sigma}$	$\frac{\lambda^2}{L^2}$	$\frac{r^*}{\sigma H}$	$\frac{\hat{\mathcal{A}}_{\mathrm{h}}}{\sigma L^2}$	$\frac{\hat{\mathcal{A}}_{\mathrm{h}}}{\sigma L^2}$
1	0.07	0.07	0.7	16	0.2	$2\cdot 10^{-4}$	$2\cdot 10^{-4}$

The order of magnitudes have been computed using the characteristic values shown in Table 2.1. The pressure term is rather large and this property is exploited in section 3.2.2. Furthermore, the eddy viscosity terms are significantly smaller than the other terms. Hence, the eddy viscosity terms can be neglected. It should be noted that the above analysis is not valid at the boundaries and it is possible that the eddy viscosity terms play an important role there. Since we are only interested in the behaviour of the flow in the main part of the domain this analysis is justified.

To ensure that the bottom friction is finite a small constant h_0 is introduced in the denominator of the bottom friction term. The two-dimensional depth-averaged conservation of momentum equations are then given by

$$\begin{cases} \dfrac{\partial \bar{u}}{\partial t}+\bar{u}\dfrac{\partial \bar{u}}{\partial x}+\bar{v}\dfrac{\partial \bar{u}}{\partial y}-f\bar{v}=-g\dfrac{\partial \zeta}{\partial x}-\dfrac{r^*\bar{u}}{H+\zeta-h+h_0}, & \text{(2.2.18a)}\\ \dfrac{\partial \bar{v}}{\partial t}+\bar{u}\dfrac{\partial \bar{v}}{\partial x}+\bar{v}\dfrac{\partial \bar{v}}{\partial y}+f\bar{u}=-g\dfrac{\partial \zeta}{\partial y}-\dfrac{r^*\bar{v}}{H+\zeta-h+h_0}. & \text{(2.2.18b)} \end{cases}$$

2.2.4 The two-dimensional shallow water equations

Combing the result of the depth-averaged conservation of mass with the result of the depth-averaged conservation of momentum, i.e. equations (2.2.11) and (2.2.18a-b), yields the two-dimensional shallow water equations:

$$\begin{cases} \dfrac{\partial \zeta}{\partial t}-\dfrac{\partial h}{\partial t}+\dfrac{\partial}{\partial x}\big[(H+\zeta-h)\bar{u}\big]+\dfrac{\partial}{\partial y}\big[(H+\zeta-h)\bar{v}\big]=0, & \text{(2.2.19a)}\\ \dfrac{\partial \bar{u}}{\partial t}+\bar{u}\dfrac{\partial \bar{u}}{\partial x}+\bar{v}\dfrac{\partial \bar{u}}{\partial y}-f\bar{v}=-g\dfrac{\partial \zeta}{\partial x}-\dfrac{r^*\bar{u}}{H+\zeta-h+h_0}, & \text{(2.2.19b)}\\ \dfrac{\partial \bar{v}}{\partial t}+\bar{u}\dfrac{\partial \bar{v}}{\partial x}+\bar{v}\dfrac{\partial \bar{v}}{\partial y}+f\bar{u}=-g\dfrac{\partial \zeta}{\partial y}-\dfrac{r^*\bar{v}}{H+\zeta-h+h_0}. & \text{(2.2.19c)} \end{cases}$$

Here, the overbar $\bar{\cdot}$ denotes the depth-averaged quantity. The first equation (2.2.19a) represents the conservation of mass and the last two equations (2.2.19b–c) represent the conservation of momentum in the x and y directions respectively.

2.3 Derivation of the cross-sectionally-averaged equations

In this section, the depth-averaged equations are integrated over the width of the domain to obtain the one-dimensional cross-sectionally-averaged equations.

2.3.1 Geometry and boundary conditions

Geometry

A sketch of the channel geometry is shown in Figure 2.3. The x-axis is directed along the channel and $B_1(x)$ and $B_2(x)$ are the lower and upper boundary of the channel respectively.

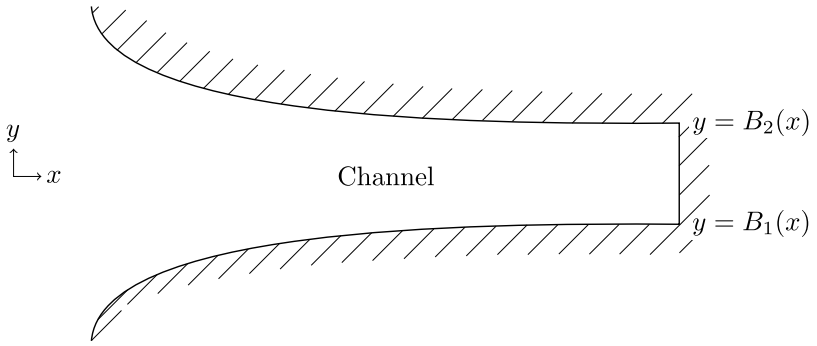

Figure 2.3: Top view of the channel geometry.

Impermeable wall boundary conditions

The boundary of the channel is stationary and impermeable, thus the fluid cannot flow through the edge of the channel. This is equivalent to requiring that there is no flow perpendicular, or normal, to the boundary. Hence at the first boundary of the embayment B_1, we have

$$\bar{\boldsymbol{u}} \cdot \boldsymbol{n} = 0 \implies \begin{bmatrix} \bar{u} \\ \bar{v} \end{bmatrix} \cdot \begin{bmatrix} \frac{dB_1}{dx} \\ -1 \end{bmatrix} = 0 \implies \bar{u}\frac{dB_1}{dx} - \bar{v} = 0 \quad \text{at} \quad y = B_1, \tag{2.3.1}$$

where the boundary normal is chosen to point away from the fluid.

Similarly, at the second boundary B_2 an impermeable boundary condition gives

$$-\bar{u}\frac{dB_2}{dx} + \bar{v} = 0 \quad \text{at} \quad y = B_2. \tag{2.3.2}$$

2.3.2 Width and depth-averaged conservation of mass equation

Starting with the two-dimensional depth-averaged conservation of mass equation (2.2.11) and integrating from $B_1(x)$ to $B_2(x)$, i.e. integrating over the width of the channel which can vary depending on the position inside the channel x, yields

$$\int_{B_1}^{B_2} \frac{\partial \zeta}{\partial t} - \frac{\partial h}{\partial t} + \frac{\partial}{\partial x}\big[(H + \zeta - h)\bar{u}\big] + \frac{\partial}{\partial y}\big[(H + \zeta - h)\bar{v}\big]\, dy = 0.$$

The four terms can be integrated separately since integration is a linear operator. Differentiation with respect to t and integration can be exchanged since the limits of integration do not depend on t. For the

term with the partial derivative w.r.t. x the rewritten form of Leibniz integral rule given by equation (2.2.9) is used and for the last term the fundamental theorem of calculus is applied. Then, we obtain

$$\frac{\partial}{\partial t}\left(\int_{B_1}^{B_2}\zeta\,dy\right)-\frac{\partial}{\partial t}\left(\int_{B_1}^{B_2}h\,dy\right)+\frac{\partial}{\partial x}\left(\int_{B_1}^{B_2}(H+\zeta-h)\bar{u}\,dy\right)$$
$$+\left[(H+\zeta-h)\left(\bar{u}\frac{dB_1}{dx}-\bar{v}\right)\right]_{B_1}-\left[(H+\zeta-h)\left(\bar{u}\frac{dB_2}{dx}-\bar{v}\right)\right]_{B_2}=0.$$

The width-averaged quantities are defined as

$$\hat{\zeta}=\frac{1}{B_2-B_1}\int_{B_1}^{B_2}\zeta\,dy,\qquad \hat{h}=\frac{1}{B_2-B_1}\int_{B_1}^{B_2}h\,dy,\qquad \hat{\bar{u}}=\frac{1}{B_2-B_1}\int_{B_1}^{B_2}\bar{u}\,dy. \tag{2.3.3}$$

Using the with-averaged $\hat{\zeta}$ and $\hat{h}$ and substituting the two impermeable boundary conditions given by equations (2.3.1) and (2.3.2) yields that

$$\frac{\partial}{\partial t}\big[(B_2-B_1)\hat{\zeta}\big]-\frac{\partial}{\partial t}\big[(B_2-B_1)\hat{h}\big]+\frac{\partial}{\partial x}\left(\int_{B_1}^{B_2}(H+\zeta-h)\bar{u}\,dy\right)=0.$$

In order to further simplify the equation, especially the nonlinear term, all the width dependent variables are split into a width-independent mean part and a width-fluctuating part denoted with the superscript $\hat{\zeta}$ and $\tilde{\zeta}$ respectively for ζ. The mean width part is already defined by equation (2.3.3). The fluctuating part is defined by $\tilde{\zeta}=\zeta-\hat{\zeta}$. For the fluctuating part it follows that

$$\int_{B_1}^{B_2}\tilde{\zeta}\,dy=0.$$

Using $\zeta=\hat{\zeta}+\tilde{\zeta}$, $h=\hat{h}+\tilde{h}$ and $\bar{u}=\hat{\bar{u}}+\tilde{\bar{u}}$ then for the last term it follows that

$$\int_{B_1}^{B_2}(H+\zeta-h)\bar{u}\,dy=(B_2-B_1)(H+\hat{\zeta}-\hat{h})\hat{\bar{u}}+\int_{B_1}^{B_2}(\tilde{\zeta}-\tilde{h})\tilde{\bar{u}}\,dy,$$

since the mean of the fluctuating terms vanishes.

If the flow along the x axis is fairly uniform and if the channel is approximately rectangular, then the width variations are small and the product of two fluctuations is even smaller. However, these assumptions are not always justified and these assumptions represent the inherent difference between the two-dimensional and the one-dimensional description of the flow.

By omitting the covariance term, the cross-sectionally-averaged conservation of mass equation is obtained:

$$\frac{\partial}{\partial t}\big[(B_2-B_1)\hat{\zeta}\big]-\frac{\partial}{\partial t}\big[(B_2-B_1)\hat{h}\big]+\frac{\partial}{\partial x}\big[(B_2-B_1)(H+\hat{\zeta}-\hat{h})\hat{\bar{u}}\big]=0. \tag{2.3.4}$$

If the channel has a constant width such that the difference B_2-B_1 is independent of x, then the equation can be further simplified to

$$\frac{\partial\hat{\zeta}}{\partial t}-\frac{\partial\hat{h}}{\partial t}+\frac{\partial}{\partial x}\big[(H+\hat{\zeta}-\hat{h})\hat{\bar{u}}\big]=0. \tag{2.3.5}$$

2.3.3 Width and depth-averaged conservation of momentum equation

The conservative form of the depth-averaged conservation of momentum equation is found by combining the LHS of equation (2.2.13) with the RHS of equation (2.2.16) and using that the viscous terms are small. Moreover, Pedlosky (1987, p. 78) has shown that the rotational effects can be neglected for a narrow channel. A channel is considered narrow, if the channel width B is much smaller than the length of the channel L and if the channel width is much smaller than the Rossby deformation radius $R=\sqrt{gH}/f$ (Cushman-Roisin and Beckers, 2009, p. 252), i.e. $B\ll L,R$.

The two-dimensional depth-averaged conservation of momentum equation for $\bar{u}$ in conservative form is given by

$$\frac{\partial}{\partial t}\big[(H+\zeta-h)\bar{u}\big]+\frac{\partial}{\partial x}\big[(H+\zeta-h)\bar{u}^2\big]+\frac{\partial}{\partial y}\big[(H+\zeta-h)\bar{v}\bar{u}\big]=-(H+\zeta-h)g\frac{\partial\zeta}{\partial x}+r^*\bar{u}. \tag{2.3.6}$$

Integration of the LHS over the width of the channel and invoking Leibniz integral rule and the fundamental theorem of calculus yields

$$\int_{B_1}^{B_2}\left\{\frac{\partial}{\partial t}\big[(H+\zeta-h)\bar{u}\big]+\frac{\partial}{\partial x}\big[(H+\zeta-h)\bar{u}^2\big]+\frac{\partial}{\partial y}\big[(H+\zeta-h)\bar{v}\bar{u}\big]\right\}dy=\frac{\partial}{\partial t}\left(\int_{B_1}^{B_2}(H+\zeta-h)\bar{u}\,dy\right)$$
$$+\frac{\partial}{\partial x}\left(\int_{B_1}^{B_2}(H+\zeta-h)\bar{u}^2\,dy\right)+\left[(H+\zeta-h)\bar{u}\left(\bar{u}\frac{dB_1}{dx}-\bar{v}\right)\right]_{B_1}-\left[(H+\zeta-h)\bar{u}\left(\bar{u}\frac{dB_2}{dx}-\bar{v}\right)\right]_{B_2}.$$

The terms in the square brackets are zero due to the requirement that there is no flow perpendicular to the boundary, see the impermeable boundary conditions given by equation (2.3.1) and equation (2.3.2).

For the resulting terms the width decompositions $\zeta=\hat{\zeta}+\tilde{\zeta},\ h=\hat{h}+\tilde{h},\ \bar{u}=\hat{\bar{u}}+\tilde{\bar{u}}$ and $\bar{v}=\hat{\bar{v}}+\tilde{\bar{v}}$ are introduced

$$\frac{\partial}{\partial t}\left(\int_{B_1}^{B_2}(H+\zeta-h)\bar{u}\,dy\right)+\frac{\partial}{\partial x}\left(\int_{B_1}^{B_2}(H+\zeta-h)\bar{u}^2\,dy\right)=\frac{\partial}{\partial t}\left[(B_2-B_1)(H+\hat{\zeta}-\hat{h})\hat{\bar{u}}+\int_{B_1}^{B_2}(\tilde{\zeta}-\tilde{h})\tilde{\bar{u}}\,dy\right]$$
$$+\frac{\partial}{\partial x}\left[(B_2-B_1)(H+\hat{\zeta}-\hat{h})\hat{\bar{u}}^2+(H+\hat{\zeta}-\hat{h})\int_{B_1}^{B_2}\tilde{\bar{u}}^2\,dy+2\hat{\bar{u}}\int_{B_1}^{B_2}(\tilde{\zeta}-\tilde{h})\tilde{\bar{u}}\,dy+\int_{B_1}^{B_2}(\tilde{\zeta}-\tilde{h})\tilde{\bar{u}}^2\,dy\right].$$

If the flow along the x direction is reasonably uniform and if the channel is almost rectangular, then the width fluctuations are small and the product of two width fluctuations is even smaller. Hence, the covariance terms can be omitted. However, the assumptions about the uniformity of the flow and the channel geometry cannot be shown from first principles and represent the inherent difference between the two-dimensional and the one-dimensional description of the flow. Nevertheless, the covariance terms are neglected. Application of the product rule gives

$$\frac{\partial}{\partial t}\big[(B_2-B_1)(H+\hat{\zeta}-\hat{h})\hat{\bar{u}}\big]+\frac{\partial}{\partial x}\big[(B_2-B_1)(H+\hat{\zeta}-\hat{h})\hat{\bar{u}}\hat{\bar{u}}\big]=(B_2-B_1)(H+\hat{\zeta}-\hat{h})\left(\frac{\partial\hat{\bar{u}}}{\partial t}+\hat{\bar{u}}\frac{\partial\hat{\bar{u}}}{\partial x}\right)$$
$$+\hat{\bar{u}}\left(\frac{\partial}{\partial t}\big[(B_2-B_1)\hat{\zeta}\big]-\frac{\partial}{\partial t}\big[(B_2-B_1)\hat{h}\big]+\frac{\partial}{\partial x}\big[(B_2-B_1)(H+\hat{\zeta}-\hat{h})\hat{\bar{u}}\big]\right). \tag{2.3.7}$$

The last term is zero due to the conservation of mass equation (2.3.4).

Integrating the RHS of equation (2.3.6) over the channel width and using the width decomposition gives

$$\int_{B_1}^{B_2}-(H+\zeta-h)g\frac{\partial\zeta}{\partial x}+r^*\bar{u}\,dy \tag{2.3.8}$$
$$=-(B_2-B_1)(H+\hat{\zeta}-\hat{h})g\frac{\partial\hat{\zeta}}{\partial x}-(H+\hat{\zeta}-\hat{h})g\int_{B_1}^{B_2}\frac{\partial\tilde{\zeta}}{\partial x}\,dy-g\int_{B_1}^{B_2}(\tilde{\zeta}-\tilde{h})\frac{\partial\tilde{\zeta}}{\partial x}\,dy+(B_2-B_1)r^*\hat{\bar{u}}.$$

Similar to our earlier remarks, for one-dimensional fairly uniform flow the fluctuations are small and the covariance terms are neglected.

Combining the previous two results, i.e. equations (2.3.7) and (2.3.8), dividing by the sea depth and introducing the constant h_0 to ensure finite bottom friction yields the one-dimensional cross-sectionally-averaged conservation of momentum equation for variable channel width:

$$\frac{\partial\hat{\bar{u}}}{\partial t}+\hat{\bar{u}}\frac{\partial\hat{\bar{u}}}{\partial x}=-g\frac{\partial\hat{\zeta}}{\partial x}-\frac{r^*\hat{\bar{u}}}{H+\hat{\zeta}-\hat{h}+h_0}. \tag{2.3.9}$$

2.3.4 The one-dimensional shallow water equations

Combing the result of the cross-sectionally-averaged conservation of mass (2.3.5) with the result of the cross-sectionally-averaged conservation of momentum (2.3.9) yields the one-dimensional shallow water equations:

$$\begin{cases} \dfrac{\partial \hat{\zeta}}{\partial t} - \dfrac{\partial \hat{h}}{\partial t} + \dfrac{\partial}{\partial x}\left[(H + \hat{\zeta} - \hat{h})\hat{\bar{u}}\right] = 0, & \text{(2.3.10a)} \\ \dfrac{\partial \hat{\bar{u}}}{\partial t} + \hat{\bar{u}}\dfrac{\partial \hat{\bar{u}}}{\partial x} = -g\dfrac{\partial \hat{\zeta}}{\partial x} - \dfrac{r^* \hat{\bar{u}}}{H + \hat{\zeta} - \hat{h} + h_0}. & \text{(2.3.10b)} \end{cases}$$

Here, the overbar $\bar{\cdot}$ denotes the depth-averaged quantity and the hat $\hat{\cdot}$ denotes the width-averaged quantity. The first equation (2.3.10a) represents the conservation of mass and the second equation (2.3.10b) the conservation of momentum.

Chapter 3

The morphodynamics of an idealised tidal embayment

In this chapter, the idealised tidal embayment is introduced. The hydro-morphodynamic equations are presented in detail and simplified for the chosen characteristic values. The basin equilibrium bed profile is derived under the assumption of diffusively dominated transport and its asymptotic stability is proven. Then the temporal evolution of the basin bed is investigated and the numerical and analytical eigenvalues are compared. This chapter follows along the lines of Schuttelaars and De Swart (1996).

3.1 The one-dimensional idealised tidal embayment

In this section, the geometry of the one-dimensional idealised basin is introduced. Thereafter the equations that govern the transport of sediment are discussed and the corresponding boundary and initial conditions are given.

3.1.1 Geometry

The interaction between the motion of water, the transport of sediment and the seabed is studied in a semi-enclosed basin. In shallow embayments the main driver of horizontal sediment transport is the tide, hence these basins are called tidal embayments. A short, narrow, rectangular basin is considered with width B and length L, as shown in Figure 3.1a. The basin is short compared to the tidal wavelength and narrow compared to the Rossby deformation radius. The free surface is found at $z = \zeta + H$ with H a reference depth and the erodible bottom is given by $z = h$, see Figure 3.1b.

A brief description is presented of the processes governing the morphodynamics of the seabed. In the next sections, these processes and equations are described in more detail. The water inside of the basin is governed by the shallow water equations. This results in an equation for the free surface ζ and for the flow velocity u. The water flow whirls up sediment from the seabed which increases the suspended sediment concentration C. The suspended sediment is transported by advective and diffusive processes. Finally, the suspended sediment is deposited on the seabed h by gravitational forces. The seabed h changes due to the exchange of sediment with the water column. These processes and variables are illustrated in Figure 3.1b as well.

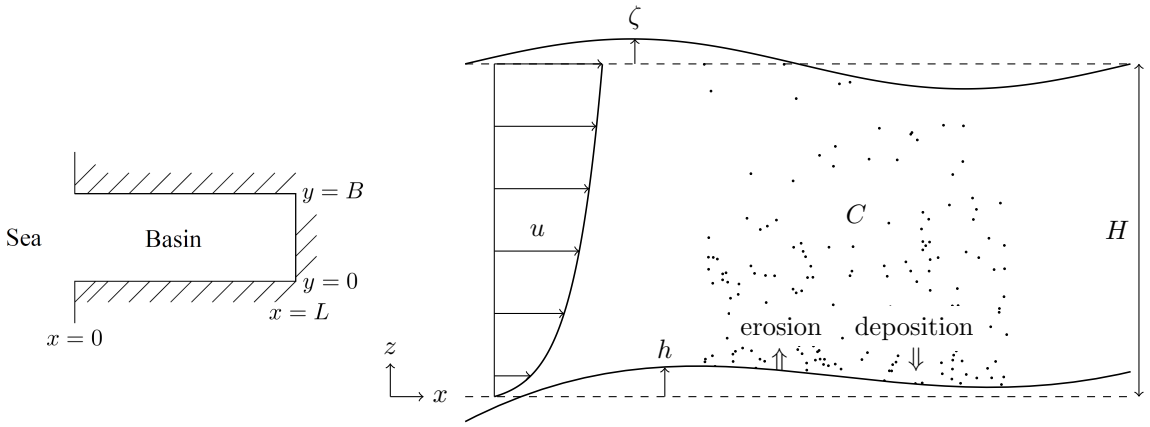

(a) Top view of the rectangular embayment.

(b) Cross-sectional view of a vertical water column.

Figure 3.1: Geometry of the one-dimensional idealised model. The log velocity profile shown is derived in Appendix A.1.

3.1.2 Hydrodynamics

The cross-sectionally-averaged shallow water equations are used to describe the motion of water. The cross-sectionally-averaged shallow water equations for narrow channels of constant width are

$$\begin{cases} \dfrac{\partial \zeta}{\partial t} - \dfrac{\partial h}{\partial t} + \dfrac{\partial}{\partial x}\big[(H+\zeta-h)u\big] = 0, & \text{(3.1.1a)} \\ \dfrac{\partial u}{\partial t} + u\dfrac{\partial u}{\partial x} = -g\dfrac{\partial \zeta}{\partial x} - \dfrac{r^* u}{H+\zeta-h+h_0}, & \text{(3.1.1b)} \end{cases}$$

see equations (2.3.10a–b) in Chapter 2 respectively. Here, ζ is the width-averaged free surface elevation, h is the width-averaged bottom profile and u is the cross-sectionally-averaged water velocity. Furthermore, H is a reference depth, g the gravitational acceleration, r^* a friction coefficient and h_0 is a small constant. The first equation represents the conservation of mass and the second equation the conservation of momentum.

3.1.3 Suspended sediment transport

The amount of sediment in the water column changes due to advective and diffusive transport processes as well as due to the exchange of sediment particles with the seabed. The equation that governs the transport of suspended sediment reads

$$\frac{\partial C}{\partial t} + \frac{\partial uC}{\partial x} - \kappa_{\mathrm{h}}\frac{\partial^2 C}{\partial x^2} - \frac{\partial}{\partial x}\left[\kappa_{\mathrm{h}}\frac{\omega_{\mathrm{s}}}{\kappa_{\mathrm{v}}}\beta\frac{\partial h}{\partial x}C\right] = \alpha u^2 - \frac{\omega_{\mathrm{s}}^2}{\kappa_{\mathrm{v}}}\beta C. \tag{3.1.2}$$

We refer to Ter Brake (2011) for a detailed derivation of the suspended sediment transport equation. Here, C is the depth-integrated and width-averaged concentration of suspended sediment, i.e. C is the amount of sediment stored in a water column of unit horizontal area. Moreover, κ_{h} is a constant horizontal diffusion coefficient, κ_{v} is a constant vertical diffusion coefficient, ω_{s} is a constant settling velocity, α is a constant erosion parameter and β is the deposition parameter which depends on the depth as

$$\beta = \frac{1}{1 - e^{-\omega_{\mathrm{s}}/\kappa_{\mathrm{v}}(\zeta+H-h+h_0)}}. \tag{3.1.3}$$

The physical interpretation of each term in the suspended sediment transport equation is given below:

- $\frac{\partial C}{\partial t}$: This term represents the rate of change of the depth-integrated and width-averaged suspended sediment concentration.

- $\frac{\partial uC}{\partial x}$: This term is the divergence of the advective sediment transport. It represents the sediment transport caused by the differences in the sediment advection rate. Sediment advection is the transport of suspended sediment due to the flow of water.
- $\kappa_\mathrm{h}\frac{\partial^2 C}{\partial x^2}$: This term is the divergence of the diffusive sediment transport. It represents the sediment transport caused by the differences in the sediment diffusion rate. Sediment diffusion is the natural tendency of suspended sediment to move from a region of high concentration to a region of low concentration.
- $\frac{\partial}{\partial x}\left[\kappa_\mathrm{h}\frac{\omega_\mathrm{s}}{\kappa_\mathrm{v}}\beta\frac{\partial h}{\partial x}C\right]$: This term is the divergence of the topologically induced diffusive sediment transport. It represents the sediment transport caused by the differences in the topologically induced sediment diffusion rate. This term originates from the fact that the depth-integrated concentration is considered instead of the three-dimensional sediment concentration. This term can be explained as follows. If two adjacent water columns contain the same amount of sediment but are different in depth, then an equal amount of sediment is distributed over a larger volume in the deeper water column, resulting in a lower sediment concentration than in the shallower water column. Hence, there is a concentration gradient towards the deeper water column. This concentration gradient gives rise to a net sediment flux towards deeper areas.
- αu^2: This term represents the addition of sediment to the water column due to the whirling up of sediment from the seabed.
- $\frac{\omega_\mathrm{s}^2}{\kappa_\mathrm{v}}\beta C$: This term represents the deposition of sediment from the water column to the seabed.

3.1.4 Bottom evolution

The seabed changes due to bedload fluxes, which represents the sliding, rolling and hopping of sediment along the bed, and due to the exchange of sediment particles with the water column. The equation that governs the evolution of the seabed reads

$$\rho_\mathrm{s}(1-p)\left(\frac{\partial h}{\partial t}+\frac{\partial S_\mathrm{b}}{\partial x}\right)=-\alpha u^2+\frac{\omega_\mathrm{s}^2}{\kappa_\mathrm{v}}\beta C. \tag{3.1.4}$$

The bottom evolution equation can be derived from the conservation of mass in the sediment layer, see e.g. Appendix A.2. Here, ρ_s is the density of the sediment particles, p is the porosity of the sediment layer and S_b is the volumetric bedload flux which represents the sliding, rolling and hopping of sediment along the bed in the active layer.

The sediment particles are either in suspension or deposited along the bed, hence the right-hand side of the bottom evolution equation (3.1.4) is exactly opposite to the right-hand side of the suspended sediment concentration equation (3.1.2).

A parametrisation of the volumetric bedload flux is given by

$$S_\mathrm{b}=\hat{s}\frac{|u|^b}{u_\mathrm{c}^b}\left(\frac{u}{|u|}-\mu_*\frac{\partial h}{\partial x}\right),$$

see for example Van Rijn (1993). Here, $b>1$ is a constant, μ_* is a bed slope correction coefficient (to model the preferred downhill transport), u_c is the critical erosion velocity and $\hat{s}$ is a parameter that is a function of the sediment properties.

3.1.5 Boundary and initial conditions

A semidiurnal tide is prescribed at the entrance of the embayment for the free surface, as the main driver of horizontal sediment transport is the tide. Thus

$$\zeta=A\cos\sigma t \quad \text{at} \quad x=0. \tag{3.1.5}$$

Here, A is the amplitude of the semidiurnal tide and σ is the angular frequency of the semidiurnal tide.

Water cannot be transported through the landward boundary at the end of the embayment, $x = L$. This leads to the requirement that

$$(H + \zeta - h)u = 0 \quad \text{at} \quad x = L.$$

The suspended sediment concentration is split into two parts: a tidally averaged part $\langle C \rangle$ and time fluctuating part C' as follows $C = \langle C \rangle + C'$ with $\langle C' \rangle = 0$. The solid boundary at $x = L$ prohibits the tidal averaged or net flow of sediment, i.e.

$$\langle uC \rangle - \kappa_{\mathrm{h}} \frac{\partial \langle C \rangle}{\partial x} - \kappa_{\mathrm{h}} \frac{\omega_{\mathrm{s}}}{\kappa_{\mathrm{v}}} \beta \frac{\partial h}{\partial x} \langle C \rangle = 0 \quad \text{at} \quad x = L.$$

Since the sediment transport equation is singularly perturbed for $0 < \kappa_{\mathrm{h}} \ll 1$, it is expected that a boundary layer, a region where the solution changes rapidly, forms. To make sure that no unphysical boundary layers form for the fluctuating part, the boundary condition should be chosen such that it is in line with the $\kappa_{\mathrm{h}} = 0$ case. Henceforth

$$C'(x, t, \kappa_{\mathrm{h}}) = C'(x, t, \kappa_{\mathrm{h}} = 0) \quad \text{at} \quad x = 0 \ \text{ and } \ x = 1.$$

The seabed at the entrance of the embayment should not change in time. Hence, the boundary condition at the entrance is

$$\frac{\partial h}{\partial t} = 0 \quad \text{at} \quad x = 0.$$

During ebb tide, the water level falls and the water line retracts. During flood tide, the water level rises and the water line advances. The landward boundary is located in the middle of these two extremes and we require that the tidally averaged transport vanishes at the landward boundary. Therefore

$$\langle F \rangle = 0 \quad \text{at} \quad x = L,$$

where the tidal averaged flux $\langle F \rangle$ is given by equation (3.2.13).

Normally, initial conditions are necessary in order to solve time-dependent partial differential equations. However, because the water motion is forced by the (periodic) tide at the entrance of the embayment (3.1.5) and because we are not interested in the transient behaviour, we search for periodic solutions on the short tidal time scale for ζ, u, C for a known bottom profile h. Hence, only an initial condition for the seabed is necessary (Schuttelaars, 1997, p. 24).

3.2 Simplifying the hydro-morphodynamic equations

In this section, the hydro-morphodynamic equations are nondimensionalized and simplified using the characteristic values of the Ameland inlet system.

3.2.1 Nondimensionalization

The hydro-morphodynamic equations are nondimensionalized by introducing the characteristic scale and the nondimensional quantity, denoted with an asterisk, of each variable as follows

$$\begin{aligned} x &= Lx^*, & h &= Hh^*, & u &= Uu^*, \\ t &= \frac{1}{\sigma} t^*, & \zeta &= \frac{HU}{\sigma L} \zeta^*, & C &= \frac{\alpha \kappa_{\mathrm{v}} U^2}{\omega_{\mathrm{s}}^2} C^*. \end{aligned} \tag{3.2.1}$$

Here, L is a horizontal length scale, H a vertical length scale, U a horizontal flow velocity scale and σ a frequency scale. The scaling of the amplitude of the tide follows from the balance between the first and last term in the conservation of mass equation. The concentration scale follows from the approximate balance between the deposition and the whirling up of sediment in the suspended sediment transport equation.

Conservation of mass

Substitution of the characteristic scales in the conservation of mass equation (3.1.1a) yields

$$\frac{HU}{L}\frac{\partial \zeta^*}{\partial t^*} - \sigma H \frac{\partial h^*}{\partial t^*} + \frac{HU}{L}\frac{\partial}{\partial x^*}\left[\left(1 + \frac{U}{\sigma L}\zeta^* - h^*\right)u^*\right] = 0.$$

Dividing by HU/L and defining $\varepsilon = U/(\sigma L)$ results in the nondimensional conservation of mass equation

$$\frac{\partial \zeta^*}{\partial t^*} - \frac{1}{\varepsilon}\frac{\partial h^*}{\partial t^*} + \frac{\partial}{\partial x^*}\left[(1 + \varepsilon\zeta^* - h^*)u^*\right] = 0. \tag{3.2.2}$$

Conservation of momentum

Introducing the characteristic scales in the conservation of momentum equation (3.1.1b) gives

$$\sigma U \frac{\partial u^*}{\partial t^*} + \frac{U^2}{L}u^*\frac{\partial u^*}{\partial x^*} = -\frac{gHU}{\sigma L^2}\frac{\partial \zeta^*}{\partial x^*} - \frac{r^*U}{H}\frac{u^*}{1 + \frac{U}{\sigma L}\zeta^* - h^* + h_0^*}.$$

This equation is divided by σU, then introducing $\varepsilon = U/(\sigma L)$, $\Lambda = gH/(\sigma^2 L^2)$ and the non-dimensional friction coefficient $r = r^*/(\sigma H)$, the conservation of momentum equation in nondimensional form is obtained

$$\frac{\partial u^*}{\partial t^*} + \varepsilon u^*\frac{\partial u^*}{\partial x^*} = -\Lambda\frac{\partial \zeta^*}{\partial x^*} - r\frac{u^*}{1 + \varepsilon\zeta^* - h^* + h_0^*}. \tag{3.2.3}$$

Suspended sediment transport

Substituting the characteristic scales in the suspended sediment transport equation (3.1.2) gives

$$\frac{\sigma\alpha\kappa_\mathrm{v}U^2}{\omega_\mathrm{s}^2}\frac{\partial C^*}{\partial t^*} + \frac{\alpha\kappa_\mathrm{v}U^3}{\omega_\mathrm{s}^2 L}\frac{\partial u^*C^*}{\partial x^*} - \frac{\alpha\kappa_\mathrm{h}\kappa_\mathrm{v}U^2}{\omega_\mathrm{s}^2 L^2}\frac{\partial^2 C^*}{\partial (x^*)^2} - \frac{\alpha\kappa_\mathrm{h}HU^2}{\omega_\mathrm{s}L^2}\frac{\partial}{\partial x^*}\left[\beta\frac{\partial h^*}{\partial x^*}C^*\right] = \alpha U^2(u^*)^2 - \alpha U^2\beta C^*.$$

Dividing by αU^2 and defining $a = \sigma\kappa_\mathrm{v}/\omega_\mathrm{s}^2$, $\varepsilon = U/(\sigma L)$, $\kappa = \kappa_\mathrm{h}/(\sigma L^2)$ and $\gamma = \omega_\mathrm{s}H/\kappa_\mathrm{v}$, the dimensionless suspended concentration equation is found

$$a\left\{\frac{\partial C^*}{\partial t^*} + \varepsilon\frac{\partial u^*C^*}{\partial x^*} - \kappa\left(\frac{\partial^2 C^*}{\partial (x^*)^2} + \gamma\frac{\partial}{\partial x^*}\left[\beta\frac{\partial h^*}{\partial x^*}C^*\right]\right)\right\} = (u^*)^2 - \beta C^*. \tag{3.2.4}$$

Bottom evolution

The nondimensional variables are introduced in the bottom evolution equation (3.1.4) as

$$\rho_\mathrm{s}(1-p)\left\{\sigma H\frac{\partial h^*}{\partial t^*} + \frac{\hat{s}U^b}{Lu_\mathrm{c}^b}\frac{\partial}{\partial x^*}\left[|u^*|^b\left(\frac{u^*}{|u^*|} - \frac{\mu_* H}{L}\frac{\partial h^*}{\partial x^*}\right)\right]\right\} = -\alpha U^2(u^*)^2 + \alpha U^2\beta C^*.$$

Dividing by $\rho_\mathrm{s}(1-p)\sigma H$ and defining $\delta_\mathrm{s} = \alpha U^2/\big(\rho_\mathrm{s}(1-p)\sigma H\big)$, $\delta_\mathrm{b} = \hat{s}U^b/\big(\sigma H L u_\mathrm{c}^b\big)$ and $\mu = \mu_* H/L$ gives

$$\frac{\partial h^*}{\partial t^*} + \delta_\mathrm{b}\frac{\partial}{\partial x^*}\left[|u^*|^b\left(\frac{u^*}{|u^*|} - \mu\frac{\partial h^*}{\partial x^*}\right)\right] = -\delta_\mathrm{s}\big((u^*)^2 - \beta C^*\big). \tag{3.2.5}$$

3.2.2 Scaling analysis and averaging

In order to apply scaling analysis, the characteristic values corresponding to the characteristic scales need to be chosen. Here, the Ameland inlet system is considered as it is one of the most natural tidal inlet systems along the Dutch coast (Van der Vegt, 2006, p. 8). No major human interferences affected this inlet system, thus it can be considered in morphodynamic equilibrium (Ter Brake, 2011, p. 6). Figure 3.2

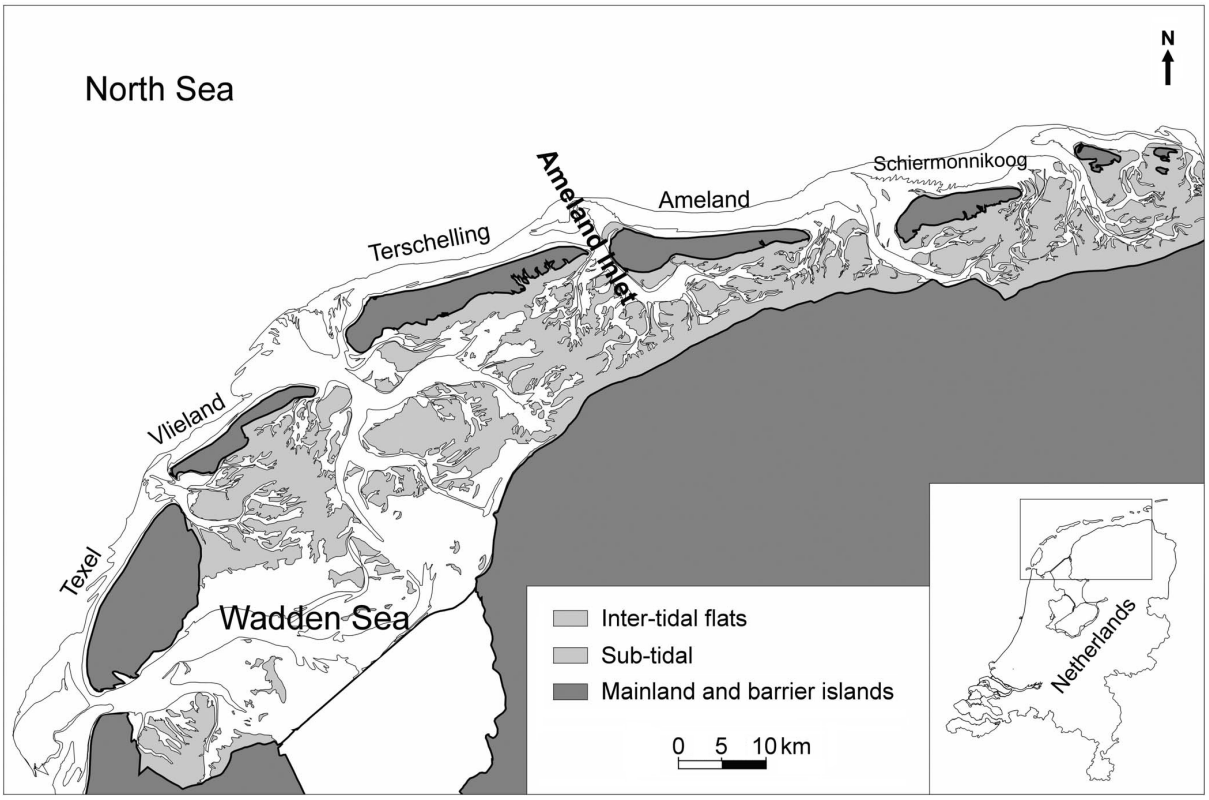

Figure 3.2: Bathymetry of the Dutch Wadden Sea. The Ameland inlet system is located between Terschelling and Ameland as indicated by the bold text. Adaptation based on Cheung *et al.* (2007).

shows a schematic representation of the bathymetry of the Dutch Wadden Sea and it shows the location of the Ameland inlet system.

The characteristic scales of the Ameland inlet system together with the resulting nondimensional parameters are shown in Table 3.1. The nondimensional parameters, which were defined during the nondimensionalization, are summarised below:

$$\begin{aligned} &\varepsilon = \frac{U}{\sigma L}, \qquad \Lambda = \frac{gH}{\sigma^2 L^2}, \qquad r = \frac{r^*}{\sigma H}, \qquad a = \frac{\sigma \kappa_\mathrm{v}}{\omega_\mathrm{s}^2}, \qquad \kappa = \frac{\kappa_\mathrm{h}}{\sigma L^2}, \\ &\gamma = \frac{\omega_\mathrm{s} H}{\kappa_\mathrm{v}}, \qquad \delta_\mathrm{s} = \frac{\alpha U^2}{\rho_\mathrm{s}(1-p)\sigma H}, \qquad \delta_\mathrm{b} = \frac{\hat{s} U^b}{\sigma H L u_\mathrm{c}^b}, \qquad \mu = \frac{\mu_* H}{L}. \end{aligned} \tag{3.2.6}$$

From Table 3.1, it follows that the bedload parameter δ_b is much smaller than the suspended load parameter δ_s, i.e. $\delta_\mathrm{b} \ll \delta_\mathrm{s}$. From the nondimensional bottom evolution equation (3.2.5), it follows that the leading order rate of change of the bottom scales with the larger suspended load parameter δ_s, hence $\partial h^*/\partial t^* \sim \delta_\mathrm{s}$. Thus the term $1/\varepsilon\, \partial h^*/\partial t^*$ found in the conservation of mass equation (3.2.2) scales with $1/\varepsilon\, \partial h^*/\partial t^* \sim \delta_\mathrm{s}/\varepsilon \sim 10^{-3}$. The other terms in the conservation of mass equation (3.2.2) are order one and, hence, this term can safely be neglected. The nondimensional conservation of mass equation (3.2.2) therefore reduces to

$$\frac{\partial \zeta}{\partial t} + \frac{\partial}{\partial x}\big[(1 + \varepsilon\zeta - h)u\big] = 0. \tag{3.2.7}$$

Furthermore, in Table 3.1 can be seen that $\Lambda \gg 1$. When comparing Λ to the other terms in the nondimensional conservation of momentum equation (3.2.3) it is found that this is the only large term. Hence this is the dominant term and, therefore, the conservation of momentum equation (3.2.3) reduces to

$$\frac{\partial \zeta}{\partial x} = 0. \tag{3.2.8}$$

Table 3.1: Characteristic values of the Ameland inlet system. The dimensionless parameters are summarised in equation (3.2.6). Courtesy of Schuttelaars (1997); Ter Brake (2011).

Channel	Sediment	Dimensionless
$L = 1.9 \cdot 10^4\,\mathrm{m}$	$\alpha = 0.005\,\mathrm{kg\,s\,m^{-4}}$	$\varepsilon \sim 7.1 \cdot 10^{-2}$
$B = 2 \cdot 10^3\,\mathrm{m}$	$\omega_\mathrm{s} = 0.015\,\mathrm{m\,s^{-1}}$	$\Lambda \sim 1.7 \cdot 10^1$
$H = 12\,\mathrm{m}$	$\kappa_\mathrm{v} = 0.1\,\mathrm{m^2\,s^{-1}}$	$r \sim 2.4 \cdot 10^{-1}$
	$\kappa_\mathrm{h} = 10^2\,\mathrm{m^2\,s^{-1}}$	$a \sim 6.2 \cdot 10^{-2}$
Tide	$\rho_\mathrm{s} = 2650\,\mathrm{kg\,m^{-3}}$	$\kappa \sim 2.0 \cdot 10^{-3}$
$\sigma = 1.4 \cdot 10^{-4}\,\mathrm{rad\,s^{-1}}$	$d = 1.3 \cdot 10^{-4}\,\mathrm{m}$	$\gamma \sim 1.8$
$A = 0.84\,\mathrm{m}$	$p = 0.4$	$\delta_\mathrm{s} \sim 6.8 \cdot 10^{-5}$
$U = 0.19\,\mathrm{m\,s^{-1}}$	$\hat{s} = 3 \cdot 10^{-6}\,\mathrm{m\,s^{-1}}$	$\delta_\mathrm{b} \sim 2.4 \cdot 10^{-8}$
	$u_\mathrm{c} = 0.3\,\mathrm{m\,s^{-1}}$	$\mu \sim 1.3 \cdot 10^{-3}$
Constant	$\mu_* = 2$	
$g = 9.81\,\mathrm{m\,s^{-2}}$	$b = 3$	
$r^* = 4 \cdot 10^{-4}\,\mathrm{m\,s^{-1}}$		

Observations show that the main driver of horizontal sediment transport is the tide. Waves mostly influence the vertical transport of sediment and this process can be incorporated into the model by enhancing the erosion parameter α. The free surface ζ prescribed at the entrance of the embayment is therefore periodic and by equation (3.2.8) it directly follows that the free surface in the rest of the domain is periodic. The flow velocity u that depends on the free surface via equation (3.2.7) therefore also has the same periodicity. From equation (3.2.4) it follows that the suspended sediment transport is forced by the flow velocity u, thus C is periodic but also has a residual component. Since the equations are nondimensionalized the tidal periodic functions are transformed into 2π-periodic functions. Since $\delta_\mathrm{s} \gg \delta_\mathrm{b}$, the leading order nondimensional bottom evolution equation reads

$$\frac{\partial h^*}{\partial t^*} = -\delta_\mathrm{s}\big((u^*)^2 - \beta C^*\big). \tag{3.2.9}$$

As explained above, u^* and C^* are 2π-periodic functions. Since the bottom evolves slowly in time due to the presence of the small parameter δ_s and since the RHS is order one periodic, the method of averaging can be applied for each fixed spatial coordinate[1] (Verhulst, 1990). Thus the bottom evolves so slowly that it can be considered constant on the fast 2π time scale and averaging over the fast time is justified (Schuttelaars, 1997; Ter Brake, 2011). Moreover, Krol (1990, p. 75) has shown, for a system very similar to ours, that the method of averaging can be applied to obtain accurate results on a long time scale. The error is order $\mathcal{O}(\delta_\mathrm{s})$ on a $1/\delta_\mathrm{s}$ time scale. The bottom evolution equation averaged over the fast time scale is given by

$$\frac{\partial h^*}{\partial t^*} = -\delta_\mathrm{s}\Big\langle (u^*)^2 - \beta C^* \Big\rangle, \tag{3.2.10}$$

where $\langle\,\cdot\,\rangle$ denotes the 2π tidal average.

The whirling up and settling down of the sediment is perfectly balanced by the horizontal transport of sediment as described by the concentration equation (3.2.4). Substitution of the concentration equation into the averaged bottom evolution equation results in

$$\frac{\partial h^*}{\partial t^*} = -\delta_\mathrm{s} a \frac{\partial}{\partial x^*}\left[\varepsilon\big\langle u^* C^* \big\rangle - \kappa\left(\frac{\partial}{\partial x^*}\big\langle C^* \big\rangle + \gamma\beta \frac{\partial h^*}{\partial x^*}\big\langle C^* \big\rangle\right)\right], \tag{3.2.11}$$

since the term $\big\langle \partial C^*/\partial t \big\rangle$ vanishes as C^* is 2π-periodic and since $\partial h^*/\partial x^*$ can be taken out of the averaging procedure. This follows because h^* only changes significantly on the morphological time scale.

The asterisk superscript, denoting that a variable is nondimensional and order one, is omitted from now

[1] that is, for ordinary differential equations

on. To summarise, the leading order nondimensional hydro-morphodynamic equations are given by

$$\begin{cases} \dfrac{\partial \zeta}{\partial t} + \dfrac{\partial}{\partial x}\big[(1+\varepsilon\zeta - h)u\big] = 0, & \text{(3.2.12a)} \\ \dfrac{\partial \zeta}{\partial x} = 0, & \text{(3.2.12b)} \\ a\left\{ \dfrac{\partial C}{\partial t} + \varepsilon \dfrac{\partial uC}{\partial x} - \kappa\left(\dfrac{\partial^2 C}{\partial x^2} + \gamma \dfrac{\partial}{\partial x}\left[\beta \dfrac{\partial h}{\partial x} C\right]\right)\right\} = u^2 - \beta C, & \text{(3.2.12c)} \\ \dfrac{\partial h}{\partial t} = -\dfrac{\partial \langle F\rangle}{\partial x}, & \text{(3.2.12d)} \end{cases}$$

where the tidally averaged flux $\langle F\rangle$ is given by

$$\langle F\rangle = \delta_{\mathrm{s}} a\left[\varepsilon\big\langle uC\big\rangle - \kappa\left(\frac{\partial\langle C\rangle}{\partial x} + \gamma\beta\frac{\partial h}{\partial x}\langle C\rangle\right)\right]. \tag{3.2.13}$$

Here, $\varepsilon\langle uC\rangle$ represents advective transport, $\kappa\,\partial\langle C\rangle/\partial x$ diffusive transport and $\kappa\gamma\beta\,\partial h/\partial x\,\langle C\rangle$ topologically induced diffusive transport.

The characteristic scales as given by equation (3.2.1) are substituted into the dimensional boundary conditions given in section 3.1.5. Identifying the nondimensional variables as defined in equation (3.2.6), yield the nondimensional boundary conditions:

$$\begin{aligned} \zeta &= \cos t && \text{at} \quad x = 0, && \text{(3.2.14a)} \\ (1+\varepsilon\zeta - h)u &= 0 && \text{at} \quad x = 1, && \text{(3.2.14b)} \\ \varepsilon\big\langle uC\big\rangle - \kappa\left(\frac{\partial\langle C\rangle}{\partial x} + \gamma\beta\frac{\partial h}{\partial x}\langle C\rangle\right) &= 0 && \text{at} \quad x = 1, && \text{(3.2.14c)} \\ C'(x,t,\kappa) &= C'(x,t,\kappa=0) && \text{at} \quad x = 0,\ x = 1, && \text{(3.2.14d)} \\ \frac{\partial h}{\partial t} &= 0 && \text{at} \quad x = 0, && \text{(3.2.14e)} \\ \langle F\rangle &= 0 && \text{at} \quad x = 1. && \text{(3.2.14f)} \end{aligned}$$

3.3 Diffusively dominated transport

In this section, the model is solved in the case when diffusive transport dominates the advective and topologically induced transport mechanisms. Thus there is no advective transport, $\varepsilon = 0$, and no topologically induced diffusive transport, $\gamma = 0$.

3.3.1 Solving the model

The simplifications made in the scaling analysis section allow analytical solutions to be determined. The nondimensional conservation of momentum equation (3.2.12b) together with the free surface boundary condition (3.2.14a) imply that

$$\zeta(x,t) = \cos t.$$

Substituting this into the nondimensional conservation of mass equation (3.2.12a), solving for the flow velocity u and using the boundary condition (3.2.14b) with $\varepsilon = 0$ results in

$$u(x,t) = \frac{x-1}{1-h}\sin t. \tag{3.3.1}$$

We assume that the deposition parameter is given by $\beta = 1$ instead of the depth-dependent relation given by equation (3.1.3), as this simplifies the resulting bottom evolution equation considerably. The tidally averaged flux $\langle F\rangle$ as given by equation (3.2.13) only depends on the tidally averaged sediment

concentration. Thus the suspended sediment transport equation (3.2.12c) with $\varepsilon = 0$ and $\gamma = 0$ is tidally averaged and this yields

$$-a\kappa\frac{\partial^2\langle C\rangle}{\partial x^2} = \frac{1}{2}\left(\frac{x-1}{1-h}\right)^2 - \langle C\rangle. \tag{3.3.2}$$

From Table 3.1, it follows that $a\kappa \ll 1$. Thus this ordinary differential equation is singularly perturbed, which allows a boundary layer to form. It is expected that the second derivative of the averaged concentration is small throughout the domain and thus no boundary layers form. This assumption has to be checked a posteriori. A perturbation method is used to find an approximate solution for this problem. For an introduction to perturbation techniques, see for example Holmes (2013). We assume that $\langle C\rangle$ exhibits a regular expansion with respect to $a\kappa$:

$$\langle C\rangle = \langle C_0\rangle + a\kappa\langle C_1\rangle + (a\kappa)^2\langle C_2\rangle + \dots \tag{3.3.3}$$

This regular expansion is substituted into the averaged sediment equation (3.3.2) and the solution of the leading order balance is given by

$$\langle C_0\rangle = \frac{1}{2}\left(\frac{x-1}{1-h}\right)^2. \tag{3.3.4}$$

This solution is regular on the entire domain and also satisfies boundary condition (3.2.14c), thus this is a valid solution on the entire domain. The leading order tidally averaged flux under the assumption of no advective transport, $\varepsilon = 0$, and no topological induced diffusive transport, $\gamma = 0$, is given by $\langle F\rangle = -\delta_s a\kappa\,\partial\langle C_0\rangle/\partial x$. Substitution of the leading order sediment concentration (3.3.4) into the leading order sediment flux yields

$$\langle F\rangle = -\delta_s\frac{a\kappa}{2}\frac{\partial}{\partial x}\left(\frac{x-1}{1-h}\right)^2. \tag{3.3.5}$$

Substitution of the leading order sediment flux (3.3.5) into equation (3.2.12d) yields an explicit evolution equation for the bottom profile:

$$\frac{\partial h}{\partial t} = \delta_s\frac{a\kappa}{2}\frac{\partial^2}{\partial x^2}\left(\frac{x-1}{1-h}\right)^2.$$

The morphological time scale $\tau = a\kappa\delta_s t$ is introduced to simplify the equation. The bottom evolution equation for $h(\tau, x)$ on the morphodynamic time scale becomes

$$\frac{\partial h}{\partial \tau} = \frac{1}{2}\frac{\partial^2}{\partial x^2}\left(\frac{x-1}{1-h}\right)^2. \tag{3.3.6}$$

At equilibrium, the bed no longer changes in time, thus $\partial h/\partial\tau = 0$. The equilibrium bed profile that satisfies both boundary conditions is the simple linear bed profile:

$$h_{\text{eq}} = x. \tag{3.3.7}$$

3.3.2 Linear stability analysis

The linear equilibrium bed profile is perturbed to investigate its stability. The small perturbation on top of the equilibrium bed profile is denoted with $\tilde{h}(x,\tau)$ and satisfies the boundary conditions $\tilde{h}(x=0,\tau) = 0$ and $\langle\tilde{F}\rangle(x=1,\tau) = 0$, i.e. the averaged perturbed flux vanishes at $x = 1$. The linear equilibrium bed profile is given by equation (3.3.7). The perturbed bottom profile $h = h_{\text{eq}} + \tilde{h}$ is substituted into the bottom evolution equation (3.3.6) and the resulting equation is linearised by ignoring the higher order terms in the Taylor series to obtain

$$\frac{\partial\tilde{h}}{\partial\tau} = \frac{\partial^2}{\partial x^2}\left(\frac{\tilde{h}}{1-x}\right).$$

The same result can be obtained using the Fréchet derivative, see e.g. Van Groesen and Molenaar (2007, p. 89) for a definition of the Fréchet derivative. Separation of variables shows that this equation allows solutions of the type

$$\tilde{h}(x,\tau) = g(x)e^{\omega\tau},$$

where the eigenvalue ω and $g(x)$ are determined by the non-trivial solutions of the eigenvalue problem:

$$\frac{d^2}{dx^2}\left(\frac{g}{1-x}\right) = \omega g. \tag{3.3.8}$$

Using the transformations $z = 1 - x$ and $\psi(z) = g/z$, the equation can be written as a Sturm-Liouville eigenvalue problem:

$$\frac{d^2\psi}{dz^2} = \omega z\psi. \tag{3.3.9}$$

The homogeneous boundary conditions transform into $\frac{d\psi}{dz}(z = 0) = 0$ and $\psi(z = 1) = 0$, as we are not interested in the trivial solution. The first boundary condition can be derived by substituting the perturbed bottom profile $h = h_{\text{eq}} + \tilde{h}$ into the flux given by equation (3.3.5), applying the same transformations as above and evaluating the expression at $z = 0$.

Since the weight function $\sigma(z) = z$ is zero at $z = 0$ it follows that this is a irregular Sturm-Liouville eigenvalue problem and the usual results do not directly apply (Haberman, 2005, p. 163). Note that the eigenvalue problem can be written as

$$\mathcal{L}\psi = \omega z\psi,$$

where $\mathcal{L} \equiv d^2/dz^2$ is a linear operator. For any functions u and v that satisfy the homogeneous boundary conditions, it follows using integration by parts twice and using the homogeneous boundary conditions that

$$\int_0^1 v\mathcal{L}u\,dz = \int_0^1 u\mathcal{L}v\,dz,$$

i.e. the linear operator $\mathcal{L}$ with the corresponding boundary conditions is *self-adjoint*. We show that eigenfunctions corresponding to different eigenvalues are orthogonal with respect to the weight $\sigma(z) = z$. Let ω_n and ω_m be two eigenvalues with corresponding eigenfunctions ψ_n and ψ_m. The eigenvalues and eigenfunctions satisfy

$$\mathcal{L}\psi_n = \omega_n z\psi_n \qquad \text{and} \qquad \mathcal{L}\psi_m = \omega_m z\psi_m, \tag{3.3.10}$$

with homogeneous boundary conditions. The operator $\mathcal{L}$ is self-adjoint and therefore it holds that

$$\int_0^1 \psi_m\mathcal{L}\psi_n\,dz = \int_0^1 \psi_n\mathcal{L}\psi_m\,dz.$$

Using that ψ_n and ψ_m are eigenfunctions, i.e. using equation (3.3.10), and bringing everything to one side, reveals that

$$(\omega_n - \omega_m)\int_0^1 \psi_n\psi_m z\,dz = 0. \tag{3.3.11}$$

Thus if the eigenvalues are different, $\omega_n \neq \omega_m$, then ψ_n and ψ_m are orthogonal with respect to the inner product with weight $\sigma(z) = z$. Furthermore by taking the complex conjugate of eigenvalue problem (3.3.10), it follows that $\overline{\omega}_n$ is also an eigenvalue with corresponding eigenfunction $\overline{\psi}_n$:

$$\mathcal{L}\overline{\psi}_n = \overline{\omega}_n z\overline{\psi}_n.$$

The eigenfunction $\overline{\psi}_n$ also satisfies the homogeneous boundary conditions. Since (3.3.11) holds for any pair of eigenvalues and eigenfunctions, it also holds for the complex conjugate eigenvalue and eigenfunction. Hence

$$(\omega_n - \overline{\omega}_n)\int_0^1 \psi_n\overline{\psi}_n z\,dz = 0.$$

Since $\psi_n\overline{\psi}_n z = |\psi_n|^2 z \geq 0$ and since the eigenfunctions are not identically zero, it follows that $\omega_n = \overline{\omega}_n$. Thus all the eigenvalues ω are real.

As all the coefficients of the Sturm-Liouville equation (3.3.9) are real, it follows that eigenfunctions can always be chosen real.

There are three cases left for ω to consider: $\omega < 0$, $\omega = 0$ and $\omega > 0$. If $\omega = 0$ then all the solutions of the Sturm-Liouville equation are linear functions. Application of the homogeneous boundary conditions

shows that this case always results in the trivial solution. For $\omega \neq 0$, eigenvalue problem (3.3.9) is multiplied with ψ and integrated over the domain. The resulting equation is solved for the eigenvalue ω. By using integration by parts and the homogeneous boundary conditions, the Rayleigh Quotient is found:

$$\omega = -\frac{\int_0^1 (\frac{\partial \psi}{\partial z})^2 \, dz}{\int_0^1 \psi^2 z \, dz}.$$

Since the eigenfunctions are real, it follows that $(\frac{\partial \psi}{\partial z})^2 \geq 0$, $\psi^2 z \geq 0$. Furthermore, since the eigenfunctions are not identically zero, it follows that all eigenvalues are negative: $\omega < 0$, as $\omega = 0$ is already excluded.

We note that the Sturm-Liouville equation, (3.3.9), is a generalised Airy differential equation. Using the transformation $\hat{\xi} = \sqrt[3]{\omega} z$ the equation can be written in the standard Airy differential equation form where a linear combination of the Airy functions is a solution. However, the solution in terms of the Airy functions turns out to be inconvenient. Instead, we apply the transformation $\xi = \sqrt[3]{-\omega} z$ to obtain

$$\frac{d^2\psi}{d\xi^2} + \xi\psi = 0,$$

where $\xi \geq 0$ since $\omega < 0$ and $z \geq 0$. Define $\phi(\xi) = \psi(\xi)/\sqrt{\xi}$, then the second order differential equation becomes

$$\sqrt{\xi}\frac{d^2\phi}{d\xi^2} + \frac{1}{\sqrt{\xi}}\frac{d\phi}{d\xi} + \left(\xi\sqrt{\xi} - \frac{1}{4}\frac{1}{\xi\sqrt{\xi}}\right)\phi = 0.$$

Finally, using the coordinate transformation $\eta = \frac{2}{3}\xi\sqrt{\xi}$ and multiplying with η, results in Bessel's differential equation:

$$\eta^2\frac{d^2\phi}{d\eta^2} + \eta\frac{d\phi}{d\eta} + \left(\eta^2 - \frac{1}{9}\right)\phi = 0.$$

The orders of the Bessel function are found from the equation $\nu^2 = \frac{1}{9}$ and, therefore, the orders of the Bessel functions are $\nu = \pm\frac{1}{3}$. The solution of Bessel's differential equation is

$$\phi(\eta) = AJ_{\frac{1}{3}}(\eta) + BJ_{-\frac{1}{3}}(\eta),$$

where J_ν is the Bessel function of order ν. Transforming back to $\psi(z)$ yields the desired form of the solution:

$$\psi(z) = A\sqrt{z}J_{\frac{1}{3}}\left(\frac{2}{3}\sqrt{-\omega}z^{3/2}\right) + B\sqrt{z}J_{-\frac{1}{3}}\left(\frac{2}{3}\sqrt{-\omega}z^{3/2}\right),$$

where the factor $\sqrt[6]{-\omega}$ has been absorbed into the coefficients A and B, which is allowed since ω is a nonzero constant.

Application of boundary condition $\frac{d\psi}{dz}(z = 0^+) = 0$ shows that $A = 0$ since the derivative of the second term vanishes at 0^+. The second boundary condition $\psi(z = 1) = 0$ now implies that

$$J_{-\frac{1}{3}}\left(\frac{2}{3}\sqrt{-\omega}\right) = 0, \tag{3.3.12}$$

since for non-trivial solutions $B \neq 0$. That is, all the eigenvalues ω are directly related to the zeros of the Bessel function of order $-1/3$.

Transforming back to $\tilde{h}$ shows that the small perturbations on top of equilibrium bed profile (3.3.6) satisfy

$$\tilde{h}(x, \tau) = B(1 - x)^{3/2}J_{-\frac{1}{3}}\left(\frac{2}{3}\sqrt{-\omega}(1 - x)^{3/2}\right)e^{\omega\tau},$$

where ω can be determined from equation (3.3.12). Since $\omega < 0$, it follows that all the perturbations of the equilibrium bed profile decay in time, thus the equilibrium bed profile $h_{\text{eq}} = x$ is asymptotically linear stable.

3.3.3 Temporal evolution towards equilibrium

The nonlinear equation (3.3.6) is solved numerically to investigate the temporal evolution of the bottom profile. A Finite Element Method (FEM) is used for the spatial discretization, the θ-scheme is used for the temporal discretization and the resulting nonlinear system is solved with the Newton-Raphson method, see Appendix B.1 for a derivation and validation of the numerical schemes. The FEM discretization uses linear elements and $n = 1000$ spatial nodes. The temporal discretization uses $\theta = 1/2$ and time step $\Delta t = 10^{-3}$.

The landwards no-flux boundary

Implementing the nonlinear no-flux boundary condition (3.2.14f) at the end of the embayment is not a trivial task, since the nonlinear partial differential equation (3.3.6) and the condition itself become singular whenever $h \to 1$. Previous approaches found in literature are not fully satisfactory. Van Dongeren and De Vriend (1994) used the implied condition that the velocity is zero at $x = 1$ for a slightly different model. As pointed out by the authors, at the landward side the bottom profile did not evolve towards the analytical equilibrium bottom profile but instead contained an unphysically sharp drop at the right boundary. In Schuttelaars and De Swart (1996); Van Leeuwen (2002) the no-flux boundary condition was replaced by a homogeneous Neumann condition. This produced better results but still, the numerical solution contained a small unphysical corner at the landward side, which lead to a small discrepancy between the equilibrium solution and numerical solution at the landward side.

A numerical scheme is derived in Appendix B.1 that uses the no-flux boundary condition (3.2.14f). However, using this boundary condition it is found that the discretization matrix becomes singular. To overcome this problem, the Dirichlet boundary condition $h = 1$ at $x = 1$ is used instead. The vanishing water transport boundary condition (3.2.14b) implies that whenever $h = 1$, the velocity u should be finite at $x = 1$ and not necessarily that $u = 0$ as is the case if $h \neq 1$. It was shown in Appendix B.1.2 that when using the Dirichlet boundary condition, the natural no-flux boundary condition is automatically applied at the previous grid node using our FEM discretization. Thus the no-flux boundary condition is still satisfied when using the Dirichlet boundary condition, albeit at a grid cell before the actual boundary. Below, the used Dirichlet boundary condition is derived from the no-flux condition when an additional constraint is imposed.

Dirichlet condition The no-flux boundary condition is subjected to an additional constraint to derive a simpler numerical boundary condition. Expanding the derivatives of the no-flux boundary condition (3.3.5) and simplifying this result yields the condition:

$$\langle F \rangle \propto \frac{(x-1)\Big(1-h+\frac{\partial h}{\partial x}(x-1)\Big)}{(1-h)^3} = 0 \quad \text{at} \quad x = 1.$$

To obtain an unambiguous boundary condition an extra condition is imposed. Namely that the no-flux boundary condition should still be consistent when applied at any $x \leq 1$ arbitrarily close to 1:

$$\langle F \rangle \propto \frac{(x-1)\Big(1-h+\frac{\partial h}{\partial x}(x-1)\Big)}{(1-h)^3} = 0 \quad \text{at} \quad x \leq 1.$$

Note that at morphodynamic equilibrium the flux vanishes in the whole domain and this condition is certainly satisfied.

Then for any $x < 1$ it follows that $x - 1 < 0$ and that $h < 1$ such that $1 - h > 0$. The no-flux boundary condition reduces to

$$1 - h + \frac{\partial h}{\partial x}(x-1) = 0 \quad \text{for} \quad x < 1.$$

This condition shows in the limit $x \to 1$ that h should satisfy:

$$h = 1 \quad \text{at} \quad x = 1.$$

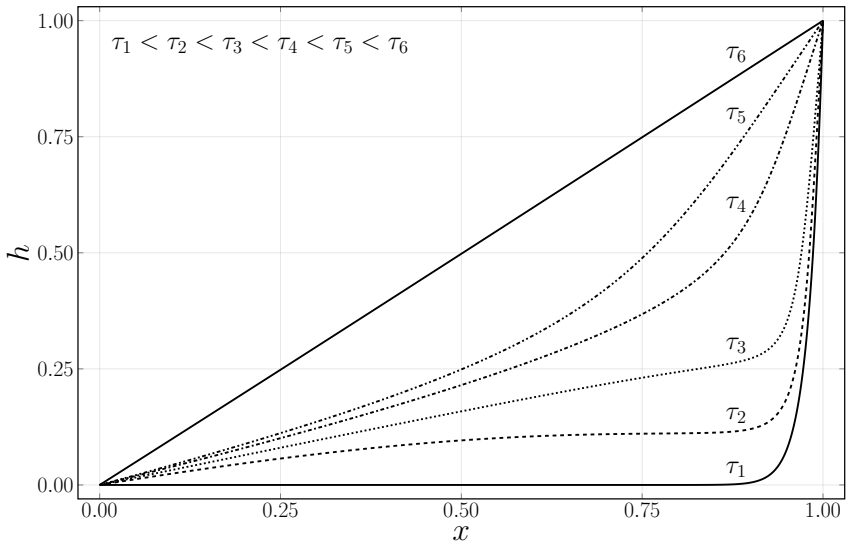

Figure 3.3: Evolution of an initially nearly flat bottom towards the linear equilibrium bottom profile (3.3.7) in the diffusively dominated transport case. The bottom profile is shown at $\tau_1 = 0$, $\tau_2 = 0.1$, $\tau_3 = 0.2$, $\tau_4 = 0.35$, $\tau_5 = 0.45$ and $\tau_6 = 1.2$. The numerical solution is computed with $n = 1000$ spatial nodes and time step $\Delta t = 10^{-3}$.

This result is consistent with the linear equilibrium bottom profile at $x = 1$, is physically justified as the seabed should be continuous when going from the edge of the basin ($x < 1$) to the unmodelled beach ($x > 1$) and is supported by the scaling of the nondimensional model.

Nearly flat bottom initially

Figure 3.3 shows the evolution of an initially nearly flat bed towards the linear equilibrium bottom profile (3.3.7). Initially, at τ_1, the bottom profile is given by $h = x^{50}$. This can be interpreted as an excavated basin which is continuous at the landward side, $x = 1$. Some time later, at τ_2 and τ_3, the sediment is distributed fairly evenly along the basin. The time stamps τ_4 and τ_5 show that most sediment is deposited at the landward side. Finally, at τ_6, the rest of the basin is filled with sediment such that the linear equilibrium profile is obtained, as predicted by equation (3.3.7).

The steady linear bottom profile is acquired after approximately 30,000 years for the parameter values given in Table 3.1. Observations show that the bottom in tidal embayments typically evolves in the order of 20 years (Schuttelaars, 1997, p. 22). Hence, the time scale to reach equilibrium as predicted by the model is extremely long. This extremely long time scale can be explained by the fact that the basin is initially almost empty. Then the slow diffusive transport needs to transport all the sediment from the seaward side into the long and narrow basin. Moreover, the time scales reported by observations only indicate the time scales at which bathymetric changes occur and are not suitable to describe the time scales needed to reach equilibrium. Hence, the evolution towards the linear equilibrium profile from the initially nearly flat bottom is expected to take a very long time.

Furthermore, the evolution from the nearly flat bottom profile towards the linear equilibrium bottom profile (3.3.7) suggests that the linear bottom profile is not only asymptotically linear stable, as proven in Section 3.3.2, but is also globally stable.

Comparison between eigenvalues

The ten largest eigenvalues of the continuous operator (3.3.8), the roots of the Bessel function, and of the discretized operator (B.1.7) are shown in Figure 3.4. Both operators are linearised around the linear equilibrium profile (3.3.7). It can be seen that the ten largest eigenvalues of both operators are in good agreement. The smallest eigenvalues of the discretized operator for $n = 1000$ nodes do not agree with

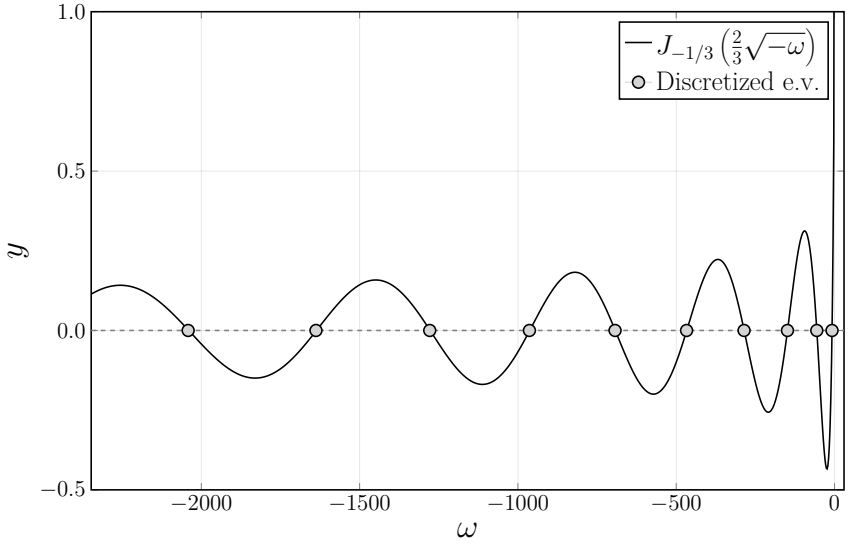

Figure 3.4: The ten largest eigenvalues of the continuous operator (3.3.8) and the discretized operator or matrix (B.1.7) when linearised around the linear equilibrium profile (3.3.7). The eigenvalues of the continuous operator are exactly the roots of the Bessel function $J_{-1/3}\left(\frac{2}{3}\sqrt{-\omega}\right)$, see equation (3.3.12). The eigenvalues of the discrete operator are obtained after correcting for the factor Δx resulting from the FEM discretization. The eigenvalues of the discretized operator are shown as light grey dots and are computed with $n = 1000$ nodes.

those of the continuous operator (not shown here). However, in the limit of $\Delta x \to 0$, all the eigenvalues of the discretized operator approach those of the continuous operator, indicating that the numerical problem approaches the analytical problem and, therefore, indicating that the numerical solution approaches the analytical solution.

Chapter 4

The morphodynamics of a one-dimensional idealised sea-basin system

In this chapter, the one-dimensional idealised sea-basin system is introduced. The geometry of the sea-basin system is presented and a novel approach to model the sea-basin interaction is explained. Then the equations that govern the morphodynamics of the sea-basin system are discussed. Two methods are used to solve these hydro-morphodynamic equations and their results are compared. Lastly, the temporal evolution and stability of the sea-basin system are investigated.

4.1 The one-dimensional idealised sea-basin system

The seawards boundary condition used in Chapter 3 assumes a fixed depth at the entrance of the embayment. The embayment is nondimensionalized using this depth and the same fixed depth is present in the computed equilibrium profiles. To allow other equilibrium entrance heights to occur and to investigate the behaviour of the bottom profile at the entrance of the basin, the seaside boundary is replaced by a boundary at sea, far away from the entrance of the basin.

The geometry of the nondimensionalized sea-basin system is shown in Figure 4.1. The one-dimensional spatial domain is split into two parts: a sea domain and a basin domain. The sea domain ranges from $x = 0$ to $x = x_\mathrm{i}$, the interface between the sea and the basin, and the basin domain starts at $x = x_\mathrm{i}$ and stops at $x = 1$.

The state vector, containing the free surface ζ, the along-channel flow velocity u, the averaged concentration $\langle C \rangle$ and the bottom profile h, is defined as

$$\Psi = (\zeta,\, u,\, \langle C \rangle, h). \tag{4.1.1}$$

The state vector in the sea consists of a basic state $\Psi_\mathrm{s}^\mathrm{b}$, which is the solution when the entrance to the basin is blocked, and a response state $\Psi_\mathrm{s}^\mathrm{r}$, which is the response in the sea domain when the entrance to the basin is opened. Similarly, in the basin the basic state is $\Psi_\mathrm{b}^\mathrm{b}$, which is the solution when the entrance to the basin is closed, and the response state is $\Psi_\mathrm{b}^\mathrm{r}$, which is the response in the basin when the entrance is opened.

If the basin is closed off, then there is no forcing acting on the basic basin state $\Psi_\mathrm{b}^\mathrm{b}$. Furthermore, since the hydro-morphodynamic equations and boundary conditions are homogeneous, it follows that the free surface inside the basin remains flat, the water in the basin is at rest and there is no suspended sediment inside the basin. The basic basin bed can be chosen arbitrarily. To simplify the forthcoming analysis, the basic basin bed is assumed to vanish. Thus we have for the basic basin state that $\Psi_\mathrm{b}^\mathrm{b} = \mathbf{0}$. However,

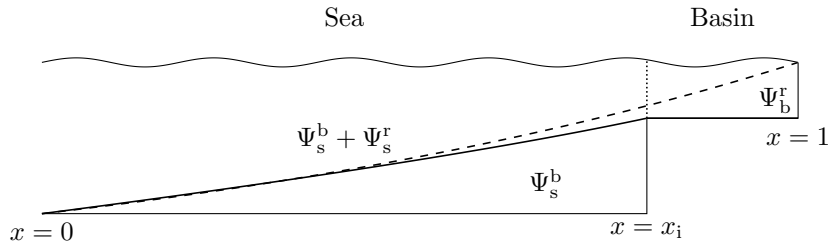

Figure 4.1: Cross-sectional view of the sea-basin system. The seaside solid line is the bed profile of the basic sea state $\Psi_{\mathrm{s}}^{\mathrm{b}}$, which is Dean's profile (4.1.2) with $d = 0.97$. The dashed line indicates the bottom profile in response to opening the basin.

one could also assume, for example, that the basic basin bed is flat and the height is chosen such that the bed is continuous at the basin entrance, as is shown in Figure 4.1.

Assuming that the wave breaking process of offshore waves results in chaotic turbulent fluctuations, Dean argues that these fluctuations are destructive forces which change the bed slope until an equilibrium beach profile is reached. Assuming that the dominant destructive force is wave energy dissipation per volume, Dean (1991) has shown that the equilibrium bottom profile is given by

$$h_{\mathrm{D}}(x) = 1 - (1 - dx)^{2/3}, \tag{4.1.2}$$

where d is a scaling parameter. We require that the bottom profile of the basic sea state, i.e. when the basin is closed off, is given by Dean's bed profile, that is $h_{\mathrm{s}}^{\mathrm{b}} = h_{\mathrm{D}}$.

The idea is to first determine the basic state inside the sea $\Psi_{\mathrm{s}}^{\mathrm{b}}$ and in the basin $\Psi_{\mathrm{b}}^{\mathrm{b}}$ that satisfy the constraints given above and then determine the response in the sea $\Psi_{\mathrm{s}}^{\mathrm{r}}$ and in the basin $\Psi_{\mathrm{b}}^{\mathrm{r}}$ when the basin is opened such that the hydro-morphodynamic equations (3.2.12a–d) are satisfied. Figure 4.1 summarises the set-up of the sea basin system.

4.1.1 The hydro-morphodynamic equations

On both domains, the hydro-morphodynamic equations (3.2.12a–d) need to be satisfied together with boundary conditions (3.2.14a–f). We again assume diffusively dominated transport, thus $\varepsilon = \gamma = 0$, and the simple constant deposition parameter $\beta = 1$. The suspended sediment transport equation (3.2.12c) is tidally averaged. The simplified hydro-morphodynamic equations, valid on the whole domain, are then given by

$$\begin{cases} \dfrac{\partial \zeta}{\partial t} + \dfrac{\partial}{\partial x}\big[(1-h)u\big] = 0, & \text{(4.1.3a)} \\ \dfrac{\partial \zeta}{\partial x} = 0, & \text{(4.1.3b)} \\ -a\kappa \dfrac{\partial^2 \langle C \rangle}{\partial x^2} = \langle u^2 \rangle - \langle C \rangle, & \text{(4.1.3c)} \\ \dfrac{\partial h}{\partial \tau} = -\dfrac{\partial \langle F_{\mathrm{diff}} \rangle}{\partial x} + f_{\mathrm{s}} H(x_{\mathrm{i}} - x), & \text{(4.1.3d)} \end{cases}$$

where the averaged and scaled diffusive flux is given by

$$\langle F_{\mathrm{diff}} \rangle = -\frac{\partial \langle C \rangle}{\partial x}. \tag{4.1.4}$$

Here, $\tau = \delta_{\mathrm{s}} a\kappa t$ is the morphological time scale, f_{s} is a source term which is added to parametrise the vastly different dynamics inside the sea, x_{i} the location of the sea basin interface and $H(x_{\mathrm{i}} - x)$ is the Heaviside step function which ensures that the hydro-morphodynamic equations inside the basin are unaltered.

The source term f_s is unknown and has to be determined such that Dean's equilibrium bottom profile is the equilibrium seabed solution of the hydro-morphodynamic equations in the sea if the entrance to the basin is closed off.

4.2 Solving the one-dimensional idealised sea-basin system

The sea-basin system is solved using two different methods. In the first method, the domain is split into two parts. The corresponding hydro-morphodynamic equations are solved on each part separately and are then matched at the interface. The second method considers the hydro-morphodynamic equations on the whole domain. Using the source term f_s determined with the first method, a solution is constructed that is valid on the whole domain.

4.2.1 Method 1: Splitting the domain

The scaled domain is split into two parts, a sea domain ranging from $x = 0$ to $x = x_\mathrm{i}$ and a basin domain located between $x = x_\mathrm{i}$ and $x = 1$, as illustrated in Figure 4.1. First, the basic state inside of the sea $\Psi_\mathrm{s}^\mathrm{b}$ is determined from which an explicit expression for the source term f_s can be found. The basic state inside in the basin is assumed to vanish for simplicity, i.e. $\Psi_\mathrm{b}^\mathrm{b} = \mathbf{0}$, and is therefore already known. Then the response systems in the basin and sea are formulated and solved simultaneously using the matching conditions at the interface.

Solving the basic sea state

Substitution of the total sea state $\Psi_\mathrm{s} = \Psi_\mathrm{s}^\mathrm{b} + \Psi_\mathrm{s}^\mathrm{r}$ into the hydro-morphodynamic equations (4.1.3a–d) and requiring that the basic state does not depend on the response state, i.e. it interacts with itself only, yields a system of equations for the basic sea state $\Psi_\mathrm{s}^\mathrm{b}$:

$$\begin{cases} \dfrac{\partial \zeta_\mathrm{s}^\mathrm{b}}{\partial t} + \dfrac{\partial}{\partial x}\Big[\big(1 - h_\mathrm{s}^\mathrm{b}\big)u_\mathrm{s}^\mathrm{b}\Big] = 0, & \text{(4.2.1a)} \\ \dfrac{\partial \zeta_\mathrm{s}^\mathrm{b}}{\partial x} = 0, & \text{(4.2.1b)} \\ -a\kappa \dfrac{\partial^2 \langle C_\mathrm{s}^\mathrm{b} \rangle}{\partial x^2} = \langle (u_\mathrm{s}^\mathrm{b})^2 \rangle - \langle C_\mathrm{s}^\mathrm{b} \rangle, & \text{(4.2.1c)} \\ 0 = -\dfrac{\partial \langle F_\mathrm{s,diff}^\mathrm{b} \rangle}{\partial x} + f_\mathrm{s}, & \text{(4.2.1d)} \end{cases}$$

where the source term f_s is added to incorporate the complex dynamics in the sea and the averaged diffusive flux is given by

$$\langle F_\mathrm{s,diff}^\mathrm{b} \rangle = -\frac{\partial \langle C_\mathrm{s}^\mathrm{b} \rangle}{\partial x}. \tag{4.2.2}$$

Furthermore, it has been taken into account that $\partial h_\mathrm{s}^\mathrm{b}/\partial \tau = 0$ as Dean's profile is time independent.

The boundary conditions are given by equations (3.2.14a–f) but with $x = 1$ replaced by $x = x_\mathrm{i}$, the sea basin interface. Thus, the entrance of the basin represents a closed wall for the basic sea state.

Solving this system of equations is highly similar to solving the systems of equations given in Section 3.3.1 except that the bottom profile is known a priori, namely Dean's bottom profile (4.1.2). Hence, the

solving procedure is omitted. The basic sea state $\Psi_{\mathrm{s}}^{\mathrm{b}}$ solution is given by

$$\zeta_{\mathrm{s}}^{\mathrm{b}}(x,t) = \cos t, \tag{4.2.3a}$$

$$u_{\mathrm{s}}^{\mathrm{b}}(x,t) = \frac{x - x_{\mathrm{i}}}{(1-dx)^{2/3}} \sin t, \tag{4.2.3b}$$

$$\langle C_{\mathrm{s}}^{\mathrm{b}} \rangle(x) = \frac{1}{2} \frac{(x - x_{\mathrm{i}})^2}{(1-dx)^{4/3}}, \tag{4.2.3c}$$

$$h_{\mathrm{s}}^{\mathrm{b}}(x) = 1 - (1-dx)^{2/3}. \tag{4.2.3d}$$

To allow Dean's profile (4.1.2) to be the equilibrium solution of the bottom evolution equation in the sea domain the source term has to be chosen as

$$f_{\mathrm{s}}(x) = -\frac{1}{(1-dx)^{4/3}} - \frac{8d(x-x_{\mathrm{i}})}{3(1-dx)^{7/3}} - \frac{14d^2(x-x_{\mathrm{i}})^2}{9(1-dx)^{10/3}}. \tag{4.2.4}$$

The coupled response systems

The response states of the sea and basin need to be solved simultaneously, contrary to the basic sea state that could be solved in isolation, due to their interaction at the interface. First, the sea response system is introduced, after which the basin response system and the corresponding interface conditions are presented.

The response sea equations Substitution of the total sea state $\Psi_{\mathrm{s}} = \Psi_{\mathrm{s}}^{\mathrm{b}} + \Psi_{\mathrm{s}}^{\mathrm{r}}$ into the hydro-morphodynamic equations (4.1.3a–d) and subtracting the basic sea state equations (4.2.1a–d) results in a set of equations which the response sea state $\Psi_{\mathrm{s}}^{\mathrm{r}}$ should satisfy and reads:

$$\begin{cases} \dfrac{\partial \zeta_{\mathrm{s}}^{\mathrm{r}}}{\partial t} + \dfrac{\partial}{\partial x}\Big[\big(1 - h_{\mathrm{s}}^{\mathrm{b}} - h_{\mathrm{s}}^{\mathrm{r}}\big)u_{\mathrm{s}}^{\mathrm{r}} - h_{\mathrm{s}}^{\mathrm{r}} u_{\mathrm{s}}^{\mathrm{b}}\Big] = 0, & \text{(4.2.5a)} \\ \dfrac{\partial \zeta_{\mathrm{s}}^{\mathrm{r}}}{\partial x} = 0, & \text{(4.2.5b)} \\ -a\kappa \dfrac{\partial^2 \langle C_{\mathrm{s}}^{\mathrm{r}} \rangle}{\partial x^2} = 2\langle u_{\mathrm{s}}^{\mathrm{b}} u_{\mathrm{s}}^{\mathrm{r}} \rangle + \langle (u_{\mathrm{s}}^{\mathrm{r}})^2 \rangle - \langle C_{\mathrm{s}}^{\mathrm{r}} \rangle, & \text{(4.2.5c)} \\ \dfrac{\partial h_{\mathrm{s}}^{\mathrm{r}}}{\partial \tau} = -\dfrac{\partial \langle F_{\mathrm{s,diff}}^{\mathrm{r}} \rangle}{\partial x}. & \text{(4.2.5d)} \end{cases}$$

The seawards boundary conditions are determined in a similar fashion and read

$$\zeta_{\mathrm{s}}^{\mathrm{r}} = 0 \qquad \text{at} \quad x = 0, \tag{4.2.6a}$$

$$h_{\mathrm{s}}^{\mathrm{r}} = 0 \qquad \text{at} \quad x = 0. \tag{4.2.6b}$$

The response basin equations The total basin state is equal to the response state $\Psi_{\mathrm{b}}^{\mathrm{r}}$ since the basic basin state is chosen zero. Hence, the response basin state $\Psi_{\mathrm{b}}^{\mathrm{r}}$ satisfies the hydro-morphodynamic equations (4.1.3a–d) without extra interaction terms:

$$\begin{cases} \dfrac{\partial \zeta_{\mathrm{b}}^{\mathrm{r}}}{\partial t} + \dfrac{\partial}{\partial x}\Big[\big(1 - h_{\mathrm{b}}^{\mathrm{r}}\big)u_{\mathrm{b}}^{\mathrm{r}}\Big] = 0, & \text{(4.2.7a)} \\ \dfrac{\partial \zeta_{\mathrm{b}}^{\mathrm{r}}}{\partial x} = 0, & \text{(4.2.7b)} \\ -a\kappa \dfrac{\partial^2 \langle C_{\mathrm{b}}^{\mathrm{r}} \rangle}{\partial x^2} = \langle (u_{\mathrm{b}}^{\mathrm{r}})^2 \rangle - \langle C_{\mathrm{b}}^{\mathrm{r}} \rangle, & \text{(4.2.7c)} \\ \dfrac{\partial h_{\mathrm{b}}^{\mathrm{r}}}{\partial \tau} = -\dfrac{\partial \langle F_{\mathrm{b,diff}}^{\mathrm{r}} \rangle}{\partial x}. & \text{(4.2.7d)} \end{cases}$$

The boundary conditions at the landwards side are

$$(1-h_{\mathrm{b}}^{\mathrm{r}})u_{\mathrm{b}}^{\mathrm{r}}=0 \qquad \text{at} \quad x=1, \tag{4.2.8a}$$

$$\frac{\partial\langle C_{\mathrm{b}}^{\mathrm{r}}\rangle}{\partial x}=0 \qquad \text{at} \quad x=1, \tag{4.2.8b}$$

$$\langle F_{\mathrm{b,diff}}^{\mathrm{r}}\rangle=0 \qquad \text{at} \quad x=1. \tag{4.2.8c}$$

Interface conditions Integrating the first three hydro-morphodynamic equations (4.1.3a–c) from x_{i}^{-} to x_{i}^{+} and using that all the terms are finite yields three interface conditions, namely continuity of surface height, continuity of water transport and continuity of diffusive sediment transport, respectively. The continuity of sediment concentration, the last interface condition, follows by integrating the tidally averaged concentration equation (4.1.3c) with respect to x and then integrating the resulting equation once more from x_{i}^{-} to x_{i}^{+}. The four interface conditions read

$$\zeta_{\mathrm{s}}^{\mathrm{b}}+\zeta_{\mathrm{s}}^{\mathrm{r}}=\zeta_{\mathrm{b}}^{\mathrm{r}} \qquad \text{at} \quad x=x_{\mathrm{i}}, \tag{4.2.9a}$$

$$(1-h_{\mathrm{s}}^{\mathrm{b}}-h_{\mathrm{s}}^{\mathrm{r}})(u_{\mathrm{s}}^{\mathrm{b}}+u_{\mathrm{s}}^{\mathrm{r}})=(1-h_{\mathrm{b}}^{\mathrm{r}})u_{\mathrm{b}}^{\mathrm{r}} \qquad \text{at} \quad x=x_{\mathrm{i}}, \tag{4.2.9b}$$

$$\frac{\partial\langle C_{\mathrm{s}}^{\mathrm{b}}\rangle}{\partial x}+\frac{\partial\langle C_{\mathrm{s}}^{\mathrm{r}}\rangle}{\partial x}=\frac{\partial\langle C_{\mathrm{b}}^{\mathrm{r}}\rangle}{\partial x} \qquad \text{at} \quad x=x_{\mathrm{i}}, \tag{4.2.9c}$$

$$\langle C_{\mathrm{s}}^{\mathrm{b}}\rangle+\langle C_{\mathrm{s}}^{\mathrm{r}}\rangle=\langle C_{\mathrm{b}}^{\mathrm{r}}\rangle \qquad \text{at} \quad x=x_{\mathrm{i}}. \tag{4.2.9d}$$

Solving the coupled response systems

The conservation of momentum in the sea (4.2.5b) together with boundary condition (4.2.6a) imply

$$\zeta_{\mathrm{s}}^{\mathrm{r}}(x,t)=0.$$

Using the conservation of momentum in the basin (4.2.7b) and the continuity of the free surface at the interface (4.2.9a) yield

$$\zeta_{\mathrm{b}}^{\mathrm{r}}(x,t)=\cos t.$$

The velocity in the basin is obtained using the conservation of mass in the basin (4.2.7a) and the condition of zero mass flux at the landward side (4.2.8a):

$$u_{\mathrm{b}}^{\mathrm{r}}(x,t)=\frac{x-1}{1-h_{\mathrm{b}}^{\mathrm{r}}}\sin t. \tag{4.2.10}$$

The basic sea state is known (4.2.3a–d) and the mass flux at the interface (4.2.9b) is continuous. Then, from the conservation of mass equation (4.2.5a), the velocity in the sea is found as

$$u_{\mathrm{s}}^{\mathrm{r}}(x,t)=\frac{\frac{x-x_{\mathrm{i}}}{(1-dx)^{2/3}}h_{\mathrm{s}}^{\mathrm{r}}+x_{\mathrm{i}}-1}{(1-dx)^{2/3}-h_{\mathrm{s}}^{\mathrm{r}}}\sin t.$$

It is assumed that $\langle C_{\mathrm{b}}^{\mathrm{r}}\rangle$ exhibits a regular expansion with respect to $a\kappa$, see equation (3.3.3). Substitution of the response basin velocity (4.2.10) into equation (4.2.7c) shows that the leading order solution is given by

$$\langle C_{\mathrm{b}}^{\mathrm{r}}\rangle=\frac{1}{2}\left(\frac{x-1}{1-h_{\mathrm{b}}^{\mathrm{r}}}\right)^{2}.$$

Similarly, from the averaged sediment concentration equation in the sea (4.2.5c), the leading order suspended sediment concentration is determined to be

$$\langle C_{\mathrm{s}}^{\mathrm{r}}\rangle=\frac{-\frac{1}{2}\frac{(x-x_{\mathrm{i}})^{2}}{(1-dx)^{4/3}}(h_{\mathrm{s}}^{\mathrm{r}})^{2}+\frac{(x-x_{\mathrm{i}})^{2}}{(1-dx)^{2/3}}h_{\mathrm{s}}^{\mathrm{r}}+(x_{\mathrm{i}}-1)(x-x_{\mathrm{i}})+\frac{1}{2}(x_{\mathrm{i}}-1)^{2}}{\left((1-dx)^{2/3}-h_{\mathrm{s}}^{\mathrm{r}}\right)^{2}}.$$

Substituting the leading order sediment concentration into the bottom evolution equation (4.2.7d) and results in the bottom evolution equation in the basin on the morphological time scale:

$$\frac{\partial h_{\mathrm{b}}^{\mathrm{r}}}{\partial \tau} = \frac{1}{2}\frac{\partial^2}{\partial x^2}\left(\frac{x-1}{1-h_{\mathrm{b}}^{\mathrm{r}}}\right)^2. \tag{4.2.11}$$

The leading order sea response sediment concentration $\langle C_{\mathrm{s}}^{\mathrm{r}}\rangle$ is substituted into the sea response bottom evolution equation (4.2.5d) to obtain the response sea bottom evolution equation on the morphological time scale:

$$\frac{\partial h_{\mathrm{s}}^{\mathrm{r}}}{\partial \tau} = \frac{\partial^2}{\partial x^2}\left(\frac{-\frac{1}{2}\frac{(x-x_{\mathrm{i}})^2}{(1-dx)^{4/3}}(h_{\mathrm{s}}^{\mathrm{r}})^2 + \frac{(x-x_{\mathrm{i}})^2}{(1-dx)^{2/3}}h_{\mathrm{s}}^{\mathrm{r}} + (x_{\mathrm{i}}-1)(x-x_{\mathrm{i}}) + \frac{1}{2}(x_{\mathrm{i}}-1)^2}{\left((1-dx)^{2/3}-h_{\mathrm{s}}^{\mathrm{r}}\right)^2}\right). \tag{4.2.12}$$

Steady state An analytical answer can be obtained for the *equilibrium* bottom profile. At steady state $\partial h_{\mathrm{b}}^{\mathrm{r}}/\partial t = 0$ and from equation (4.2.11) and boundary condition (4.2.8b), it follows that $\partial\langle C_{\mathrm{b}}^{\mathrm{r}}\rangle/\partial x = 0$ in the entire basin. Using equation (4.2.3c) it can be readily computed that $\partial\langle C_{\mathrm{s}}^{\mathrm{b}}\rangle/\partial x = 0$. Thus interface condition (4.2.9c) simplifies to

$$\frac{\partial\langle C_{\mathrm{s}}^{\mathrm{r}}\rangle}{\partial x} = 0 \quad \text{at} \quad x = x_{\mathrm{i}}. \tag{4.2.13}$$

At steady state the bottom profile of the sea response is also constant in time and thus $\partial h_{\mathrm{s}}^{\mathrm{r}}/\partial t = 0$. Integrating the bottom evolution equation for the response seabed (4.2.12) twice, using the ABC formula to solve the resulting quadratic equation in $h_{\mathrm{s}}^{\mathrm{r}}$ and using boundary conditions (4.2.6b) and (4.2.13) yields

$$h_{\mathrm{s}}^{\mathrm{r}}(x) = (1-dx)^{2/3}\left(1 + \frac{x-1}{\sqrt{(x-x_{\mathrm{i}})^2 + (1-x_{\mathrm{i}}^2)(1-dx)^{4/3}}}\right). \tag{4.2.14}$$

The continuity of sediment interface condition (4.2.9d) implies continuity of the bed:

$$h_{\mathrm{s}}^{\mathrm{b}} + h_{\mathrm{s}}^{\mathrm{r}} = h_{\mathrm{b}}^{\mathrm{r}} \quad \text{at} \quad x = x_{\mathrm{i}}. \tag{4.2.15}$$

Using that $\partial h_{\mathrm{b}}^{\mathrm{r}}/\partial t = 0$, the bottom evolution equation in the basin can be integrated twice and application of boundary conditions (4.2.8c) and (4.2.15) results in the equilibrium bed profile in the basin:

$$h_{\mathrm{b}}^{\mathrm{r}}(x) = 1 + \frac{x-1}{\sqrt{1-x_{\mathrm{i}}^2}}. \tag{4.2.16}$$

This equilibrium basin bed profile (4.2.16) is linear in x. This is the same spatial dependency as the equilibrium basin bed profile (3.3.7) of Chapter 3, when solely an idealised basin was considered.

Furthermore, the equilibrium basin entrance height can be determined from the equilibrium basin bed profile and is given by

$$h_{\mathrm{eq}}(x_{\mathrm{i}}) = 1 + \frac{x_{\mathrm{i}}-1}{\sqrt{1-x_{\mathrm{i}}^2}}. \tag{4.2.17}$$

It is remarkable that the equilibrium entrance height is independent of d, the parameter that determines the basin entrance height when the basin is closed off. The relation between the equilibrium entrance height and the interface location x_{i} is plotted in Figure 4.2.

4.2.2 Method 2: The entire domain

Instead of splitting the domain into two parts one can also consider the system of equations on the whole domain. An explicit expression for f_{s} can be derived by similar means as method 1.

The to be solved hydro-morphodynamic equations are given by equations (4.1.3a–d), the boundary conditions by equations (3.2.14a–f) and the source term by equation (4.2.4).

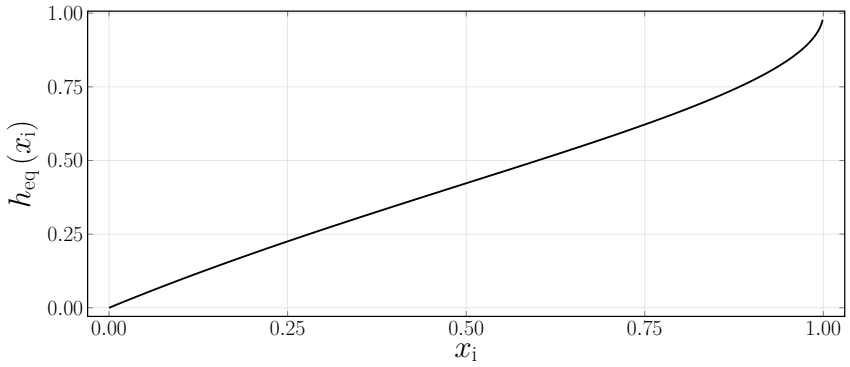

Figure 4.2: The entrance height $h_{\mathrm{eq}}(x_{\mathrm{i}})$ as a function of the interface location x_{i} according to equation (4.2.17).

Solving the first part of this system is similar to what was done in section 3.3.1 and is omitted. The first part of the solution is

$$\zeta(x,t) = \cos t, \tag{4.2.18a}$$

$$u(x,t) = \frac{x-1}{1-h}\sin t, \tag{4.2.18b}$$

$$\langle C\rangle(x) = \frac{1}{2}\left(\frac{x-1}{1-h}\right)^2. \tag{4.2.18c}$$

The bottom profile on the morphological time scale $\tau = \delta_{\mathrm{s}} a\kappa t$ satisfies the equation

$$\frac{\partial h}{\partial \tau} = \frac{1}{2}\frac{\partial^2}{\partial x^2}\left(\frac{x-1}{1-h}\right)^2 + f_{\mathrm{s}} H(x_{\mathrm{i}} - x). \tag{4.2.19}$$

At steady state the last equation can be integrated twice and using boundary conditions (3.2.14e) and (3.2.14f) yields an equilibrium bottom profile that is valid in the sea and basin domain:

$$h_{\mathrm{eq}}(x) = 1 + \frac{x-1}{\sqrt{1 - x_{\mathrm{i}}^2 + \frac{(x-x_{\mathrm{i}})^2}{(1-dx)^{4/3}} H(x_{\mathrm{i}} - x)}}. \tag{4.2.20}$$

4.2.3 Comparison between the two methods

In the basin, i.e. $x > x_{\mathrm{i}}$, it follows that the Heaviside step functions vanishes and the equilibrium bottom profile (4.2.20) reduces to the equilibrium bottom profile (4.2.16) determined using method 1.

Similarly, in the sea it holds that $x < x_{\mathrm{i}}$ and it can be shown that equilibrium bottom profile (4.2.20) is equivalent to the sum of the basic sea bottom profile (4.2.3d) and the sea response profile (4.2.14).

Thus the two methods produce the same result. The first method is more elaborate but provides more insight into the physical processes, while the second method is more straightforward to apply if the forcing is known.

4.2.4 Linear stability analysis

The equilibrium bed profile (4.2.20) is perturbed to investigate its stability. The small perturbation on top of the equilibrium bed profile is denoted with $\tilde{h}(x,\tau)$. The perturbed bottom profile $h = h_{\mathrm{eq}} + \tilde{h}$ is substituted into the bottom evolution equation (4.2.19) and the resulting equation is linearised by only retaining the first-order terms of the Taylor expansion to obtain

$$\frac{\partial \tilde{h}}{\partial \tau} = \frac{\partial^2}{\partial x^2}\left[\left(1 - x_{\mathrm{i}} + \frac{(x-x_{\mathrm{i}})^2}{(1-dx)^{4/3}} H(x_{\mathrm{i}} - x)\right)^{3/2} \frac{\tilde{h}}{1-x}\right].$$

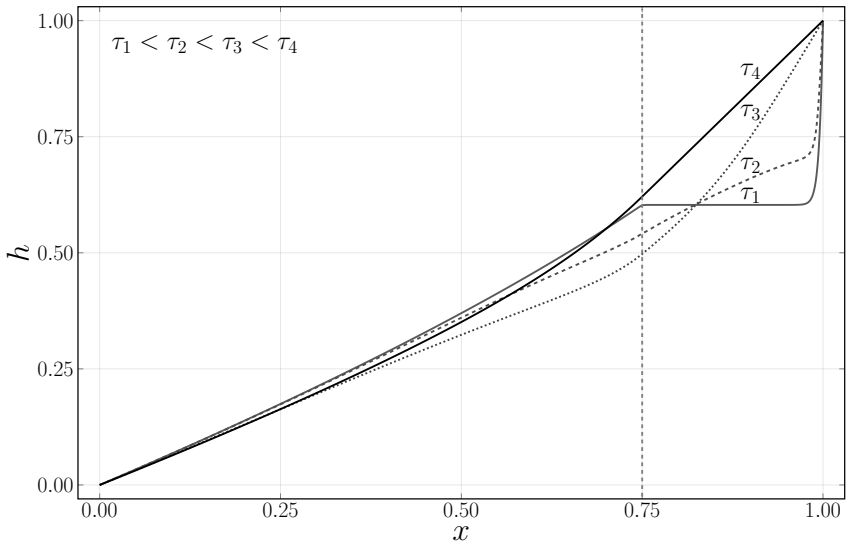

Figure 4.3: Evolution of Dean's profile (A.3.1) towards the equilibrium bottom profile (4.2.20) for diffusively dominated transport. The bottom profile is shown at $\tau_1 = 0$, $\tau_2 = 0.013$, $\tau_3 = 0.05$ and $\tau_4 = 0.2$. The vertical dotted grey line indicates the interface $x_\mathrm{i} = 0.75$ and the scaling parameter is $d = 1$. The numerical solution is computed with $n = 1000$ spatial nodes and time step $\Delta t = 10^{-3}$.

Separation of variables shows that this equation allows solutions of the form

$$\tilde{h}(x, \tau) = g(x)e^{\omega\tau}.$$

The corresponding eigenvalue problem is given by

$$\frac{\partial^2}{\partial x^2}\left[\left(1 - x_\mathrm{i} + \frac{(x - x_\mathrm{i})^2}{(1 - dx)^{4/3}} H(x_\mathrm{i} - x)\right)^{3/2} \frac{g}{1 - x}\right] = \omega g.$$

No closed form expression for the eigenvalues could be found. The eigenvalues of the discretized operator are therefore obtained numerically in the next section. The stability of the equilibrium bottom profile can also be determined using these eigenvalues.

4.2.5 Temporal evolution towards equilibrium

The temporal behaviour of the bottom can be investigated by numerically solving the response evolution equations (4.2.11) and (4.2.12) determined with method 1 or by numerically solving the total bottom evolution equation (4.2.19) from method 2. Here, the latter approach is taken as this case reduces to solving the diffusively dominated transport equation with additional source terms. Hence, the same numerical schemes can be used as in Section 3.3.3. Thus, a Finite Element Method is used for the spatial discretization, the θ-scheme for the temporal discretization and the nonlinear system is solved using the Newton-Raphson method, see Appendix B.1 for a derivation. The FEM discretization uses linear elements and $n = 1000$ spatial nodes. The temporal discretization uses $\theta = 1/2$ and time step $\Delta t = 10^{-3}$.

Dean's profile initially

The source term f_s is chosen such that when the entrance of the basin is closed, Dean's bottom profile is the equilibrium solution. Thus a logical choice of the initial bottom profile in the sea is Dean's profile. In the basin, the nearly flat bottom is prescribed such that it is continuous at the entrance of the basin. At the interface between the sea and the basin the bottom profile is smoothed such that the derivatives are also continuous, see Appendix A.3 for the derivation.

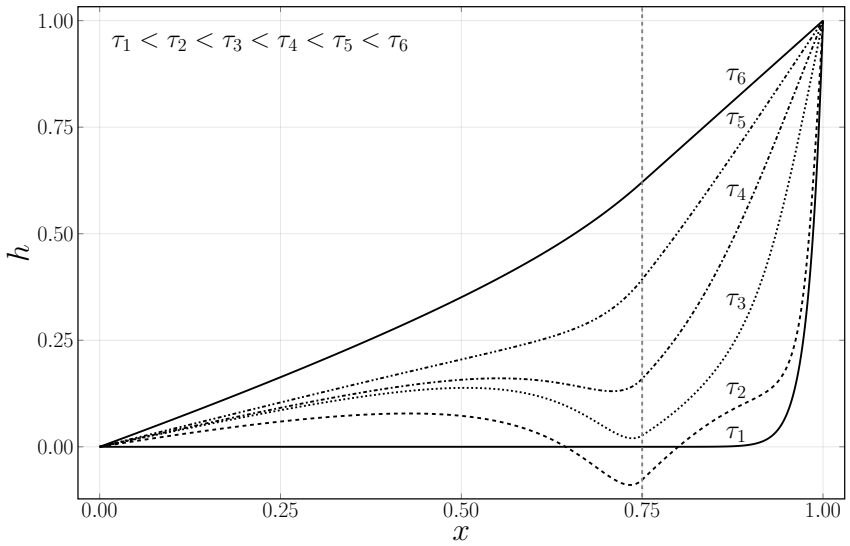

Figure 4.4: Evolution of an initially nearly flat bottom towards the equilibrium bottom profile given by equation (4.2.20) for diffusively dominated transport. The bottom profile is shown at $\tau_1 = 0$, $\tau_2 = 0.1$, $\tau_3 = 0.4$, $\tau_4 = 0.65$, $\tau_5 = 1$ and $\tau_6 = 10$. The vertical dotted grey line indicates the interface $x_\mathrm{i} = 0.75$ and the scaling parameter is $d = 1$. The numerical solution is computed with $n = 1000$ spatial nodes and time step $\Delta t = 10^{-3}$.

The seabed response to opening the basin is shown in Figure 4.3. At τ_1 the initial bottom profile can be seen, it consists of Dean's equilibrium bottom profile in the sea and the nearly flat bottom in the basin (see equation (A.3.1)). Most of the deposited sediment at the entrance of the basin is washed towards the landward boundary at τ_2. At τ_3 this process continues until the equilibrium bed profile (4.2.20) is reached at τ_4.

Furthermore, it can be seen that the equilibrium response to opening the basin is moderate in the sea domain and substantial inside the basin. In the basin the linear equilibrium bottom profile (3.3.7) is retrieved again, as was the case in the model with solely the basin (see Section 3.3.3). This could have been expected as the equations inside of the basin are unaltered (see equations (4.1.3a–d) for $x > x_\mathrm{i}$). Moreover, the sea basin interaction at the interface results in a new equilibrium entrance height. The equilibrium entrance height can be calculated using equation (4.2.17).

Nearly flat bottom initially

In Figure 4.4, the evolution of an excavated tidal inlet is shown. Initially, the bottom profile is given by $h = x^{50}$ at τ_1. At τ_2 and τ_3, sediment is transported away from the basin entrance leaving a deep cross-basin channel and sediment is deposited at the landward side. Time stamps τ_4 and τ_5 show how the bottom evolves towards the equilibrium bottom profile (4.2.20) given by τ_6, which is the same equilibrium bed profile obtained with Dean's profile initially.

To investigate if the eroded sediment from the basin entrance is the same sediment that is deposited at the landwards side, the evolution of the spatially varying total sediment transport is needed. The total sediment transport of the tidal inlet reads

$$\langle F_\mathrm{tot} \rangle = -\frac{\partial \langle C \rangle}{\partial x} - \int_{x_\mathrm{i}}^{x} f_\mathrm{s}(\tilde{x}) H(x_\mathrm{i} - \tilde{x})\, d\tilde{x}. \tag{4.2.21}$$

The total sediment transport can be derived from equation (4.1.3d). The temporal evolution of the total sediment transport of the nearly flat bottom initially is displayed in Figure 4.5. Positive sediment transport denotes that sediment is transported in the positive x direction or landwards. Since there is a positive local maximum at the basin entrance x_i initially, it follows that indeed the sediment from the entrance of the basin is transported towards the landward side. Furthermore, since the sediment transport is positive everywhere, it shows that all sediment deposited inside the tidal inlet originated

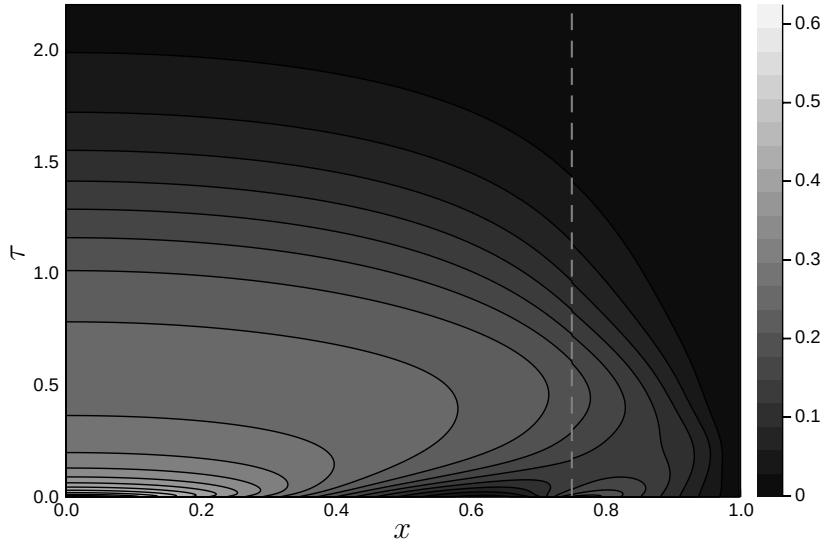

Figure 4.5: Contour plot of the evolution of the total sediment transport $\langle F_{\text{tot}} \rangle$ (4.2.21) for the nearly flat bottom initially. This is a so-called Hovmöller diagram for the total sediment transport $\langle F_{\text{tot}} \rangle$ with on the x-axis the along the basin coordinate and on the y-axis the morphological time τ. The vertical dotted grey line indicates the interface $x_{\text{i}} = 0.75$.

from the seaward boundary. Moreover, the total sediment transport vanishes first at the landwards side, showing that here the equilibrium profile is attained first, and the vanishing sediment transport slowly spreads to the rest of the basin, showing that the basin is filled from the landward side towards the seaward side as is observed in Figure 4.4.

Eigenvalues

In Figure 4.6, the ten largest eigenvalues of the discretized operator of the sea-basin system are shown. The eigenvalues are depicted as light grey circles. The discretized operator is linearised around the equilibrium profile (4.2.20). The roots of the Bessel function show the analytical eigenvalues of solely the basin system from Chapter 3. Since the largest eigenvalue of the sea-basin system is larger than the largest eigenvalue of the basin, it follows that the sea-basin system is less stable. Nevertheless, the sea-basin system is still asymptotically linear stable near the equilibrium profile as all the eigenvalues are negative.

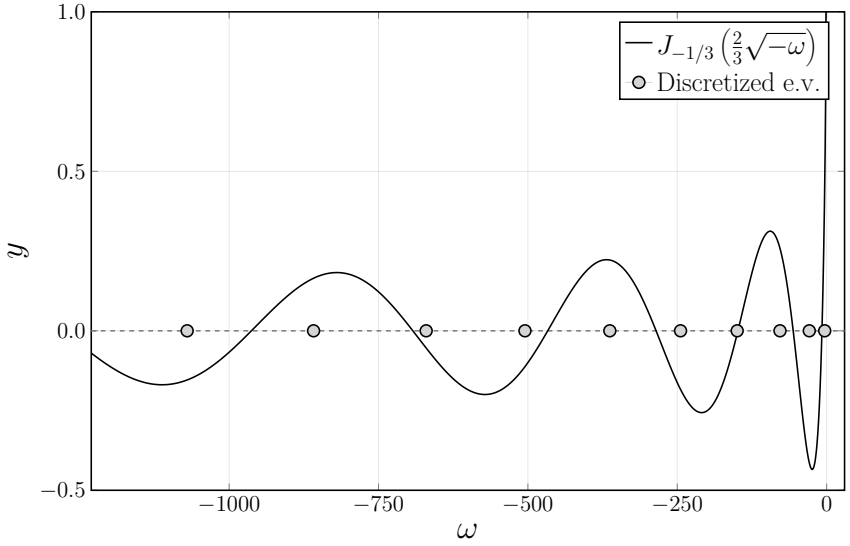

Figure 4.6: The ten largest eigenvalues of the discretized operator or matrix (B.1.7) when linearised around equilibrium profile (4.2.20). The eigenvalues are shown as light grey dots. The eigenvalues of the discrete operator are obtained after correcting for the factor Δx resulting from the FEM discretization and are computed with $n = 1000$ nodes. The eigenvalues of solely the basin are the roots of the Bessel function $J_{-1/3}\left(\frac{2}{3}\sqrt{-\omega}\right)$, see equation (3.3.12).

Chapter 5

The morphodynamics of a two-dimensional idealised sea-basin system

In this chapter, the morphodynamics of a two-dimensional semi-infinite sea and a one-dimensional basin are analysed. The geometry of the sea-basin system is introduced and the governing morphodynamic equation presented. These equations are solved by splitting the equations into two parts: a basic part and a response part. A Perfectly Matched Layer is used to incorporate the Sommerfeld radiation condition and the sea response system is analysed.

5.1 The two-dimensional idealised sea-basin system

The seawards boundary condition used in Chapter 3 assumes a fixed depth at the entrance of the embayment. This fixed depth is also present in the computed equilibrium profiles. To allow other equilibrium entrance heights to occur and to investigate the behaviour of the bottom profile at the entrance of the basin, the seaward boundary is replaced by a boundary at sea, far away from the entrance of the basin. In this section, the sea is modelled as a two-dimensional semi-infinite domain, contrary to the one-dimensional model used in Chapter 4. The modelling approach and solution procedure are fairly similar to Chapter 4.

The geometry of the sea-basin system is depicted in Figure 5.1. The coast runs along the line $x = 0$ and the rectangular basin is centred at $y = 0$ with width $2b$. Far away from the basin, a Kelvin wave is prescribed, which models the alongshore running tidal wave. The alongshore running Kelvin wave is derived in Section 5.2.1. The sea-basin interaction generates waves which radiate into the sea. These radiated waves are the subject of Section 5.2.2.

Analytically, these radiated waves should travel towards infinity. However, since a finite numerical domain is used, a boundary condition at the end of this computational domain has to be imposed. The general structure of these radiated waves can be quite complex and as a result, these waves do not satisfy simple boundary conditions. To this end, an approach similar to the Perfectly Matched Layer (PML) is used. A PML is an extra layer before the actual boundary where friction is introduced into the system. The friction inside this layer is chosen such that the waves enter the PML without reflecting and such that the waves are fully suppressed when they reach the actual boundary. As such, the actual prescribed boundary condition at the end of the PML does not influence the rest of the computational domain, as analytically desired. Thus a spatially dependent friction coefficient $\hat{r}(x, y)$ is introduced. To be consistent with Chapter 4, the friction inside the domain of interest is assumed to vanish. Hence, the friction coefficient is zero everywhere except near the seaward boundary where the friction is slowly 'turned on'

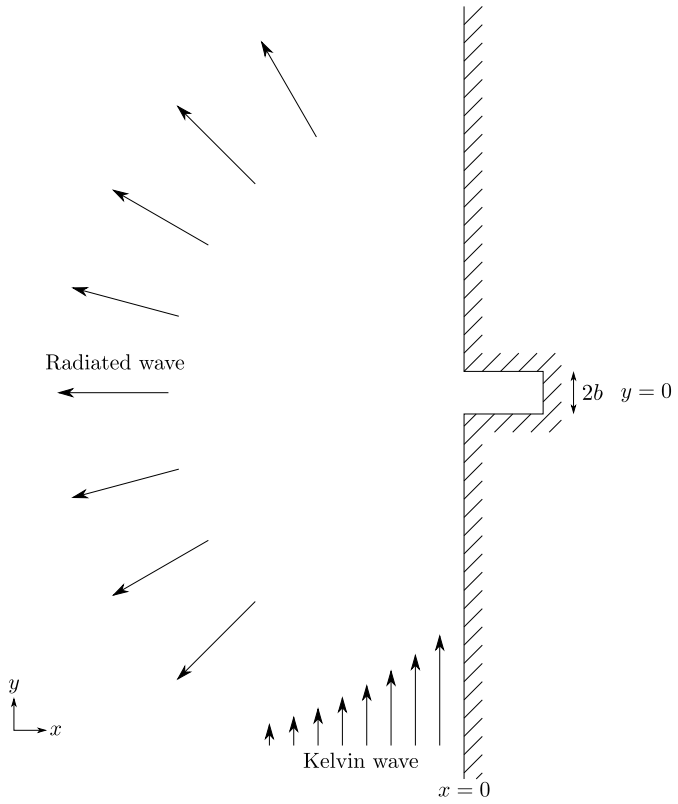

Figure 5.1: Top view of the geometry of the sea-basin system. The tidal wave forcing is depicted as the Kelvin wave and the waves generated due to the sea-basin interaction as the radiated wave.

to suppress the spurious reflections. Hence, the system without friction is solved in the domain of interest and friction is only introduced to comply with the analytic boundary conditions.

The two-dimensional hydro-morphodynamic equations are derived, nondimensionalized and scaled in e.g. Ter Brake (2011). The nondimensionalization process and scaling analysis are very similar to the one-dimensional case described in Chapter 3. The nondimensional parameters, introduced to nondimensionalize the hydro-morphodynamic equations, are given by

$$\begin{aligned} &\varepsilon = \frac{U}{\sigma L}, \qquad \hat{f} = \frac{f}{\sigma}, \qquad \Lambda = \frac{gH}{\sigma^2 L^2}, \qquad \hat{r} = \frac{r^*}{\sigma H}, \qquad a = \frac{\sigma \kappa_{\mathrm{v}}}{\omega_{\mathrm{s}}^2}, \\ &\kappa = \frac{\kappa_{\mathrm{h}}}{\sigma L^2}, \qquad \gamma = \frac{\omega_{\mathrm{s}} H}{\kappa_{\mathrm{v}}}, \qquad \delta_{\mathrm{s}} = \frac{\alpha U^2}{\rho_{\mathrm{s}}(1-p)\sigma H}, \qquad \delta_{\mathrm{b}} = \frac{\hat{s} U^b}{\sigma H L u_{\mathrm{c}}^b}, \qquad \mu = \frac{\mu_* H}{L}. \end{aligned} \tag{5.1.1}$$

The characteristic values of the North Sea and the corresponding nondimensional parameters are presented in Table 5.1. This table shows that nearly all processes are equally important in the sea domain. Nevertheless, it is assumed that the dominated transport phenomenon is diffusive transport.

The water motion and bottom evolution in the two-dimensional semi-infinite sea are described by the depth-averaged, nondimensionalized, diffusively dominated, simplified, two-dimensional hydro-morphodynamic

Table 5.1: Characteristic values of the North Sea. The dimensionless parameters are summarised in equation (5.1.1).

Sea	Sediment	Dimensionless
$L = 9 \cdot 10^5\,\mathrm{m}$	$\alpha = 0.005\,\mathrm{kg\,s\,m^{-4}}$	$\varepsilon \sim 1.7 \cdot 10^{-2}$
$H = 40\,\mathrm{m}$	$\omega_\mathrm{s} = 0.015\,\mathrm{m\,s^{-1}}$	$\hat{f} \sim 7.1 \cdot 10^{-1}$
	$\kappa_\mathrm{v} = 0.1\,\mathrm{m^2\,s^{-1}}$	$\Lambda \sim 2.5 \cdot 10^{-2}$
Tide	$\kappa_\mathrm{h} = 10^2\,\mathrm{m^2\,s^{-1}}$	$\hat{r} \sim 7.1 \cdot 10^{-2}$
$\sigma = 1.4 \cdot 10^{-4}\,\mathrm{rad\,s^{-1}}$	$\rho_\mathrm{s} = 2650\,\mathrm{kg\,m^{-3}}$	$a \sim 6.2 \cdot 10^{-2}$
$A = 0.84\,\mathrm{m}$	$d = 1.3 \cdot 10^{-4}\,\mathrm{m}$	$\kappa \sim 8.8 \cdot 10^{-7}$
$U = 2.12\,\mathrm{m\,s^{-1}}$	$p = 0.4$	$\gamma \sim 6$
	$\hat{s} = 3 \cdot 10^{-6}\,\mathrm{m\,s^{-1}}$	$\delta_\mathrm{s} \sim 2.5 \cdot 10^{-3}$
Constant	$u_\mathrm{c} = 0.3\,\mathrm{m\,s^{-1}}$	$\delta_\mathrm{b} \sim 2.1 \cdot 10^{-7}$
$f = 10^{-4}\,\mathrm{rad\,s^{-1}}$	$\mu_* = 2$	$\mu \sim 8.9 \cdot 10^{-5}$
$g = 9.81\,\mathrm{m\,s^{-2}}$	$b = 3$	
$r^* = 4 \cdot 10^{-4}\,\mathrm{m\,s^{-1}}$		

equations and read:

$$
\begin{cases}
\dfrac{\partial \zeta}{\partial t} + \dfrac{\partial}{\partial x}\big[(1-h)u\big] + \dfrac{\partial}{\partial y}\big[(1-h)v\big] = f_\mathrm{b}, & \text{(5.1.2a)}\\[2ex]
\dfrac{\partial u}{\partial t} - \hat{f}v = -\Lambda\dfrac{\partial \zeta}{\partial x} - \dfrac{\hat{r}u}{1-h}, & \text{(5.1.2b)}\\[2ex]
\dfrac{\partial v}{\partial t} + \hat{f}u = -\Lambda\dfrac{\partial \zeta}{\partial y} - \dfrac{\hat{r}v}{1-h}, & \text{(5.1.2c)}\\[2ex]
-a\kappa\left(\dfrac{\partial^2\langle C\rangle}{\partial x^2} + \dfrac{\partial^2\langle C\rangle}{\partial y^2}\right) = \big\langle u^2\big\rangle + \big\langle v^2\big\rangle - \langle C\rangle, & \text{(5.1.2d)}\\[2ex]
\dfrac{\partial h}{\partial \tau} = -\dfrac{\partial\big\langle F^1_\mathrm{diff}\big\rangle}{\partial x} - \dfrac{\partial\big\langle F^2_\mathrm{diff}\big\rangle}{\partial y} + f_\mathrm{s}, & \text{(5.1.2e)}
\end{cases}
$$

where the components of the diffusive flux are respectively given by

$$
\big\langle F^1_\mathrm{diff}\big\rangle = -\frac{\partial\langle C\rangle}{\partial x} \qquad \text{and} \qquad \big\langle F^2_\mathrm{diff}\big\rangle = -\frac{\partial\langle C\rangle}{\partial y}.
$$

Furthermore, $\tau = \delta_\mathrm{s} a\kappa t$ is the morphological time scale and $f_\mathrm{b}, f_\mathrm{s}$ are source terms added to the system to represent the inflow and outflow of the basin and to parametrise the unmodelled sea dynamics respectively. See Section 2.2 for a derivation of the depth-averaged two-dimensional shallow water equations. The purpose of the source terms $f_\mathrm{b}, f_\mathrm{s}$ is elaborated on below.

The basin is still modelled as a one-dimensional embayment. The one-dimensional basin domain needs to be coupled with the two-dimensional sea. For this, a source term f_b is used in the sea domain. The exact form of f_b is described in Section 5.2.2. The dynamics in the *basin* are still described by the one-dimensional hydro-morphodynamic equations (4.2.7a–d).

The complex dynamics in the sea are parametrised with the additional source term f_s. This source term captures the unmodelled physical processes like wave-induced sediment transport, wave breaking, alongshore currents, littoral drift etcetera. As a first step, the source term f_s is chosen such that the equilibrium bottom profile is flat when the basin entrance is closed off. This is the simplest case and allows a few equations to be solved analytically.

5.2 Solving the two-dimensional idealised sea-basin system

Similar to Chapter 4, the state vector (4.1.1) in the sea and basin are split into a basic part and a response part. The state vector in the sea consists of a basic state $\Psi^\mathrm{b}_\mathrm{s}$, which is the solution when the entrance to

the basin is blocked, and a response state $\Psi_{\mathrm{s}}^{\mathrm{r}}$, which is the response in the sea domain when the entrance to the basin is opened. Similarly, in the basin the basic state is $\Psi_{\mathrm{b}}^{\mathrm{b}}$, which is the solution when the entrance to the basin is closed, and the response state is $\Psi_{\mathrm{b}}^{\mathrm{r}}$, which is the response in the basin when the entrance is opened.

Since the equations and the forcing are homogeneous, it is assumed that the basic basin state vanishes $\Psi_{\mathrm{b}}^{\mathrm{b}} = \mathbf{0}$ for simplicity.

5.2.1 Solving the basic sea state equations

Substituting the total sea state $\Psi_{\mathrm{s}} = \Psi_{\mathrm{s}}^{\mathrm{b}} + \Psi_{\mathrm{s}}^{\mathrm{r}}$ into the hydro-morphodynamic equations (5.1.2a–e) and requiring that the basic sea state balances with itself only (as the response sea state $\Psi_{\mathrm{s}}^{\mathrm{r}}$ is not present when the basin is closed off) results in the basic sea state equations:

$$\begin{cases} \dfrac{\partial \zeta_{\mathrm{s}}^{\mathrm{b}}}{\partial t} + \dfrac{\partial}{\partial x}\Big[\big(1-h_{\mathrm{s}}^{\mathrm{b}}\big)u_{\mathrm{s}}^{\mathrm{b}}\Big] + \dfrac{\partial}{\partial y}\Big[\big(1-h_{\mathrm{s}}^{\mathrm{b}}\big)v_{\mathrm{s}}^{\mathrm{b}}\Big] = 0, & \text{(5.2.1a)} \\ \dfrac{\partial u_{\mathrm{s}}^{\mathrm{b}}}{\partial t} - \hat{f}v_{\mathrm{s}}^{\mathrm{b}} = -\Lambda\dfrac{\partial \zeta_{\mathrm{s}}^{\mathrm{b}}}{\partial x} - \dfrac{\hat{r}u_{\mathrm{s}}^{\mathrm{b}}}{1-h_{\mathrm{s}}^{\mathrm{b}}-h_{\mathrm{s}}^{\mathrm{r}}}, & \text{(5.2.1b)} \\ \dfrac{\partial v_{\mathrm{s}}^{\mathrm{b}}}{\partial t} + \hat{f}u_{\mathrm{s}}^{\mathrm{b}} = -\Lambda\dfrac{\partial \zeta_{\mathrm{s}}^{\mathrm{b}}}{\partial y} - \dfrac{\hat{r}v_{\mathrm{s}}^{\mathrm{b}}}{1-h_{\mathrm{s}}^{\mathrm{b}}-h_{\mathrm{s}}^{\mathrm{r}}}, & \text{(5.2.1c)} \\ -a\kappa\left(\dfrac{\partial^2\langle C_{\mathrm{s}}^{\mathrm{b}}\rangle}{\partial x^2} + \dfrac{\partial^2\langle C_{\mathrm{s}}^{\mathrm{b}}\rangle}{\partial y^2}\right) = \langle (u_{\mathrm{s}}^{\mathrm{b}})^2\rangle + \langle (v_{\mathrm{s}}^{\mathrm{b}})^2\rangle - \langle C_{\mathrm{s}}^{\mathrm{b}}\rangle, & \text{(5.2.1d)} \\ \dfrac{\partial h_{\mathrm{s}}^{\mathrm{b}}}{\partial \tau} = -\dfrac{\partial\langle F_{\mathrm{s,diff}}^{\mathrm{b},1}\rangle}{\partial x} - \dfrac{\partial\langle F_{\mathrm{s,diff}}^{\mathrm{b},2}\rangle}{\partial y} + f_{\mathrm{s}}, & \text{(5.2.1e)} \end{cases}$$

These equations are simplified by retaining the dominant terms only. Following Cushman-Roisin and Beckers (2009, p. 251), it is assumed that there is no cross-shore velocity, i.e. $u_{\mathrm{s}}^{\mathrm{b}} = 0$. Furthermore, the bottom friction terms are neglected and the basic sea bottom profile $h_{\mathrm{s}}^{\mathrm{b}}$ is flat and constant. The simplified basic sea state equations are obtained as:

$$\begin{cases} \dfrac{\partial \zeta_{\mathrm{s}}^{\mathrm{b}}}{\partial t} + \dfrac{\partial}{\partial y}\Big[\big(1-h_{\mathrm{s}}^{\mathrm{b}}\big)v_{\mathrm{s}}^{\mathrm{b}}\Big] = 0, & \text{(5.2.2a)} \\ \hat{f}v_{\mathrm{s}}^{\mathrm{b}} = \Lambda\dfrac{\partial \zeta_{\mathrm{s}}^{\mathrm{b}}}{\partial x}, & \text{(5.2.2b)} \\ \dfrac{\partial v_{\mathrm{s}}^{\mathrm{b}}}{\partial t} = -\Lambda\dfrac{\partial \zeta_{\mathrm{s}}^{\mathrm{b}}}{\partial y}, & \text{(5.2.2c)} \\ -a\kappa\left(\dfrac{\partial^2\langle C_{\mathrm{s}}^{\mathrm{b}}\rangle}{\partial x^2} + \dfrac{\partial^2\langle C_{\mathrm{s}}^{\mathrm{b}}\rangle}{\partial y^2}\right) = \langle (v_{\mathrm{s}}^{\mathrm{b}})^2\rangle - \langle C_{\mathrm{s}}^{\mathrm{b}}\rangle, & \text{(5.2.2d)} \\ 0 = -\dfrac{\partial\langle F_{\mathrm{s,diff}}^{\mathrm{b},1}\rangle}{\partial x} - \dfrac{\partial\langle F_{\mathrm{s,diff}}^{\mathrm{b},2}\rangle}{\partial y} + f_{\mathrm{s}}, & \text{(5.2.2e)} \end{cases}$$

Taking the temporal derivative of equation (5.2.2c), using equation (5.2.2a) and using that $h_{\mathrm{s}}^{\mathrm{b}}$ is constant results in the classical wave equation for $v_{\mathrm{s}}^{\mathrm{b}}$ parallel to the y-axis:

$$\frac{\partial^2 v_{\mathrm{s}}^{\mathrm{b}}}{\partial t^2} = \Lambda(1-h_{\mathrm{s}}^{\mathrm{b}})\frac{\partial^2 v_{\mathrm{s}}^{\mathrm{b}}}{\partial y^2}.$$

The wave speed is given by $c = \sqrt{\Lambda(1-h_{\mathrm{s}}^{\mathrm{b}})}$. The solution consists of two waves travelling in the positive and negative y direction respectively:

$$v_{\mathrm{s}}^{\mathrm{b}}(x,y,t) = V_1(x, y-ct) + V_2(x, y+ct).$$

From equation (5.2.2c) the solution of free surface $\eta_{\mathrm{s}}^{\mathrm{b}}$ can be obtained:

$$\zeta_{\mathrm{s}}^{\mathrm{b}}(x,y,t) = \sqrt{\frac{1-h_{\mathrm{s}}^{\mathrm{b}}}{\Lambda}}V_1(x, y-ct) - \sqrt{\frac{1-h_{\mathrm{s}}^{\mathrm{b}}}{\Lambda}}V_2(x, y+ct).$$

Application of equation (5.2.2b) and using that V_1 and V_2 balance with themselves only, as either one could vanish, results in Ordinary Differential Equations (ODEs) with constant coefficients:

$$\frac{\partial V_1}{\partial x} = \frac{\hat{f}}{c} V_1 \qquad \text{and} \qquad \frac{\partial V_2}{\partial x} = -\frac{\hat{f}}{c} V_2.$$

The solution of the ODEs are

$$V_1(x, y, t) = \widehat{V}_1(y - ct)e^{x/R} \qquad \text{and} \qquad V_2(x, y, t) = \widehat{V}_2(y + ct)e^{-x/R}$$

where $R \equiv \sqrt{\Lambda(1 - h_{\mathrm{s}}^{\mathrm{b}})}/\hat{f}$ is the Rossby radius of deformation. In the northern hemisphere $f > 0$. Hence, for the first wave the amplitude decreases exponentially with negative x and for the second wave, the amplitude increases exponentially with negative x. Thus the only physical solution is V_1. The general solution of the hydrodynamic equations (5.2.2a–c) is given by

$$\begin{aligned}
\zeta_{\mathrm{s}}^{\mathrm{b}} &= \sqrt{\frac{1 - h_{\mathrm{s}}^{\mathrm{b}}}{\Lambda}}\, \widehat{V}_1(y - ct)e^{x/R}, \\
u_{\mathrm{s}}^{\mathrm{b}} &= 0, \\
v_{\mathrm{s}}^{\mathrm{b}} &= \widehat{V}_1(y - ct)e^{x/R}.
\end{aligned}$$

These kinds of waves are known as Kelvin waves and only exist in the presence of a boundary. Kelvin waves decay exponentially in the cross-shore direction, i.e. away from the coast along the negative x-axis, and travel undistorted at the speed of gravity waves $c = \sqrt{\Lambda(1 - h_{\mathrm{s}}^{\mathrm{b}})}$ in the alongshore direction. A Kelvin wave is the first type of tidal wave in a region with boundaries. Thus, a Kelvin wave can be used to model the behaviour of the tide.

The hydrodynamics are forced by the nondimensionalized tide far away from the tidal inlet. The boundary condition reads

$$\zeta_{\mathrm{s}}^{\mathrm{b}} = \cos t\, e^{x/R} \quad \text{at} \quad y = -B.$$

To be consistent with the one-dimensional sea-basin system, it is required that $B = \lambda m$ for integer m, where $\lambda = 2\pi c$ is the tidal wavelength. This condition ensures that at $x = y = 0$, the free surface of the Kelvin wave is given by $\cos t$.

Application of the boundary condition results in the solution of the water motion in the undisturbed sea:

$$\zeta_{\mathrm{s}}^{\mathrm{b}} = \cos(y/c - t)e^{x/R}, \tag{5.2.3a}$$

$$u_{\mathrm{s}}^{\mathrm{b}} = 0, \tag{5.2.3b}$$

$$v_{\mathrm{s}}^{\mathrm{b}} = \sqrt{\frac{\Lambda}{1 - h_{\mathrm{s}}^{\mathrm{b}}}}\, \cos(y/c - t)e^{x/R}, \tag{5.2.3c}$$

similar to Buchwald (1971, p. 501), who also prescribed a harmonic Kelvin wave to model the tidal wave.

The leading order suspended sediment concentration can now be determined from the suspended sediment equation (5.2.2d) and yields

$$\langle C_{\mathrm{s}}^{\mathrm{b}} \rangle = \frac{\Lambda}{2(1 - h_{\mathrm{s}}^{\mathrm{b}})} e^{2x/R}.$$

The averaged suspended sediment concentration violates the vanishing diffusive transport boundary condition at the coast, i.e. at $x = 0$. However, it is more realistic that there is a nonzero sediment flux here, as the actual tidal wave also exchanges sediment with the coast.

According to the bottom evolution equation (5.2.2e), the source term has to be chosen as

$$f_{\mathrm{s}} = -\frac{2\Lambda}{(1 - h_{\mathrm{s}}^{\mathrm{b}})R^2} e^{2x/R}.$$

5.2.2 The response equations

The response sea state equations

Substituting the total sea state $\Psi_\mathrm{s} = \Psi_\mathrm{s}^\mathrm{b} + \Psi_\mathrm{s}^\mathrm{r}$ into the hydro-morphodynamic equations (5.1.2a–e) and subtracting the basic sea state equations (5.2.1a–e) results in the response sea state equations for $\Psi_\mathrm{s}^\mathrm{r}$:

$$\begin{cases} \dfrac{\partial \zeta_\mathrm{s}^\mathrm{r}}{\partial t} + \dfrac{\partial}{\partial x}\Big[\big(1-h_\mathrm{s}^\mathrm{b}-h_\mathrm{s}^\mathrm{r}\big)u_\mathrm{s}^\mathrm{r} - h_\mathrm{s}^\mathrm{r}u_\mathrm{s}^\mathrm{b}\Big] + \dfrac{\partial}{\partial y}\Big[\big(1-h_\mathrm{s}^\mathrm{b}-h_\mathrm{s}^\mathrm{r}\big)v_\mathrm{s}^\mathrm{r} - h_\mathrm{s}^\mathrm{r}v_\mathrm{s}^\mathrm{b}\Big] = f_\mathrm{b}, & \text{(5.2.4a)} \\ \dfrac{\partial u_\mathrm{s}^\mathrm{r}}{\partial t} = -\Lambda\dfrac{\partial \zeta_\mathrm{s}^\mathrm{r}}{\partial x} - \dfrac{\hat{r}u_\mathrm{s}^\mathrm{r}}{1-h_\mathrm{s}^\mathrm{b}-h_\mathrm{s}^\mathrm{r}}, & \text{(5.2.4b)} \\ \dfrac{\partial v_\mathrm{s}^\mathrm{r}}{\partial t} = -\Lambda\dfrac{\partial \zeta_\mathrm{s}^\mathrm{r}}{\partial y} - \dfrac{\hat{r}v_\mathrm{s}^\mathrm{r}}{1-h_\mathrm{s}^\mathrm{b}-h_\mathrm{s}^\mathrm{r}}, & \text{(5.2.4c)} \\ -a\kappa\left(\dfrac{\partial^2\langle C_\mathrm{s}^\mathrm{r}\rangle}{\partial x^2} + \dfrac{\partial^2\langle C_\mathrm{s}^\mathrm{r}\rangle}{\partial y^2}\right) = 2\langle u_\mathrm{s}^\mathrm{b}u_\mathrm{s}^\mathrm{r}\rangle + \langle (u_\mathrm{s}^\mathrm{r})^2\rangle + 2\langle v_\mathrm{s}^\mathrm{b}v_\mathrm{s}^\mathrm{r}\rangle + \langle (v_\mathrm{s}^\mathrm{r})^2\rangle - \langle C_\mathrm{s}^\mathrm{r}\rangle, & \text{(5.2.4d)} \\ \dfrac{\partial h_\mathrm{s}^\mathrm{r}}{\partial \tau} = -\dfrac{\partial\langle F_{\mathrm{s,diff}}^{\mathrm{r},1}\rangle}{\partial x} - \dfrac{\partial\langle F_{\mathrm{s,diff}}^{\mathrm{r},2}\rangle}{\partial y}, & \text{(5.2.4e)} \end{cases}$$

where the rotational effects due to the Coriolis force are neglected.

The solution of the basic sea state hydrodynamics (5.2.3a–c) is periodic with the tidal time scale and, hence, it is expected that the hydrodynamic responses of the basin and the sea are periodic. Thus the source term f_b modelling the interaction between the sea and the basin is periodic. Moreover, the narrow one-dimensional embayment is modelled as a point source forcing in the two-dimensional semi-infinite sea domain since the embayment width is very small compared to the length scales found in the sea. Hence, the source term is parametrised as

$$f_\mathrm{b} = \Re\Big\{Q\delta(\boldsymbol{x})e^{-i\omega t}\Big\},$$

where $\Re\{\,\cdot\,\}$ denotes taking the real part of a complex number, Q is the complex magnitude of the basin discharge, $\delta(\boldsymbol{x})$ the two-dimensional Dirac delta function and ω the tidal frequency.

The boundary conditions that the response sea state satisfies are

$$\begin{aligned} \sqrt{r}\left(\frac{\partial}{\partial r} + \frac{1}{c}\frac{\partial}{\partial t}\right)\zeta_\mathrm{s}^\mathrm{r} &= 0 && \text{for} \quad r\to\infty, && \text{(5.2.5a)} \\ u_\mathrm{s}^\mathrm{r} &= 0 && \text{at} \quad x = 0, && \text{(5.2.5b)} \\ \langle C_\mathrm{s}^\mathrm{r}\rangle &= 0 && \text{for} \quad r\to\infty, && \text{(5.2.5c)} \\ \frac{\partial}{\partial x}\langle C_\mathrm{s}^\mathrm{r}\rangle &= 0 && \text{at} \quad x = 0, && \text{(5.2.5d)} \\ h_\mathrm{s}^\mathrm{r} &= 0 && \text{for} \quad r\to\infty, && \text{(5.2.5e)} \\ \langle F_{\mathrm{s,diff}}^{\mathrm{r},1}\rangle &= 0 && \text{at} \quad x = 0. && \text{(5.2.5f)} \end{aligned}$$

The response basin state equations

The total basin state is equal to the response basin state $\Psi_\mathrm{b}^\mathrm{r}$ since the basic basin state is assumed to vanish. Hence, the response basin state $\Psi_\mathrm{b}^\mathrm{r}$ satisfies the hydro-morphodynamic equations (4.1.3a–d):

$$\begin{cases} \dfrac{\partial \zeta_\mathrm{b}^\mathrm{r}}{\partial t} + \dfrac{\partial}{\partial \hat{x}}\Big[\big(1-h_\mathrm{b}^\mathrm{r}\big)u_\mathrm{b}^\mathrm{r}\Big] = 0, & \text{(5.2.6a)} \\ \dfrac{\partial \zeta_\mathrm{b}^\mathrm{r}}{\partial \hat{x}} = 0, & \text{(5.2.6b)} \\ -a\kappa\dfrac{\partial^2\langle C_\mathrm{b}^\mathrm{r}\rangle}{\partial \hat{x}^2} = \langle (u_\mathrm{b}^\mathrm{r})^2\rangle - \langle C_\mathrm{b}^\mathrm{r}\rangle, & \text{(5.2.6c)} \\ \dfrac{\partial h_\mathrm{b}^\mathrm{r}}{\partial \tau} = -\dfrac{\partial\langle F_{\mathrm{b,diff}}^{\mathrm{r}}\rangle}{\partial \hat{x}}, & \text{(5.2.6d)} \end{cases}$$

where $\hat{x}$ is the nondimensional along-basin variable, i.e. $\hat{x} = 0$ is at the basin entrance and $\hat{x} = 1$ is the landward boundary of the basin.

The boundary conditions at the landwards side are

$$(1 - h_{\mathrm{b}}^{\mathrm{r}})u_{\mathrm{b}}^{\mathrm{r}} = 0 \qquad \text{at} \quad \hat{x} = 1, \tag{5.2.7a}$$

$$\frac{\partial \langle C_{\mathrm{b}}^{\mathrm{r}} \rangle}{\partial \hat{x}} = 0 \qquad \text{at} \quad \hat{x} = 1, \tag{5.2.7b}$$

$$\langle F_{\mathrm{b,diff}}^{\mathrm{r}} \rangle = 0 \qquad \text{at} \quad \hat{x} = 1. \tag{5.2.7c}$$

The matching conditions

The basin state and the sea state have to be matched at the basin entrance. Hence, matching conditions are needed. The following matching conditions are proposed.

The seabed is continuous at the interface, thus

$$h_{\mathrm{s}} = h_{\mathrm{b}} \quad \text{at} \quad x = 0 \quad \text{and} \quad -b < y < b.$$

The total flux through a semicylinder centred at the origin should equal the total flux through the rectangular basin entrance:

$$\int_{\pi/2}^{3\pi/2} (1 - h_{\mathrm{s}})(\boldsymbol{u}_{\mathrm{s}} \cdot \boldsymbol{n}) r \, d\varphi = 2b(1 - h_{\mathrm{b}})u_{\mathrm{b}} \quad \text{at} \quad \text{at} \quad x = 0 \quad \text{and} \quad -b < y < b.$$

where $\boldsymbol{n}$ is the cylinder unit normal vector, $2b$ is the nondimensionalized width of the basin and r is the radial and φ the angular coordinate of a polar coordinate system. The seabed should be continuous at the interface, thus $h_{\mathrm{s}} = h_{\mathrm{b}}$. The basin entrance is very small with respect to the sea domain, which led to the point source parametrisation of the source function f_{b}. Taking the limit $r \to 0$ yields the condition

$$\lim_{r \to 0} r(\boldsymbol{u}_{\mathrm{s}} \cdot \boldsymbol{n}) = \frac{2b}{\pi} u_{\mathrm{b}} \quad \text{at} \quad x = 0 \quad \text{and} \quad -b < y < b. \tag{5.2.8}$$

The third matching condition states that the basin-width-averaged surface heights are equal. This leads to the condition

$$\zeta_{\mathrm{b}} = \frac{1}{2b} \int_{-b}^{b} \zeta_{\mathrm{s}} \, dy \quad \text{at} \quad x = 0 \quad \text{and} \quad -b < y < b. \tag{5.2.9}$$

The last matching condition states that the diffusive flux is continuous across the interface:

$$\frac{\partial}{\partial x} \langle C_{\mathrm{s}} \rangle = \frac{\partial}{\partial x} \langle C_{\mathrm{b}} \rangle \quad \text{at} \quad x = 0 \quad \text{and} \quad -b < y < b.$$

5.2.3 The Helmholtz equation

In this section, it is shown that the hydrodynamic sea response equations (5.2.4a–c) can be rewritten as a single Helmholtz-type equation assuming a periodic time dependency.

It is assumed that the bottom profiles $h_{\mathrm{s}}^{\mathrm{b}}$ and h_{s}^{r} are known and constant on the fast tidal time scale. The hydrodynamic response equations (5.2.4a–c) allow harmonic solutions of the form:

$$\zeta_{\mathrm{s}}^{\mathrm{r}}(x, y, t) = \Re\Big\{ \eta_{\mathrm{s}}^{\mathrm{r}}(x, y) e^{-i\omega t} \Big\}, \qquad u_{\mathrm{s}}^{\mathrm{r}}(x, y, t) = \Re\Big\{ U_{\mathrm{s}}^{\mathrm{r}}(x, y) e^{-i\omega t} \Big\}, \qquad v_{\mathrm{s}}^{\mathrm{r}}(x, y, t) = \Re\Big\{ V_{\mathrm{s}}^{\mathrm{r}}(x, y) e^{-i\omega t} \Big\}.$$

Hence, $\eta_{\mathrm{s}}^{\mathrm{r}}$ is the complex spatial dependency of $\zeta_{\mathrm{s}}^{\mathrm{r}}$ and $U_{\mathrm{s}}^{\mathrm{r}}, V_{\mathrm{s}}^{\mathrm{r}}$ are the complex spatial dependencies of $u_{\mathrm{s}}^{r}, v_{\mathrm{s}}^{\mathrm{r}}$ respectively.

Substitution of the periodic time dependencies into the momentum equations (5.2.4b–c) yields two explicit relations between the flow velocities and the free surface:

$$U_{\mathrm{s}}^{\mathrm{r}} = \frac{\Lambda}{i\omega\big(1+i\frac{\hat{r}}{\omega(1-h_{\mathrm{s}}^{\mathrm{b}}-h_{\mathrm{s}}^{\mathrm{r}})}\big)}\frac{\partial \eta_{\mathrm{s}}^{\mathrm{r}}}{\partial x} \qquad \text{and} \qquad V_{\mathrm{s}}^{\mathrm{r}} = \frac{\Lambda}{i\omega\big(1+i\frac{\hat{r}}{\omega(1-h_{\mathrm{s}}^{\mathrm{b}}-h_{\mathrm{s}}^{\mathrm{r}})}\big)}\frac{\partial \eta_{\mathrm{s}}^{\mathrm{r}}}{\partial y}. \tag{5.2.10}$$

Substitution of the explicit relations in the conservation of mass equation (5.2.4a) results in a Helmholtz equation:

$$\frac{\partial}{\partial x}\left[\frac{\Lambda(1-h_{\mathrm{s}}^{\mathrm{b}}-h_{\mathrm{s}}^{\mathrm{r}})}{1+i\frac{\hat{r}}{\omega(1-h_{\mathrm{s}}^{\mathrm{b}}-h_{\mathrm{s}}^{\mathrm{r}})}}\frac{\partial \eta_{\mathrm{s}}^{\mathrm{r}}}{\partial x}\right] + \frac{\partial}{\partial y}\left[\frac{\Lambda(1-h_{\mathrm{s}}^{\mathrm{b}}-h_{\mathrm{s}}^{\mathrm{r}})}{1+i\frac{\hat{r}}{\omega(1-h_{\mathrm{s}}^{\mathrm{b}}-h_{\mathrm{s}}^{\mathrm{r}})}}\frac{\partial \eta_{\mathrm{s}}^{\mathrm{r}}}{\partial y}\right] + \omega^2\eta_{\mathrm{s}}^{\mathrm{r}} = i\omega\frac{\partial}{\partial y}\big[h_{\mathrm{s}}^{\mathrm{r}}V_{\mathrm{s}}^{\mathrm{b}}\big] + i\omega Q\delta(\boldsymbol{x}), \tag{5.2.11}$$

where it has been used that the cross-shore velocity vanishes, i.e. $u_{\mathrm{s}}^{\mathrm{b}} = 0$ see equation (5.2.3b), and the alongshore basic sea velocity has been written in complex form according to

$$v_{\mathrm{s}}^{\mathrm{b}}(x,y,t) = \Re\Big\{V_{\mathrm{s}}^{\mathrm{b}}(x,y)e^{-i\omega t}\Big\}.$$

Thus using equation (5.2.3c), it follows that the complex alongshore velocity is given by

$$V_{\mathrm{s}}^{\mathrm{b}} = \sqrt{\frac{\Lambda}{1-h_{\mathrm{s}}^{\mathrm{b}}}}e^{x/R+iy/c}. \tag{5.2.12}$$

The Helmholtz equation (5.2.11) can generally not be solved analytically and solving it numerically is difficult due to the finite numerical domain, where numerical boundary conditions have to be imposed at the seaward boundary. In the next section, an analytic solution is derived in case the parameters are constant. Using this analytical solution the numerical seaward boundary condition can be tested.

5.2.4 Analytical solution and Perfectly Matched Layer

In this section, a Helmholtz equation is derived that is analytically solvable, contrary to the Helmholtz equation (5.2.11) which is generally not analytically solvable. This analytically solvable Helmholtz equation is actually a special case of Helmholtz equation (5.2.11) for constant parameter values and no basic sea state or when the sea response bed vanishes. Using this analytical solution, the Perfectly Matched Layer method is tested.

Analytical radiation damping

Similar to Section 5.2.2, the water motion in a two-dimensional semi-infinite sea is solved with periodic point source forcing. However contrary to that section, the parameters are assumed to be constant and there is no Kelvin wave running alongshore. Hence, there is no basic state inside the sea. Since the forcing is circularly symmetric, the parameter values are constant and there is no symmetry-breaking basic sea state, it follows that the water motion is circularly symmetric. Hence, the water motion in the semi-infinite sea forced by a periodic point source is governed by the circularly symmetric, nondimensional, viscous, diffusively dominated, shallow water equations in polar coordinates:

$$\begin{cases} \dfrac{\partial \zeta_{\mathrm{s}}}{\partial t} + \dfrac{1}{r}\dfrac{\partial}{\partial r}\big[r(1-h_{\mathrm{s}})u_{\mathrm{s}}\big] = \dfrac{1-h_{\mathrm{s}}}{\pi r}\delta(r)\cos\omega t, & \text{(5.2.13a)} \\ \dfrac{\partial u_{\mathrm{s}}}{\partial t} = -\Lambda\dfrac{\partial \zeta_{\mathrm{s}}}{\partial r} - \dfrac{\hat{r}u_{\mathrm{s}}}{1-h_{\mathrm{s}}}, & \text{(5.2.13b)} \end{cases}$$

see equations (A.4.5a–b) respectively. Here, u_{s} is the radial velocity component, h_{s} is the bottom height and r is the radial coordinate. The source term is scaled such that the depth-averaged flux through the semicircle centred at the origin in the limit of $r \to 0$ is normalized:

$$\lim_{r\to 0}\int_{\pi/2}^{3\pi/2}(\boldsymbol{u}_{\mathrm{s}}\cdot\boldsymbol{n})r\,d\varphi = 1, \tag{5.2.14}$$

where $\boldsymbol{n}$ is the unit vector that points radially outwards at the surface of the semicircle.

The parameters are assumed to be constant, hence the seabed h_s is constant in time and space. Taking the temporal derivative of equation (5.2.13a) and using equation (5.2.13b) shows that the system of equations can be reduced to the circularly symmetric, damped wave equation in polar coordinates with periodic point source forcing:

$$\frac{\partial^2\zeta_\mathrm{s}}{\partial t^2} = \Lambda\big(1-h_\mathrm{s}\big)\frac{1}{r}\frac{\partial}{\partial r}\left(r\frac{\partial\zeta_\mathrm{s}}{\partial r}\right) - \frac{\hat{r}}{1-h_\mathrm{s}}\frac{\partial\zeta_\mathrm{s}}{\partial t} + \frac{\omega(1-h_\mathrm{s})}{\pi r}\delta(r)\left(-\sin\omega t + \frac{\hat{r}}{\omega(1-h_\mathrm{s})}\cos\omega t\right). \quad (5.2.15)$$

This equation allows periodic solutions of the form:

$$\zeta_\mathrm{s}(r,t) = \Re\Big\{\eta(r)e^{-i\omega t}\Big\} \qquad \text{and} \qquad u_\mathrm{s}(r,t) = \Re\Big\{U(r)e^{-i\omega t}\Big\}, \quad (5.2.16)$$

Substitution into the damped polar wave equation (5.2.15) yields the polar Helmholtz equation:

$$\frac{1}{r}\frac{\partial}{\partial r}\left(r\frac{\partial\eta}{\partial r}\right) + k^2\eta = \frac{i\omega}{\pi\Lambda}\left(1+i\frac{\hat{r}}{\omega(1-h_\mathrm{s})}\right)\frac{\delta(r)}{r}, \quad (5.2.17)$$

where the wave number

$$k^2 = \frac{\omega^2}{c^2}\left(1+i\frac{\hat{r}}{\omega(1-h_\mathrm{s})}\right),$$

and the wave speed $c=\sqrt{\Lambda(1-h_\mathrm{s})}$ have been defined. The Helmholtz equation (5.2.11) of Section 5.2.2 reduces to the polar Helmholtz equation, if we assume that all the parameters are constant and there is no basic sea state, i.e. set all the basic sea state variables to zero, or in the special case where the response seabed is zero: $h_\mathrm{s}^\mathrm{r}=0$. Then the equation is converted to polar coordinates, the solution is assumed to be circularly symmetric and the resulting equation multiplied with

$$\frac{1+i\frac{\hat{r}}{\omega(1-h_\mathrm{s}^\mathrm{b}-h_\mathrm{s}^\mathrm{r})}}{\Lambda(1-h_\mathrm{s}^\mathrm{b}-h_\mathrm{s}^\mathrm{r})}.$$

Expanding the derivatives, multiplying with r^2 and using the substitution $\xi=kr$ yields Bessel's differential equation for $\xi>0$:

$$\xi^2\frac{\partial^2\eta}{\partial\xi^2} + \xi\frac{\partial\eta}{\partial\xi} + \xi^2\eta = 0.$$

The order of the Bessel functions is $\nu=0$. Two linearly independent solutions of Bessel's differential equation are the Bessel function of the first kind $J_0(\xi)$ and the Bessel function of the second kind $Y_0(\xi)$. However, a more convenient basis is the linear combination of the Hankel function of the first kind $H_0^{(1)}(\xi)$ and the Hankel function of the second kind $H_0^{(2)}(\xi)$. Transforming back to the solution in terms of r yields

$$\eta(r) = AH_0^{(1)}(kr) + BH_0^{(2)}(kr).$$

The waves are generated at the origin and should scatter outwards, away from the origin. Hence, the energy radiated from the origin should scatter towards infinity and there should be no waves coming from infinity towards the origin. To this end, the Sommerfeld radiation condition is used which reads

$$\lim_{r\to\infty}\sqrt{r}\left(\frac{\partial}{\partial r} - ik\right)\eta = 0, \quad (5.2.18)$$

due to the choice of the time dependency, i.e. $e^{-i\omega t}$, in equation (5.2.16). Application of the Sommerfeld radiation condition and the asymptotic expansions of the Hankel functions for large arguments shows that $B=0$.

Integrating the polar Helmholtz equation (5.2.17) over a small semicircle or substituting equation (5.2.16) into equation (5.2.13b) and using the normalized flux condition (5.2.14), shows that the second boundary condition is given by

$$\lim_{r\to0} r\frac{\partial\eta}{\partial r} = \frac{i\omega}{\pi\Lambda}\left(1+i\frac{\hat{r}}{\omega(1-h_\mathrm{s})}\right).$$

Application of the second boundary condition yields the solution of the polar Helmholtz equation:

$$\eta(r) = \frac{\omega}{2\Lambda}\left(1 + i\frac{\hat{r}}{\omega(1-h_\mathrm{s})}\right)H_0^{(1)}(kr). \tag{5.2.19}$$

Using equation (5.2.13b) the corresponding complex flow field is found:

$$U(r) = \frac{ik}{2}H_1^{(1)}(kr). \tag{5.2.20}$$

In case there is no friction present in the system, i.e. $\hat{r} = 0$, the complex free surface reduces to

$$\eta(r) = \frac{\omega}{2\Lambda}H_0^{(1)}(kr),$$

which is in compliance with literature, see for example Buchwald (1971, p. 504) or Mei *et al.* (2005, p. 213). Furthermore, if there is no friction then it follows that k is real and using relation (5.2.16) shows that the free surface is given by

$$\zeta_\mathrm{s}(r,t) = \frac{\omega}{2\Lambda}\big(J_0(kr)\cos\omega t + Y_0(kr)\sin\omega t\big).$$

and the radial velocity by

$$u_\mathrm{s}(r,t) = \frac{k}{2}\big(-Y_1(kr)\cos\omega t + J_1(kr)\sin\omega t\big).$$

Perfectly Matched Layer

The analytical free surface solution (5.2.19) of the polar Helmholtz equation (5.2.17) satisfying the Sommerfeld radiation condition (5.2.18) does not satisfy simple boundary conditions on a finite domain. Thus an approach similar to a Perfectly Matched Layer is adopted. Before the actual boundary, a layer is introduced where the friction increases. This friction dampens out incoming waves and allows simple boundary conditions to be prescribed at the end of the finite domain, as these boundary conditions do not influence the domain due to the friction layer.

The exact form of the friction coefficient in the PML is problem specific and has to be determined on a per case basis. Several friction coefficient formulations have been tested. The best results for our problem are found with a friction coefficient of the from:

$$\hat{r}(r) = \alpha_\mathrm{r}\left(\frac{r - r_\mathrm{p}}{r_\mathrm{b} - r_\mathrm{p}}\right)^2 H(r - r_\mathrm{p}), \tag{5.2.21}$$

where α_r is a friction strength parameter, r_p is the start of the Perfectly Matched Layer domain and r_b is the actual boundary.

The general Helmholtz equation (5.2.11) is discretized in Appendix B.2 using linear triangular elements. If we assume that the parameters are constant and there is no basic sea state, or if we assume that the response seabed vanishes, then this equation is equivalent to polar Helmholtz equation (5.2.17) for which the analytical solution is known. Hence the PML method can be validated.

The analytical solution (5.2.19) and numerical solution of Helmholtz equation (5.2.17) are shown in Figure 5.2. The analytical solution is obtained for $\hat{r} = 0$ and the numerical solution uses the friction coefficient formulation given by equation (5.2.21). The numerical solution is obtained for a semicircular domain, however, since the solution is circularly symmetric, it follows that the solution along one line is sufficient. Here, the line $x = 0$ is chosen. In Figure 5.2, it can be seen that in the internal domain, the analytic and numeric solution are almost indistinguishable. In the PML, the numeric solution quickly decays to zero. Hence, the PML is a convenient way to numerically satisfy the Sommerfeld radiation condition.

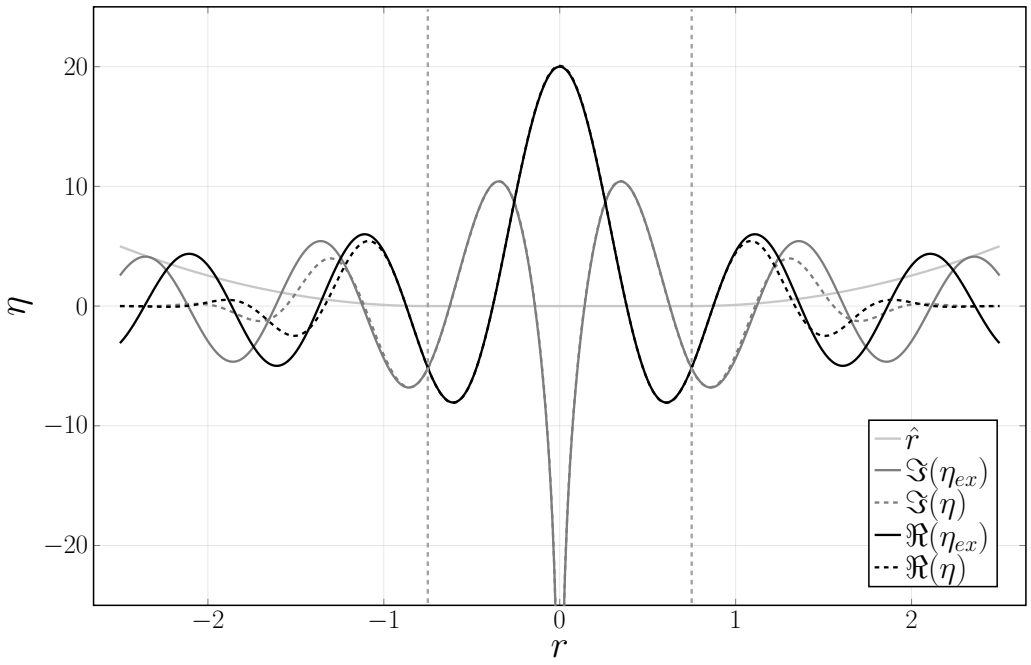

Figure 5.2: Analytic η_{ex} (continuous) and numeric η (dashed) surface height in the sea. The friction coefficient $\hat{r}$, given by equation (5.2.21), is also shown. The vertical grey dashed lines indicate the boundary between the interior domain and the PML and $\Im\{\cdot\}$ denotes taking the imaginary part of a complex number. The parameter values used are $\omega = 1$, $\Lambda = 2.5 \cdot 10^{-2}$, $\alpha_{\mathrm{r}} = 5$, $r_{\mathrm{p}} = 0.75$, $r_{\mathrm{b}} = 2.5$ and $n = 130617$.

5.2.5 Solving the sea response system

In this section, the sea response equations (5.2.4a–e) are solved. As a first step, only the influence of the basin is taken into account and the morphodynamic evolution of the basin is neglected. The sea response equations are solved using the so-called morphodynamic loop methodology. The morphodynamic loop is depicted in Figure 1.1. First, the water motion is resolved. Then the sediment transport is computed using the known water motion. The seabed is updated for the given sediment transport. The new seabed changes the water motion again and hence we have a loop.

If the basin is closed off, the seabed is flat and given by $h_{\mathrm{s}}^{\mathrm{b}}$. The idea is to determine what happens once the basin entrance opens. Hence, initially the response sea bed profile vanishes: $h_{\mathrm{s}}^{\mathrm{r}} = 0$. This implies that the term $i\omega\frac{\partial}{\partial y}\left[h_{\mathrm{s}}^{\mathrm{r}}V_{\mathrm{s}}^{\mathrm{b}}\right]$ vanishes in the Helmholtz equation (5.2.11). The Helmholtz equation is then circularly symmetric and the circularly symmetric, analytical free surface solution is given by equation (5.2.19). The analytical and numerical solutions are plotted in Figure 5.2. It should be noted that the analytical solution is valid up to a multiplicative factor, due to the assumed normalized basin flux. In Appendix A.5, the solution using the matching conditions is presented. In general, when $h_{\mathrm{s}}^{\mathrm{r}} \neq 0$, then the free surface solution has to be determined numerically, as is done in Appendix B.2.

Once the free surface $\eta_{\mathrm{s}}^{\mathrm{r}}$ is known, then the complex horizontal flow velocities can be determined using equation (5.2.10). Since the response seabed is still zero, the analytical solution of the free surface can be used to compute the analytical solution of the flow velocities and these are given by equation (5.2.20). The circularly symmetric, analytical and numerical solutions are shown in Figure 5.3. For nonzero response seabed, the flow fields need to be determined numerically, see Appendix B.2.3.

From equation (5.2.22), it follows that the leading order suspended sediment concentration is given by

$$\begin{aligned}\left\langle C_{\mathrm{s}}^{\mathrm{r}}\right\rangle &= \left\langle (u_{\mathrm{s}}^{\mathrm{r}})^2\right\rangle + 2\left\langle v_{\mathrm{s}}^{\mathrm{b}}v_{\mathrm{s}}^{\mathrm{r}}\right\rangle + \left\langle (v_{\mathrm{s}}^{\mathrm{r}})^2\right\rangle \\ &= \frac{1}{2}\left(U_{\mathrm{s}}^{\mathrm{r}}\bar{U}_{\mathrm{s}}^{\mathrm{r}}\right) + \frac{1}{2}\left(V_{\mathrm{s}}^{\mathrm{b}}\bar{V}_{\mathrm{s}}^{\mathrm{r}} + \bar{V}_{\mathrm{s}}^{\mathrm{b}}V_{\mathrm{s}}^{\mathrm{r}}\right) + \frac{1}{2}\left(V_{\mathrm{s}}^{\mathrm{r}}\bar{V}_{\mathrm{s}}^{\mathrm{r}}\right),\end{aligned} \tag{5.2.22}$$

where the bar denotes the complex conjugated quantity and the vanishing cross-shore velocity has been used. Thus $\left\langle C_{\mathrm{s}}^{\mathrm{r}}\right\rangle$ can be computed directly once $U_{\mathrm{s}}^{\mathrm{r}}$ and $V_{\mathrm{s}}^{\mathrm{r}}$ are known. For $h_{\mathrm{s}}^{\mathrm{r}} = 0$, the suspended

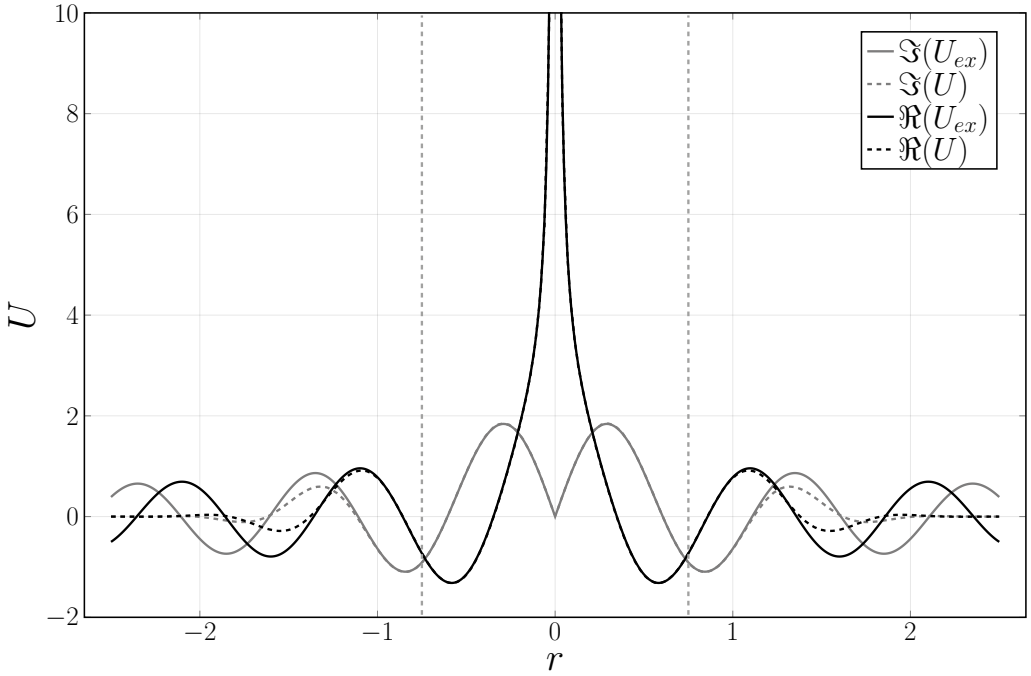

Figure 5.3: Analytic U_{ex} (continuous) and numeric U (dashed) radial velocity components in the sea. The vertical grey dashed lines indicate the boundary between the interior domain and the PML. The friction coefficient is given by equation (5.2.21). The parameter values used are $\omega = 1$, $\Lambda = 2.5 \cdot 10^{-2}$, $\alpha_{\mathrm{r}} = 5$, $r_{\mathrm{p}} = 0.75$, $r_{\mathrm{b}} = 2.5$ and $n = 130617$.

sediment concentration can be found analytically by substituting equations (5.2.20) and (5.2.12) into equation (5.2.22) and this yields

$$\langle C_{\mathrm{s}}^{\mathrm{r}} \rangle = \frac{1}{8}|k|^2 \big|H_1^{(1)}(kr)\big|^2 + \frac{1}{2}\sqrt{\frac{\Lambda}{1-h_{\mathrm{s}}^{\mathrm{b}}}}e^{x/R}\sin\varphi\,\Re\Big\{ike^{-iy/c}H_1^{(1)}(kr)\Big\},$$

and if there is no friction present in the system, i.e. $\hat{r} = 0$, then this result reduces to

$$\langle C_{\mathrm{s}}^{\mathrm{r}} \rangle = \frac{1}{8}k^2\big(J_1^2(kr) + Y_1^2(kr)\big) + \frac{1}{2}\sqrt{\frac{\Lambda}{1-h_{\mathrm{s}}^{\mathrm{b}}}}e^{x/R}\sin\varphi\big(-\cos(y/c)Y_1(kr) + \sin(y/c)J_1(kr)\big). \tag{5.2.23}$$

The analytical sediment concentration (5.2.23) and the numerical sediment concentration determined using the PML are shown in Figure 5.4. It can be seen that the response sediment concentration oscillates for negative y. The oscillations are due to the basic sea state interaction, as can be seen from the second term in equation (5.2.23).

The evolution of the response bottom is found using equation (5.2.4e) and is given in coordinate invariant form by

$$\frac{\partial h_{\mathrm{s}}^{\mathrm{r}}}{\partial \tau} = \nabla^2 \langle C_{\mathrm{s}}^{\mathrm{r}} \rangle.$$

For the vanishing response seabed and friction coefficient, the analytical leading order change of the bottom near the tidal inlet is given by

$$\frac{\partial h_{\mathrm{s}}^{\mathrm{r}}}{\partial \tau} = \frac{1}{r}\frac{\partial}{\partial r}\left(r\frac{\partial \langle C_{\mathrm{s}}^{\mathrm{r}} \rangle}{\partial r}\right) = \frac{2}{\pi^2 r^4} + \mathcal{O}\big(\ln^2 r\big). \tag{5.2.24}$$

Thus, the bottom evolves very rapidly near the entrance of the basin.

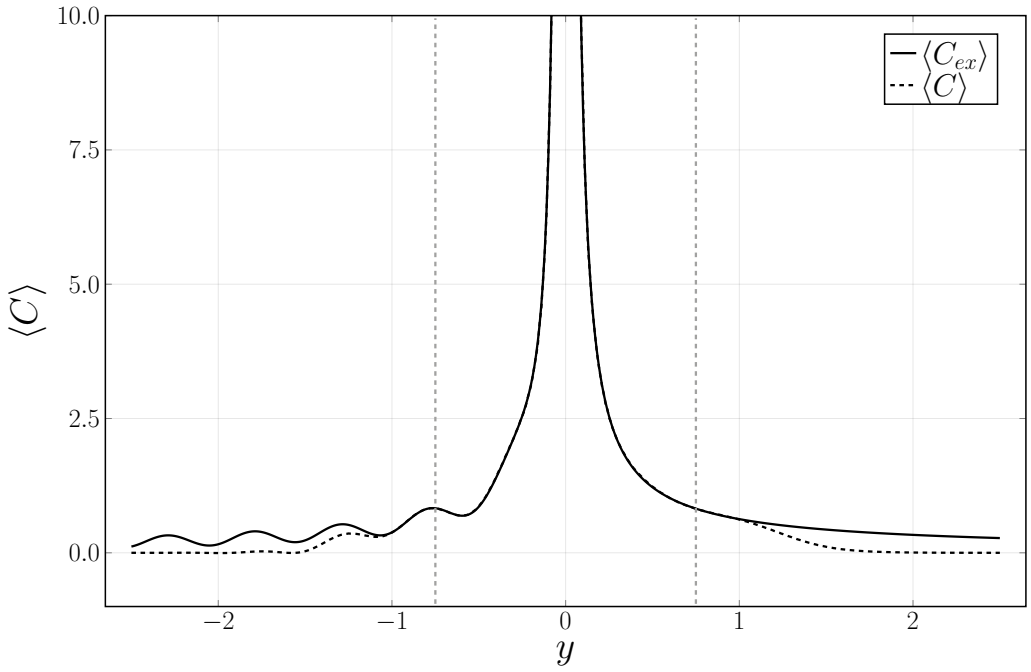

Figure 5.4: Analytic $\langle C_{ex} \rangle$ (continuous) and numeric $\langle C \rangle$ (dashed) suspended sediment concentrations in the sea along the line $x = 0$. The vertical grey dashed lines indicate the boundary between the interior domain and the PML. The friction coefficient is given by equation (5.2.21). The parameter values used are $\omega = 1$, $\Lambda = 2.5 \cdot 10^{-2}$, $\alpha_{\mathrm{r}} = 5$, $r_{\mathrm{p}} = 0.75$, $r_{\mathrm{b}} = 2.5$ and $n = 130617$.

The point source parametrisation

The leading order bottom evolution equation (5.2.24) shows that the bottom near the tidal inlet evolves too quickly to be able to solve this equation numerically or analytically. Thus, the current approach to model the sea-basin system by patching together a two-dimensional sea to an infinitely narrow one-dimensional basin does not work. To obtain a finite mass flux, an infinite velocity at the basin entrance is required. This locally infinite velocity whirls up a locally infinite amount of sediment and that leads to a very rapid bottom evolution near the tidal inlet. Hence, the effects of the narrow basin cannot be modelled as a point source forcing in the two-dimensional semi-infinite sea. It follows that other modelling techniques are needed and some of those are discussed in the further research section.

Conclusion

In this thesis, the morphodynamic interaction between an embayment and the adjacent sea has been studied. The one-dimensional, idealised, rectangular, tidal embayment is assumed to be short compared to the tidal wavelength and narrow compared to the Rossby radius of deformation and the channel length. The water motion is driven by the tide, which is prescribed at the seaward side, and the suspended sediment transport is dominated by diffusive transport processes. The tidal time scale is much shorter than the morphodynamic time scale, which allowed the to two time scales to be decoupled and justified the averaging over the short tidal time scale to study the long-term behaviour on the morphodynamic time scale.

When solely the embayment is considered with a fixed depth imposed at the entrance of the embayment (Chapter 3), a constantly sloping equilibrium profile is obtained with a spatially uniform along-basin velocity profile. It has been proven that the linear equilibrium bottom profile is asymptotically linear stable with respect to one-dimensional perturbations. A simplified no-flux boundary condition is derived, which is straightforward to implement and physically justified. The temporal evolution of the bottom has been investigated using this simplified no-flux boundary condition and the stability properties of the analytical and numerical problems are shown to be similar when linearised around the constantly sloping bottom, indicating that the numerical solution convergences to the analytical solution.

A novel approach is used to model the interaction between the embayment and the adjacent sea within a one-dimensional model (Chapter 4). An additional degree of freedom was added to the system to allow Dean's equilibrium bottom profile to be the sea equilibrium bottom profile, when the basin entrance is closed off. Subsequently, the system of equations is solved when the basin entrance is opened. At equilibrium, the bottom profile of the sea-basin system consisted of an increasingly sloping bottom in the sea and a constantly sloping bottom in the basin (***Q1***). The sea-basin equilibrium bottom profile turned out to be less stable than the basin equilibrium profile, although it was still asymptotically linear stable (***Q1***). The increasingly sloping bottom seemed to be in reasonable agreement with the coastal width-averaged bottom profiles reported by Ataei *et al.* (2015). An explicit relation between the equilibrium basin entrance height and the model parameters has been determined and it was shown that the basin entrance height only depends on the distance between the seaward boundary and the basin entrance. The tendency of the sea-basin system for the enhanced erosion near the basin entrance is explained using the total sediment transport. Furthermore, the linear equilibrium basin bottom profile provides evidence that the fixed basin entrance height is the correct boundary condition for models consisting of only an embayment. However, this boundary condition does not allow for the temporal evolution of the basin entrance height which is observed in nature and using this model. Nevertheless, for a properly chosen scaling of the entrance height, this effect is negligible (***Q2***).

The novel approach is applied to a system that consists of a one-dimensional basin and a two-dimensional semi-infinite sea (Chapter 5). The basin acted as a point source forcing in the two-dimensional sea domain. When the basin is closed off, the seabed is assumed to be flat. Once the basin opened, the morphodynamic equations are solved. A Perfectly Matched Layer is shown to be a convenient way to numerically incorporate the Sommerfeld radiation condition. Furthermore, it is shown that the point source parametrisation led to an unphysically quick bottom evolution near the tidal inlet. Thus, the narrow basin cannot be modelled as a point source forcing in the two-dimensional semi-infinite sea domain (***Q3***).

Further research

The sea-basin interaction and equilibrium bottom profile have been studied using a one-dimensional model. However, the dynamics in the sea are not one-dimensional and are much better described by a two-dimensional model, as is done in Chapter 5. We have shown that the basin influence cannot be parametrised as a point source forcing in the two-dimensional sea. Further research could use this model and investigate if a finite basin width or other interpretations of the infinite quantities could resolve the singular behaviour near the basin entrance. It could be investigated to what degree the results of the one-dimensional model remain valid for the two-dimensional model. Furthermore, it is expected that if the grid around the entrance is refined enough, some resemblance of the ebb-tidal delta could be found.

The one-dimensional bottom profile found in the sea-basin system could be compared to width-averaged seabed observations, to investigate if even a relatively simple one-dimensional model can already be used to make useful predictions.

During the derivation of the hydro-morphodynamic equations several simplifying assumptions have been made which should be checked in more detail. For example the influence of wind-driven flows on the suspended sediment concentration, the effect of wave breaking on the suspended sediment concentration, the overall erosion and deposition formulations, the erosion and deposition parameter values, the effect of using the full three-dimensional sediment concentration and velocity profile instead the depth-integrated formulation (as the horizontal suspended sediment transport would be skewed towards the bottom due to a relatively high sediment concentration near the seabed and decent flow velocities) and the influence of the moving landward boundary by reformulating the model as a proper moving boundary problem.

Bibliography

S. Ataei, M. Adjami, and M. Lashteh Neshaei, Mir Ahmad; Haghighifar. Classification of equilibrium beach profile in the Caspian Sea. *International Geoinformatics Reseach and Development Journal*, 6 (2), 2015. doi:10.13140/2.1.4437.8560.

J. Bezanson, S. Karpinski, V. B. Shah, and A. Edelman. Julia: A Fast Dynamic Language for Technical Computing. pages 1–27, 2012.

V. T. Buchwald. The diffraction of tides by a narrow channel. *Journal of Fluid Mechanics*, 46(3): 501–511, 1971. doi:10.1017/S0022112071000661.

H. Burchard. *Applied Turbulence Modelling in Marine Waters*. Springer, 2002. ISBN 9783540437956.

H. Burchard, R. D. Hetland, E. Schulz, and H. M. Schuttelaars. Drivers of Residual Estuarine Circulation in Tidally Energetic Estuaries: Straight and Irrotational Channels with Parabolic Cross Section. *Journal of Physical Oceanography*, 41(3):548–570, 2011. doi:10.1175/2010JPO4453.1.

K. F. Cheung, F. Gerritsen, and J. Cleveringa. Morphodynamics and Sand Bypassing at Ameland Inlet, The Netherlands. *Journal of Coastal Research*, 231(231):106–118, 2007. doi:10.2112/04-0403.1.

B. Cushman-Roisin and J.-M. Beckers. *Introduction to Geophysical Fluid Dynamics: Physical and Numerical Aspects*. Academic Press, 2009. ISBN 9780120887590.

V. N. De Jonge, K. Essink, and R. Boddeke. The Dutch Wadden Sea: a changed ecosystem. *Hydrobiologia*, 265:45–71, 1993. doi:10.1007/BF00007262.

H. De Swart and J. Zimmerman. Morphodynamics of Tidal Inlet Systems. *Annual Review of Fluid Mechanics*, 41(1):203–229, 2009. doi:10.1146/annurev.fluid.010908.165159.

H. E. De Swart and M. Blaas. Morphological evolutions in a 1d model for a dissipative tidal embayment. In J. Dronkers and M. Scheffers, editors, *Physics of Estuaries and Coastal Seas*, pages 305–314. Balkema, Rotterdam, 1998. ISBN 90-5410-965-3.

H. J. De Vriend. Mathematical modelling of meso-tidal barrier island coasts. Part I : Empirical and semi-empirical models. In P.-F. Liu, editor, *Advances in coastal and ocean engineering*, pages 115–149. World Scientific, Singapore, 1996. ISBN 981-02-2410-9.

H. J. De Vriend, J. Dronkers, M. J. F. Stive, and J. H. Wang. Coastal inlets and Tidal basins, 2002. URL `http://resolver.tudelft.nl/uuid:fc9bcc67-48db-4763-a121-86c7656099e4`.

R. G. Dean. Equilibrium Beach Profiles: Characteristics and Applications. *Journal of Coastal Research*, 7(1):53–84, 1991.

J. Ehlers. *The morphodynamics of the Wadden Sea*. Rotterdam, 1988. ISBN 9789061916796.

D. M. FitzGerald. Shoreline Erosional-Depositional Processes Associated with Tidal Inlets. In D. G. Aubrey and L. Weishar, editors, *Hydrodynamics and Sediment Dynamics of Tidal Inlets*, pages 186–225. Springer-Verlag, New York, 1988. ISBN 978-1-4757-4057-8.

J. D. Glaeser. Global distribution of barrier islands in terms of tectonic setting. *The journal of geology*, 86(3):283–297, 1978.

R. Haberman. *Applied Partial Differential Equations.* Pearson Education, 4th edition, 2005. ISBN 7-111-15910-1.

M. O. Hayes. General morphology and sediment patterns in tidal inlets. *Sedimentary Geology*, 26(1-3): 139–156, 1980. doi:10.1016/0037-0738(80)90009-3.

D. M. Hicks, T. M. Hume, A. Swales, and M. O. Green. Magnitudes, spatial extent, time scales and causes of shoreline change adjacent to an ebb tidal delta, Katikati inlet, New Zealand. *Journal of Coastal Research*, 15(1):220–240, 1999.

M. H. Holmes. *Introduction to Perturbation Methods.* Springer, 2nd edition, 2013. ISBN 978-1-4614-5476-2.

F. Ihlenburg. *Finite Element Analysis of Acoustic Scattering.* Springer-Verlag, New York, 1998. ISBN 0-387-98319-8.

M. S. Krol. *The method of averaging in partial differential equations.* Phd dissertation, Utrecht University, 1990.

C. C. Mei, M. Stiassnie, and D. K.-P. Yue. *Theory and applications of ocean surfacewaves.* World Scientific, 2005. ISBN 981-238-894-X.

J. C. J. Nihoul. *Modelling of Marine Systems.* Elsevier Scientific Publishing Company, Amsterdam, 1975. ISBN 0-444-41232-8.

J. Pedlosky. *Geophysical Fluid Dynamics.* R. R. Donnelley & Sons, 2nd edition, 1987. ISBN 0387963871.

J. A. Roelvink. Coastal morphodynamic evolution techniques. *Coastal Engineering*, 53(2-3):277–287, 2006. doi:10.1016/j.coastaleng.2005.10.015.

H. M. Schuttelaars. *Evolution and stability analysis of bottom patterns in a tidal embayment.* Phd dissertation, Utrecht University, 1997.

H. M. Schuttelaars and H. E. De Swart. An idealized long-term morphodynamic model of a tidal embayment. *European Journal of Mechanics, B/Fluids*, 15(1):55–80, 1996.

H. M. Schuttelaars and H. E. De Swart. Multiple morphodynamic equilibria in tidal embayments. *Journal of Geophysical Research*, 105(C10):24 105–24 118, oct 2000. doi:10.1029/2000JC900110.

J. P. M. Syvitski, R. L. Slingerland, P. Burgess, E. Meiburg, A. B. Murray, P. Wiberg, G. Tucker, and A. A. Voinov. Morphodynamic Models: An Overview. In C. A. Vionnet, M. H. Garcia, E. M. Latrubesse, and G. M. E. Perillo, editors, *River, Coastal and Estuarine Morphodynamics: RCEM 2009*, pages 3–20. Taylor & Francis, London, 2010. ISBN 978-0-415-55426-8.

M. C. Ter Brake. *Tidal Embayments.* Phd dissertation, Delft University of Technology, 2011.

G. M. Terra, W. J. Van de Berg, and L. R. M. Maas. Experimental verification of Lorentz' linearization procedure for quadratic friction. *Fluid Dynamics Research*, 36(3):175–188, 2005. doi:10.1016/j.fluiddyn.2005.01.005.

M. Van der Vegt. *Modeling the dynamics of barrier coasts and ebb-tidal deltas.* Phd dissertation, Utrecht University, 2006.

A. R. Van Dongeren and H. J. De Vriend. A model of morphological behaviour of tidal basins. *Coastal Engineering*, 22(3-4):287–310, 1994. doi:10.1016/0378-3839(94)90040-X.

E. Van Groesen and J. Molenaar. *Continuum Modeling in the Physical Sciences.* SIAM, 2007. ISBN 9780898716252.

J. Van Kan, A. Segal, and F. J. Vermolen. *Numerical Methods in Scientific Computing.* Delft Academic Press, Delft, 2nd edition, 2014. ISBN 97890-6562-3638.

S. M. Van Leeuwen. *Tidal inlet systems: bottom pattern formation and outer delta development.* Phd dissertation, Utrecht University, 2002.

L. C. Van Rijn. *Principles of sediment transport in rivers, estuaries and coastal seas.* Aqua Publications, Amsterdam, 1993. ISBN 90-800356-2-9.

F. Verhulst. *Nonlinear Differential Equations and Dynamical Systems.* Springer-Verlag, 1990. ISBN 3540506284.

C. B. Vreugdenhil. *Numerical methods for shallow-water flow.* Springer, 1994. ISBN 978-90-481-4472-3.

C. Vuik, F. J. Vermolen, M. B. Van Gijzen, and M. J. Vuik. *Numerical Methods for Ordinary Differential Equations.* Delft Academic Press, Delft, 2018. ISBN 978-90-6562-3737.

L. D. Wright and B. G. Thom. Coastal depositional landforms. *Progress in Physical Geography: Earth and Environment*, 1(3):412–459, 1977. doi:10.1177/030913337700100302.

Appendix A

Miscellaneous derivations

A.1 The log velocity profile

We consider the flow in a straight, rectangular, open channel that is driven by a pressure gradient. The x coordinate is directed along the channel. The x component of the three-dimensional shallow water flow is given by

$$\frac{\partial u}{\partial t} + u\frac{\partial u}{\partial x} + v\frac{\partial u}{\partial y} + w\frac{\partial u}{\partial z} - fv = -\frac{1}{\rho}\frac{\partial p}{\partial x} + \frac{\partial}{\partial x}\left(\mathcal{A}_{\mathrm{h}}\frac{\partial u}{\partial x}\right) + \frac{\partial}{\partial y}\left(\mathcal{A}_{\mathrm{h}}\frac{\partial u}{\partial y}\right) + \frac{\partial}{\partial z}\left(\mathcal{A}_{\mathrm{v}}\frac{\partial u}{\partial z}\right),$$

see equation (2.1.6b) and the corresponding section for a derivation. Assuming irrotational, fully developed flow directed along the x dimension that only depends on the depth $u = u(z)$, the above equation reduces to

$$\frac{\partial}{\partial z}\left(\mathcal{A}_{\mathrm{v}}\frac{\partial u}{\partial z}\right) - \frac{1}{\rho}\frac{\partial p}{\partial x} = 0.$$

The term in the brackets can be interpreted as a shear stress. Thus

$$\mathcal{A}_{\mathrm{v}}\frac{\partial u}{\partial z} = \frac{\tau}{\rho}. \tag{A.1.1}$$

The equation becomes

$$\frac{\partial}{\partial z}\left(\frac{\tau}{\rho}\right) = \frac{1}{\rho}\frac{\partial p}{\partial x}.$$

At the bottom of the channel, the shear stress divided by the density should be the square of the shear velocity or friction velocity and at the free surface the shear stress should vanish, hence the boundary conditions are

$$\frac{\tau}{\rho} = u_*^2 \quad \text{at} \quad z = 0 \qquad \text{and} \qquad \frac{\tau}{\rho} = 0 \quad \text{at} \quad z = H + \zeta.$$

The pressure gradient is assumed to be independent of the water depth. Integrating the equation and using the above boundary conditions results in

$$\frac{\tau}{\rho} = u_*^2\left(1 - \frac{z}{H+\zeta}\right).$$

A parabolic profile is assumed for the vertical eddy viscosity parameter:

$$\mathcal{A}_{\mathrm{v}} = \kappa u_*\left(1 - \frac{z}{H+\zeta}\right)z.$$

Here, κ is the von Kármán constant, usually taken as 0.4.

Using equation (A.1.1) with the parabolic eddy viscosity profile and integrating over the depth results in the log velocity profile:

$$u(z) = \frac{u_*}{\kappa} \ln\left(\frac{z}{z_0}\right),$$

where z_0 is the surface roughness parameter. This result is equivalent with the velocity profile presented in Van Rijn (1993, p. 7.59) for a flat bed.

A.2 The bottom evolution equation

Consider a control volume $\mathcal{V}$ from x_1 to x_2 with width B and height H. The total amount of deposited sediment inside the control volume $\mathcal{V}$ can change due to sediment fluxes through the boundaries of the control volume and due to sources and sinks in the body of the control volume. The volumetric bedload transport S_b represents the sliding, rolling and hopping of sediment along the bed, the sediment sink is the whirling up of sediment and the sediment source is the deposition of sediment. Thus the conservation of mass in the sediment layer implies that

$$\frac{d}{dt}\left(\int_{\mathcal{V}} \rho_\mathrm{s}(1-p)Bh\,dx\right) = \rho_\mathrm{s}(1-p)B\big(S_\mathrm{b}\big|_{x_1} - S_\mathrm{b}\big|_{x_2}\big) - \int_{\mathcal{V}} \alpha B u^2\,dx + \int_{\mathcal{V}} \frac{\omega_\mathrm{s}^2}{\kappa_\mathrm{v}} B\beta C\,dx,$$

where ρ_s is the density of the sediment particles and p is the porosity of the sediment layer.

The control volume $\mathcal{V}$ does not depend on time, thus the time derivative can be taken into the integral. Furthermore, the width B is assumed to be a nonzero constant and can be eliminated. Rewriting the flux difference in integral form and taking everything to the LHS yields

$$\int_{\mathcal{V}} \left\{\rho_\mathrm{s}(1-p)\left(\frac{\partial h}{\partial t} + \frac{\partial S_\mathrm{b}}{\partial x}\right) + \alpha u^2 - \frac{\omega_\mathrm{s}^2}{\kappa_\mathrm{v}}\beta C\right\} dx = 0.$$

This equation holds for any control volume $\mathcal{V}$, thus it follows that the integrand is zero. Rewriting the integrand yields the bottom evolution equation

$$\rho_\mathrm{s}(1-p)\left(\frac{\partial h}{\partial t} + \frac{\partial S_\mathrm{b}}{\partial x}\right) = -\alpha u^2 + \frac{\omega_\mathrm{s}^2}{\kappa_\mathrm{v}}\beta C.$$

A parametrisation of the volumetric bedload flux is given by

$$S_\mathrm{b} = \hat{s}\frac{|u|^b}{u_\mathrm{c}^b}\left(\frac{u}{|u|} - \mu_*\frac{\partial h}{\partial x}\right),$$

see for example Schuttelaars (1997); Ter Brake (2011). Here, $b > 1$ is a constant, μ_* is a bed slope correction coefficient (to model the preferred downhill transport), u_c is the critical erosion velocity and $\hat{s}$ is a parameter that is a function of the sediment properties.

A.3 The smoothed bottom profile

The bottom profile consisting of Dean's bottom profile and the nearly flat bed is given by

$$h(x) = \begin{cases} 1-(1-dx)^{2/3}, & \text{if } x < x_\mathrm{i}, \\ 1-(1-dx_\mathrm{i})^{2/3}\big[1-(\frac{x-x_\mathrm{i}}{1-x_\mathrm{i}})^m\big], & \text{if } x > x_\mathrm{i}. \end{cases}$$

Here, m is a scale parameter. At the interface the first derivative is discontinuous. Near the interface the bed can be approximated by

$$h_\mathrm{i}(x) = \begin{cases} 1-(1-dx)^{2/3} + \frac{2d}{3\sqrt[3]{1-x_\mathrm{i}d}}(x-x_\mathrm{i}), & \text{if } x < x_\mathrm{i}, \\ 1-(1-dx_\mathrm{i})^{2/3}, & \text{if } x > x_\mathrm{i}, \end{cases}$$

as can be derived by retaining the first-order Taylor terms only. A smooth local bed can be obtained by computing the convolution with a smoothing function. The chosen smoothing function is $g(x) = \frac{1}{2\gamma}e^{-\gamma|x|}$ with γ a parameter that determines the smoothness. The prefactor is chosen such that the integral of the smoothing function is normalized. By combing Dean's profile, the convolution $h_{\mathrm{i}}(x) * g(x)$ and the nearly flat bed profile, the smoothed bottom profile is obtained

$$h(x) = \begin{cases} 1-(1-dx)^{2/3}, & \text{if } x < x_{\mathrm{i}} - \delta, \\ 1-(1-dx_{\mathrm{i}})^{2/3} + \frac{d}{3\sqrt[3]{1-dx_{\mathrm{i}}}}\big(2(x-x_{\mathrm{i}}) - \frac{1}{\gamma}e^{\gamma(x-x_{\mathrm{i}})}\big), & \text{if } x_{\mathrm{i}} - \delta < x < x_{\mathrm{i}} \\ 1-(1-dx_{\mathrm{i}})^{2/3} - \frac{d}{3\sqrt[3]{1-dx_{\mathrm{i}}}}\frac{1}{\gamma}e^{-\gamma(x-x_{\mathrm{i}})}, & \text{if } x_{\mathrm{i}} < x < x_{\mathrm{i}} + \delta \\ 1-(1-dx_{\mathrm{i}})^{2/3}\big[1-(\frac{x-x_{\mathrm{i}}}{1-x_{\mathrm{i}}})^{m}\big], & \text{if } x > x_{\mathrm{i}} + \delta, \end{cases} \tag{A.3.1}$$

where δ is a small constant. In this thesis, the following values are taken: $\gamma = 500$ and $\delta = 0.01$.

A.4 The shallow water equations in cylindrical coordinates

In this section, the shallow water equations in cylindrical coordinates are derived. The derivation is rather concise as the derivation is similar to the derivation in Cartesian coordinates carried out in Chapter 2.

A.4.1 Three-dimensional water equations

The incompressible continuity equation and the incompressible Navier-Stokes equations are used to represent the conservation of mass and momentum respectively. In cylindrical coordinates, these equations are respectively given by

$$\begin{cases} \frac{1}{r}\frac{\partial}{\partial r}(ru_r) + \frac{1}{r}\frac{\partial u_\varphi}{\partial \varphi} + \frac{\partial u_z}{\partial z} = 0, & \text{(A.4.1a)} \\ \frac{\partial u_r}{\partial t} + u_r\frac{\partial u_r}{\partial r} + \frac{u_\varphi}{r}\frac{\partial u_r}{\partial \varphi} + u_z\frac{\partial u_r}{\partial z} - \frac{u_\varphi^2}{r} & \text{(A.4.1b)} \\ \qquad = -\frac{1}{\rho}\frac{\partial p}{\partial r} + \nu\left(\frac{1}{r}\frac{\partial}{\partial r}\left(r\frac{\partial u_r}{\partial r}\right) + \frac{1}{r^2}\frac{\partial^2 u_r}{\partial \varphi^2} + \frac{\partial^2 u_r}{\partial z^2} - \frac{u_r}{r^2} - \frac{2}{r^2}\frac{\partial u_\varphi}{\partial \varphi}\right), \\ \frac{\partial u_\varphi}{\partial t} + u_r\frac{\partial u_\varphi}{\partial r} + \frac{u_\varphi}{r}\frac{\partial u_\varphi}{\partial \varphi} + u_z\frac{\partial u_\varphi}{\partial z} + \frac{u_r u_\varphi}{r} & \text{(A.4.1c)} \\ \qquad = -\frac{1}{\rho r}\frac{\partial p}{\partial \varphi} + \nu\left(\frac{1}{r}\frac{\partial}{\partial r}\left(r\frac{\partial u_\varphi}{\partial r}\right) + \frac{1}{r^2}\frac{\partial^2 u_\varphi}{\partial \varphi^2} + \frac{\partial^2 u_\varphi}{\partial z^2} - \frac{u_\varphi}{r^2} + \frac{2}{r^2}\frac{\partial u_r}{\partial \varphi}\right), \\ \frac{\partial u_z}{\partial t} + u_r\frac{\partial u_z}{\partial r} + \frac{u_\varphi}{r}\frac{\partial u_z}{\partial \varphi} + u_z\frac{\partial u_z}{\partial z} & \text{(A.4.1d)} \\ \qquad = -\frac{1}{\rho}\frac{\partial p}{\partial z} + \nu\left(\frac{1}{r}\frac{\partial}{\partial r}\left(r\frac{\partial u_z}{\partial r}\right) + \frac{1}{r^2}\frac{\partial^2 u_z}{\partial \varphi^2} + \frac{\partial^2 u_z}{\partial z^2}\right) - g, \end{cases}$$

where u_r is the radial flow velocity component, u_φ is the angular flow velocity component, u_z the vertical flow velocity component, ρ is the fluid density, p is the pressure, ν is the kinematic viscosity and g is the gravitational acceleration, which is assumed to be constant. The Coriolis terms are neglected. The variables are all functions of the three cylindrical coordinates (r, φ, z) and time t.

Using Reynolds decomposition and the fact that the water is shallow, it follows that the mean flow

variables satisfy the equations

$$\begin{cases} \dfrac{1}{r}\dfrac{\partial}{\partial r}(ru_r) + \dfrac{1}{r}\dfrac{\partial u_\varphi}{\partial \varphi} + \dfrac{\partial u_z}{\partial z} = 0, & \text{(A.4.2a)} \\ \dfrac{\partial u_r}{\partial t} + u_r\dfrac{\partial u_r}{\partial r} + \dfrac{u_\varphi}{r}\dfrac{\partial u_r}{\partial \varphi} + u_z\dfrac{\partial u_r}{\partial z} - \dfrac{u_\varphi^2}{r} & \text{(A.4.2b)} \\ \qquad = -\dfrac{1}{\rho}\dfrac{\partial p}{\partial r} + \dfrac{1}{r}\dfrac{\partial}{\partial r}\left(r\mathcal{A}_\mathrm{h}\dfrac{\partial u_r}{\partial r}\right) + \dfrac{1}{r^2}\dfrac{\partial}{\partial \varphi}\left(\mathcal{A}_\mathrm{h}\dfrac{\partial u_r}{\partial \varphi}\right) + \dfrac{\partial}{\partial z}\left(\mathcal{A}_\mathrm{h}\dfrac{\partial u_r}{\partial z}\right) - \mathcal{A}_\mathrm{h}\dfrac{u_r}{r^2} - \dfrac{2}{r^2}\mathcal{A}_\mathrm{h}\dfrac{\partial u_\varphi}{\partial \varphi}, & \\ \dfrac{\partial u_\varphi}{\partial t} + u_r\dfrac{\partial u_\varphi}{\partial r} + \dfrac{u_\varphi}{r}\dfrac{\partial u_\varphi}{\partial \varphi} + u_z\dfrac{\partial u_\varphi}{\partial z} + \dfrac{u_r u_\varphi}{r} & \text{(A.4.2c)} \\ \qquad = -\dfrac{1}{\rho r}\dfrac{\partial p}{\partial \varphi} + \dfrac{1}{r}\dfrac{\partial}{\partial r}\left(r\mathcal{A}_\mathrm{h}\dfrac{\partial u_\varphi}{\partial r}\right) + \dfrac{1}{r^2}\dfrac{\partial}{\partial \varphi}\left(\mathcal{A}_\mathrm{h}\dfrac{\partial u_\varphi}{\partial \varphi}\right) + \dfrac{\partial}{\partial z}\left(\mathcal{A}_\mathrm{h}\dfrac{\partial u_\varphi}{\partial z}\right) - \mathcal{A}_\mathrm{h}\dfrac{u_\varphi}{r^2} + \dfrac{2}{r^2}\mathcal{A}_\mathrm{h}\dfrac{\partial u_\varphi}{\partial \varphi}, & \\ \dfrac{\partial p}{\partial z} = -\rho g. & \text{(A.4.2d)} \end{cases}$$

Here, $\mathcal{A}_\mathrm{h}$ is a horizontal eddy viscosity coefficient.

A.4.2 Depth-averaging

Kinematic boundary conditions

At the interface between water and air, a kinematic boundary condition is prescribed. The water parcels at the free surface can never leave the free surface and thus $z = H + \zeta(r, \varphi, t)$. Taking the material derivative (D/Dt) and using that for the angular velocity it holds that $\partial\varphi/\partial t = u_\varphi/r$ gives

$$u_z = \frac{\partial \zeta}{\partial t} + u_r\frac{\partial \zeta}{\partial r} + \frac{u_\varphi}{r}\frac{\partial \zeta}{\partial \varphi} \quad \text{at} \quad z = \zeta + H.$$

Similarly, at the interface between the water and the seabed, a kinematic boundary condition is used. This results in

$$u_z = \frac{\partial h}{\partial t} + u_r\frac{\partial h}{\partial r} + \frac{u_\varphi}{r}\frac{\partial h}{\partial \varphi} \quad \text{at} \quad z = h.$$

Depth-averaging the conservation of mass equation

Integrating the continuity equation (A.4.2a) over the depth and using that the depth does not depend on the radial distance r yields

$$\frac{1}{r}\int_h^{H+\zeta}\frac{\partial}{\partial r}(ru_r)\,dz + \frac{1}{r}\int_h^{H+\zeta}\frac{\partial u_\varphi}{\partial \varphi}\,dz + \big[u_z\big]_h^{H+\zeta} = 0.$$

Using Leibniz integral rule (2.2.9) results in

$$\frac{1}{r}\frac{\partial}{\partial r}\left(r\int_h^{H+\zeta}u_r\,dz\right) + \frac{1}{r}\frac{\partial}{\partial \varphi}\left(\int_h^{H+\zeta}u_\varphi\,dz\right) + \left[u_r\frac{\partial h}{\partial r} + \frac{u_\varphi}{r}\frac{\partial h}{\partial \varphi} - u_z\right]_h - \left[u_r\frac{\partial \zeta}{\partial r} + \frac{u_\varphi}{r}\frac{\partial \zeta}{\partial \varphi} - u_z\right]_{H+\zeta} = 0.$$

The averaged radial velocity and averaged angular velocity are defined as

$$\bar{u}_r = \frac{1}{H+\zeta-h}\int_h^{H+\zeta}u_r\,dz \qquad \text{and} \qquad \bar{u}_\varphi = \frac{1}{H+\zeta-h}\int_h^{H+\zeta}u_\varphi\,dz.$$

Using the averaged velocities and the kinematic boundary conditions one finds

$$\frac{\partial \zeta}{\partial t} - \frac{\partial h}{\partial t} + \frac{1}{r}\frac{\partial}{\partial r}\big[r(H+\zeta-h)\bar{u}_r\big] + \frac{1}{r}\frac{\partial}{\partial \varphi}\big[(H+\zeta-h)\bar{u}_\varphi\big] = 0.$$

Depth-averaged conservation of momentum equations

Using the hydrostatic balance, integrating the conservation of momentum equations over the water depth and using that the eddy viscosity coefficients are much smaller than the bottom friction yields

$$\begin{cases} \dfrac{\partial \bar{u}_r}{\partial t} + \bar{u}_r \dfrac{\partial \bar{u}_r}{\partial r} + \dfrac{\bar{u}_\varphi}{r}\dfrac{\partial \bar{u}_r}{\partial \varphi} - \dfrac{\bar{u}_\varphi^2}{r} = -g\dfrac{\partial \zeta}{\partial r} - \dfrac{r^*\bar{u}_r}{H+\zeta-h+h_0}, & \text{(A.4.3a)} \\ \dfrac{\partial \bar{u}_\varphi}{\partial t} + \bar{u}_r \dfrac{\partial \bar{u}_\varphi}{\partial r} + \dfrac{\bar{u}_\varphi}{r}\dfrac{\partial \bar{u}_\varphi}{\partial \varphi} + \dfrac{\bar{u}_r \bar{u}_\varphi}{r} = -\dfrac{g}{r}\dfrac{\partial \zeta}{\partial \varphi} + \dfrac{r^*\bar{u}_\varphi}{H+\zeta-h+h_0}, & \text{(A.4.3b)} \end{cases}$$

where the small constant h_0 is introduced to ensure that the Lorentz linearised bottom friction terms are finite.

A.4.3 Circularly symmetric

Assuming that the flow is circularly symmetric, it follows that all the variables are independent of the angle φ, i.e. the variables are uniform in φ, and thus $\partial/\partial\varphi = 0$. Furthermore, the angular velocity u_φ is assumed to be small. It follows that the one-dimensional shallow water equations are given by

$$\begin{cases} \dfrac{\partial \zeta}{\partial t} - \dfrac{\partial h}{\partial t} + \dfrac{1}{r}\dfrac{\partial}{\partial r}\big[r(H+\zeta-h)\bar{u}_r\big] = 0, & \text{(A.4.4a)} \\ \dfrac{\partial \bar{u}_r}{\partial t} + \bar{u}_r \dfrac{\partial \bar{u}_r}{\partial r} = -g\dfrac{\partial \zeta}{\partial r} - \dfrac{r^*\bar{u}_r}{H+\zeta-h+h_0}. & \text{(A.4.4b)} \end{cases}$$

Nondimensionalization and simplifying

The characteristic scales are substituted into equations (A.4.4a–b) to nondimensionalize the equations. Then using the characteristic values typical of the sea, the following dominant balances are obtained:

$$\begin{cases} \dfrac{\partial \zeta}{\partial t} + \dfrac{1}{r}\dfrac{\partial}{\partial r}\big[r(1+\varepsilon\zeta-h)\bar{u}_r\big] = 0, & \text{(A.4.5a)} \\ \dfrac{\partial \bar{u}_r}{\partial t} = -\Lambda\dfrac{\partial \zeta}{\partial r} - \dfrac{\hat{r}\bar{u}_r}{1+\varepsilon\zeta-h+h_0}, & \text{(A.4.5b)} \end{cases}$$

where the variables ζ, h, $\bar{u}_r$, r and t are order one and the nondimensional parameters are given by $\varepsilon = U/(\sigma L)$, $\Lambda = gH/(\sigma^2 L^2)$ and $\hat{r} = r^*/(\sigma H)$. Here, U is a characteristic velocity scale, σ the semidiurnal angular frequency scale, L a length scale, H is a depth scale and r^* a friction scale.

A.5 Application of the matching conditions

If instead of the normalized flux boundary condition (5.2.14) the basin flux matching condition (5.2.8) is used, then the free surface solution of Helmholtz equation (5.2.17) without friction is given by

$$\zeta_\mathrm{s}(r,t) = \frac{\omega b u_\mathrm{b}|_{x=0}}{\pi\Lambda}\big(J_0(kr)\cos\omega t + Y_0(kr)\sin\omega t\big).$$

Using the Taylor expansion and that $b \ll 1$ shows the leading order free surface matching condition (5.2.9) is given by

$$\zeta_\mathrm{b} = \frac{\omega b u_\mathrm{b}|_{x=0}}{\pi\Lambda}\left(\cos\omega t + \frac{2}{\pi}\left[\ln\left(\frac{kb}{2}\right) + \gamma - 1\right]\sin\omega t\right) + \mathcal{O}\big(b^2\big),$$

where γ is the Euler–Mascheroni constant.

Appendix B

Numerical implementation

All numerical schemes and code are written and implemented by the author in Julia (Bezanson *et al.*, 2012).

B.1 The diffusively dominated transport equation

A Finite Element Method (FEM), the θ-method and the Newton–Raphson method are used to numerically solve the following nonlinear partial differential equation resulting from diffusively dominated transport in a tidal embayment:

$$\frac{\partial h}{\partial \tau} = \frac{1}{2}\frac{\partial^2}{\partial x^2}\left(\frac{x-1}{1-h}\right)^2 + f_\mathrm{s}, \tag{B.1.1}$$

see equation (3.3.6) and the corresponding section for a derivation. Here, the source function $f_\mathrm{s}(x,\tau)$ is added for generality. The boundary conditions are $h(x=0)=0$ and $\langle F\rangle(x=1)=0$, where the averaged flux $\langle F\rangle$ is given by equation (3.3.5).

B.1.1 The Galerkin equations

We derive the weak form of equation (B.1.1). The bottom evolution equation (B.1.1) is multiplied with a test function $\varphi(x)$ and the resulting equation is integrated over the spatial domain. Using integration by parts and using the boundary conditions results in the following weak formulation:

$$(\mathcal{W}_1)\ :\ \begin{cases} \text{Find } h \in C^1\big((0,T], H^1(0,1)\big) \text{ with } h(x=0)=0 \text{ such that:} \\ \dfrac{d}{d\tau}\displaystyle\int_0^1 \varphi h\,dx = \int_0^1 -\frac{1}{2}\frac{d\varphi}{dx}\frac{\partial}{\partial x}\left(\frac{x-1}{1-h}\right)^2 dx + \int_0^1 \varphi f_\mathrm{s}\,dx, \\ \text{for all } \varphi \in H^1(0,1),\ \varphi(0)=0. \end{cases}$$

Here, $H^1(\Omega) = \{u \in L^2(\Omega) \,|\, u_{x_1}, \ldots, u_{x_n} \in L^2(\Omega)\}$ is the Sobolev space that contains square integrable functions with square integrable partial derivatives and $L^2(\Omega) = \{u : \Omega \to \mathbb{R} \,|\, \int_\Omega |u|^2\,d\Omega < \infty\}$ is the square integrable Lebesgue space. The notation $u(t,\boldsymbol{x}) \in C^1\big((0,T], H^1(\Omega)\big)$ denotes that u is continuous on $(0,T]$ and for each time $t \in (0,T]$ it holds that $u(t,\boldsymbol{x})$ is in $H^1(\Omega)$.

To obtain a finite system of equations, it is assumed that the solution can be written as a sum of chosen basis functions $\varphi_j(x)$ as follows: $h = \sum_{j=1}^n h_j(\tau)\varphi_j(x)$, where the coefficients $h_j(\tau)$ need to be determined. Furthermore, it is assumed that the test functions in the weak formulation are from the same set of functions as the chosen basis functions, therefore $\varphi(x) = \varphi_i(x)$. Substitution into weak form $\mathcal{W}_1$ results in the Galerkin equations:

$$\sum_{j=1}^n \int_0^1 \varphi_i\varphi_j\,dx\frac{dh_j}{d\tau} = \int_0^1 -\frac{1}{2}\frac{d\varphi_i}{dx}\frac{\partial}{\partial x}\left(\frac{x-1}{1-\sum_{j=1}^n h_j\varphi_j}\right)^2 dx + \int_0^1 \varphi_i f_\mathrm{s}\,dx.$$

The nonlinear Galerkin equations can be written in matrix vector form as

$$M\frac{d\boldsymbol{h}}{d\tau} = \boldsymbol{F}(\boldsymbol{h},\tau), \tag{B.1.2}$$

where we have defined

$$\begin{gathered}\boldsymbol{h} = [h_1\ h_2\ \ldots\ h_n]^T, \quad M_{ij} = \int_0^1 \varphi_i\varphi_j\,dx,\\ F_i(\boldsymbol{h},\tau) = \underbrace{\int_0^1 -\frac{1}{2}\frac{d\varphi_i}{dx}\frac{\partial}{\partial x}\left(\frac{x-1}{1-\sum_{j=1}^n h_j\varphi_j}\right)^2 dx}_{S_i(\boldsymbol{h})} + \underbrace{\int_0^1 \varphi_i f_\mathrm{s}\,dx}_{f_i}.\end{gathered} \tag{B.1.3}$$

B.1.2 The steady-state problem

Before considering the time-depended problem, first, the conceptually simpler steady-state problem is solved. At steady state, the solution does not change anymore, thus $d\boldsymbol{h}/d\tau = \boldsymbol{0}$ and $h_j(\tau) = h_j$. Hence, the following system of nonlinear equations is solved:

$$\boldsymbol{F}(\boldsymbol{h}) = \boldsymbol{0}. \tag{B.1.4}$$

This nonlinear system of equations is solved using the Newton-Raphson method (Vuik *et al.*, 2018). Using the multidimensional Taylor expansion of $\boldsymbol{F}(\boldsymbol{h})$ at $\boldsymbol{h}^-$, it follows that

$$\boldsymbol{F}(\boldsymbol{h}^- + \boldsymbol{\delta h}) = \boldsymbol{F}(\boldsymbol{h}^-) + \frac{\partial \boldsymbol{F}}{\partial \boldsymbol{h}}(\boldsymbol{h}^-)\boldsymbol{\delta h} + \mathcal{O}\big(\boldsymbol{\delta h}^2\big), \tag{B.1.5}$$

where $\boldsymbol{h}^-$ is the previous computed iterate, $\boldsymbol{\delta h}$ is a new variable which represents the change in $\boldsymbol{h}$ and $\frac{\partial \boldsymbol{F}}{\partial \boldsymbol{h}}(\boldsymbol{h}^-)$ is the Jacobi matrix which is given by

$$\frac{\partial F_i}{\partial h_j}(\boldsymbol{h}^-) = \int_0^1 -\frac{d\varphi_i}{dx}\frac{d}{dx}\left(\frac{(x-1)^2\varphi_j}{(1-\sum_{p=1}^n h_p^-\varphi_p)^3}\right) dx. \tag{B.1.6}$$

As stated in equation (B.1.4), we want to find an $\boldsymbol{h}$ such that $\boldsymbol{F}(\boldsymbol{h}) = \boldsymbol{0}$. Instead of solving for the root of $\boldsymbol{F}(\boldsymbol{h})$, we solve for the root of the linear approximation of $\boldsymbol{F}(\boldsymbol{h})$ given by equation (B.1.5) by neglecting the higher-order terms. Henceforth, the following linear system is solved for $\boldsymbol{\delta h}$:

$$\frac{\partial \boldsymbol{F}}{\partial \boldsymbol{h}}(\boldsymbol{h}^-)\boldsymbol{\delta h} = -\boldsymbol{F}(\boldsymbol{h}^-). \tag{B.1.7}$$

To ensure convergence, even for poor initial guesses, relaxed Newton-Rapson iterations are used with relaxation parameter ω. For $0 < \omega \leq 1$, the next iterate is given by

$$\boldsymbol{h} = \boldsymbol{h}^- + \omega\boldsymbol{\delta h}.$$

If $\omega = 1$ then the original Newton-Raphson method is recovered. The value of ω is determined using Algorithm 1.

Algorithm 1 The ω algorithm

```
ω ← 1
while max(h⁻ + ωδh) > 1 do
    ω ← ω/2
end while
```

The element matrix of $\frac{\partial \boldsymbol{F}}{\partial \boldsymbol{h}}(\boldsymbol{h}^-)$ and element vectors of $S_i(\boldsymbol{h}^-)$ and f_i are derived next, see equation (B.1.3) and equation (B.1.6) respectively for their definitions. Since the integral over the whole spatial

domain can be split into a sum of the integrals over the elements $e_k = (x_k, x_{k+1})$ that partition the domain, it follows that

$$\frac{\partial F_i}{\partial h_j}(\boldsymbol{h}^-) = \int_0^1 -\frac{d\varphi_i}{dx}\frac{d}{dx}\left(\frac{(x-1)^2\varphi_j}{(1-\sum_p h_p^-\varphi_p)^3}\right)dx = \sum_{k=1}^{n_{\mathrm{el}}}\int_{e_k} -\frac{d\varphi_i}{dx}\frac{d}{dx}\left(\frac{(x-1)^2\varphi_j}{(1-\sum_p h_p^-\varphi_p)^3}\right)dx = \sum_{k=1}^{n_{\mathrm{el}}}\frac{\partial F_i^{e_k}}{\partial h_j}(\boldsymbol{h}^-),$$

$$S_i(\boldsymbol{h}^-) = \int_0^1 -\frac{1}{2}\frac{d\varphi_i}{dx}\frac{d}{dx}\left(\frac{x-1}{1-\sum_p h_p^-\varphi_p}\right)^2 dx = \sum_{k=1}^{n_{\mathrm{el}}}\int_{e_k} -\frac{1}{2}\frac{d\varphi_i}{dx}\frac{d}{dx}\left(\frac{x-1}{1-\sum_p h_p^-\varphi_p}\right)^2 dx = \sum_{k=1}^{n_{\mathrm{el}}} S_i^{e_k}(\boldsymbol{h}^-),$$

$$f_i = \int_0^1 \varphi_i f_{\mathrm{s}}\,dx = \sum_{k=1}^{n_{\mathrm{el}}}\int_{e_k}\varphi_i f_{\mathrm{s}}\,dx = \sum_{k=1}^{n_{\mathrm{el}}} f_i^{e_k}.$$

Linear basis functions are used that satisfy $\varphi_i(x_j) = \delta_{ij}$. The linear basis functions can be written as $\varphi_i(x) = \alpha_i + \beta_i x$ on e_k. The integrals in $\frac{\partial F_i^{e_k}}{\partial h_j}(\boldsymbol{h}^-)$ and $S_i^{e_k}(\boldsymbol{h}^-)$ can be evaluated *analytically* and for the integral found in $f_i^{e_k}$ a Newton-Cotes quadrature is used. From a physical point of view, the bed height cannot be higher than the water height and thus we require $h < 1$. For $h_i^- < 1$ we have for the integrals that

$$\frac{\partial F_i^{e_k}}{\partial h_j}(\boldsymbol{h}^-) = \int_{e_k} -\beta_i\frac{d}{dx}\left(\frac{(x-1)^2\varphi_j}{(1-(h_k^-\varphi_k + h_{k+1}^-\varphi_{k+1}))^3}\right)dx = \beta_i\left\{\frac{(x_k-1)^2}{(1-h_k^-)^3}\delta_{jk} - \frac{(x_{k+1}-1)^2}{(1-h_{k+1}^-)^3}\delta_{jk+1}\right\},$$

$$S_i^{e_k}(\boldsymbol{h}^-) = \int_{e_k} -\frac{1}{2}\beta_i\frac{d}{dx}\left(\frac{x-1}{1-(h_k^-\varphi_k + h_{k+1}^-\varphi_{k+1})}\right)^2 dx = \frac{1}{2}\beta_i\left\{\left(\frac{x_k-1}{1-h_k^-}\right)^2 - \left(\frac{x_{k+1}-1}{1-h_{k+1}^-}\right)^2\right\},$$

$$f_i^{e_k} = \int_{e_k}\varphi_i f_{\mathrm{s}}\,dx \overset{\mathrm{NC}}{\approx} \frac{x_{k+1}-x_k}{2}\big(f(x_k)\delta_{ik} + f(x_{k+1})\delta_{ik+1}\big).$$

It follows that on element $e_k = (x_k, x_{k+1})$, the only nonzero basis functions are φ_k and φ_{k+1}, the basis functions corresponding to the vertices of element e_k. Thus only if $i, j \in \{k, k+1\}^2$ there are contributions towards element e_k. For linear basis functions on e_k it holds that $\beta_i = \mp 1/(x_{k+1} - x_k)$ for $i \in \{k, k+1\}$. We find for $h_i^- < 1$ that the element matrix and element vectors are given by

$$\frac{\partial F^{e_k}}{\partial h}(\boldsymbol{h}^-) = \begin{bmatrix} \frac{\partial F_k^{e_k}}{\partial h_k} & \frac{\partial F_k^{e_k}}{\partial h_{k+1}} \\ \frac{\partial F_{k+1}^{e_k}}{\partial h_k} & \frac{\partial F_{k+1}^{e_k}}{\partial h_{k+1}} \end{bmatrix} = \frac{1}{x_{k+1}-x_k}\begin{bmatrix} -\frac{(x_k-1)^2}{(1-h_k^-)^3} & \frac{(x_{k+1}-1)^2}{(1-h_{k+1}^-)^3} \\ \frac{(x_k-1)^2}{(1-h_k^-)^3} & -\frac{(x_{k+1}-1)^2}{(1-h_{k+1}^-)^3} \end{bmatrix},$$

$$S^{e_k}(\boldsymbol{h}^-) = \begin{bmatrix} S_k^{e_k} \\ S_{k+1}^{e_k} \end{bmatrix} = \frac{1}{2(x_{k+1}-x_k)}\left\{\left(\frac{x_k-1}{1-h_k^-}\right)^2 - \left(\frac{x_{k+1}-1}{1-h_{k+1}^-}\right)^2\right\}\begin{bmatrix} -1 \\ 1 \end{bmatrix},$$

$$f^{e_k} = \begin{bmatrix} f_k^{e_k} \\ f_{k+1}^{e_k} \end{bmatrix} = \frac{x_{k+1}-x_k}{2}\begin{bmatrix} f_{\mathrm{s}}(x_k) \\ f_{\mathrm{s}}(x_{k+1}) \end{bmatrix}.$$

Only at the landward boundary at $x = 1$, it can be the case that $h = 1$. Thus on element $k = n-1$, we can have $h_n^- = 1$. Then we can write $h_{n-1}^-\varphi_{n-1} + h_n^-\varphi_n = 1 + \gamma(x-1)$ for some $\gamma > 0$. Substitution of this expression into the element integrals yields

$$\frac{\partial F_i^{e_{n-1}}}{\partial h_j}(\boldsymbol{h}^-) = \int_{e_{n-1}} \beta_i\frac{d}{dx}\left(\frac{\varphi_j}{\gamma^3(x-1)}\right)dx = \begin{cases} 0, & \text{if } \varphi_j = \varphi_{n-1} = \hat{\gamma}(x-1) \\ \pm\infty, & \text{if } \varphi_j = \varphi_n = 1 + \tilde{\gamma}(x-1) \end{cases},$$

$$S_i^{e_{n-1}}(\boldsymbol{h}^-) = \int_{e_{n-1}} -\frac{1}{2}\beta_i\frac{d}{dx}\left(\frac{1}{\gamma^2}\right)dx = 0.$$

Whenever $h_n^- = 1$, the following element matrix and vector are obtained

$$\frac{\partial F^{e_{n-1}}}{\partial h}(\boldsymbol{h}^-) = \begin{bmatrix} \frac{\partial F_k^{e_{n-1}}}{\partial h_{n-1}} & \frac{\partial F_{n-1}^{e_{n-1}}}{\partial h_n} \\ \frac{\partial F_n^{e_{n-1}}}{\partial h_{n-1}} & \frac{\partial F_n^{e_{n-1}}}{\partial h_n} \end{bmatrix} = \begin{bmatrix} 0 & \infty \\ 0 & -\infty \end{bmatrix},$$

$$S^{e_{n-1}}(\boldsymbol{h}^-) = \begin{bmatrix} S_{n-1}^{e_{n-1}} \\ S_n^{e_{n-1}} \end{bmatrix} = \begin{bmatrix} 0 \\ 0 \end{bmatrix}.$$

The current discretization does not allow the natural boundary condition $\langle F \rangle = 0$ at $x = 1$. On the one hand, if $h \neq 1$ at $x = 1$, then the last column of the *element* matrix $\frac{\partial F^{e_{n-1}}}{\partial h}$ vanishes resulting in a zero column in the matrix $\frac{\partial \boldsymbol{F}}{\partial \boldsymbol{h}}$ of linear system (B.1.7) that we wanted to solve. On the other hand, when $h = 1$ at $x = 1$, then the element matrix $\frac{\partial F^{e_{n-1}}}{\partial h}$ contains infinite entries which do not cancel in the matrix $\frac{\partial \boldsymbol{F}}{\partial \boldsymbol{h}}$ of linear system (B.1.7). In both cases, the matrix $\frac{\partial \boldsymbol{F}}{\partial \boldsymbol{h}}$ is singular and, thus, the boundary condition $\langle F \rangle = 0$ at $x = 1$ is not allowed using the current discretization.

Instead, the Dirichlet boundary condition $h = 1$ at $x = 1$ is used, since the seabed should not contain a jump at the landward side. This simplified boundary condition is derived in Section 3.3.3. This Dirichlet boundary condition resolves our problem since whenever $h_n = 1$ then $\delta h_n = 0$. Hence the last column of $\frac{\partial \boldsymbol{F}}{\partial \boldsymbol{h}}$ does not influence the solution and can be eliminated. Furthermore, since $\delta h_n = 0$ does not influence the other nodes, it follows that the no-flux natural boundary condition is automatically applied at the previous node x_{n-1}. In the limit of $\Delta x \to 0$, it holds that x_{n-1} goes to $x_n = 1$ and thus the original boundary condition is recovered.

Method of manufactured solutions: Steady state

To verify the derivation and the FEM implementation, the numerical solution is compared to the exact solution. Often no closed-form solution exists and the only way to solve the problem is using numerical means. However, the method of manufactured solutions can be used to resolve this issue. An exact solution is chosen which satisfies both boundary conditions. This solution is substituted into the differential equation and the source term is chosen such that the chosen solution is the solution.

The chosen manufactured solution that satisfies both boundary conditions is

$$h_{\mathrm{m}}(x) = 1 + \frac{x - 1}{\sqrt{1 + b\big((1 - x)^m - 1\big)}},$$

with $m \in \mathbb{N}\backslash\{1\}$ and $b < 1$. Substituting the manufactured solution into equation (B.1.1) with $\partial h/\partial \tau = 0$ shows that the source function is given by

$$f_{\mathrm{s}}(x) = -\frac{1}{2} bm(m - 1)(1 - x)^{m-2}.$$

To investigate the order of convergence the mean absolute error (mae), the root mean squared error (rmse) and the maximum error (max) are introduced

$$\begin{aligned} \|e\|_{\mathrm{mae}} &= \frac{1}{n} \sum_{i=1}^{n} |e_i|, \\ \|e\|_{\mathrm{rmse}} &= \sqrt{\frac{1}{n} \sum_{i=1}^{n} |e_i|^2}, \\ \|e\|_{\max} &= \max\big\{|e_i|,\, i = 1, \ldots, n\big\}, \end{aligned} \tag{B.1.8}$$

where the error is defined as $e_i = h_i - h_{\mathrm{m}}(x_i)$.

The manufactured solution, the numerical approximation and the corresponding error for $b = 0.99$ and $m = 3$ are shown in Figure B.1. The numerical solution uses $n = 30$ nodes. In Figure B.1a it can be seen that the numerical solution computed with 30 nodes already approximates the analytical solution rather well. Figure B.1b shows that when the grid spacing Δx is halved the error $\|e\|$ decreases four times, hence $\|e\| = \mathcal{O}(\Delta x^2)$. This is in line with the theoretical rate of convergence for linear elements (Van Kan *et al.*, 2014, p. 158).

In Figure B.2, the analytical solution, the numerical solution and the corresponding error are shown for $b = 0.99$ and $m = 2$. It can be seen that the numerical solution with 30 nodes does not accurately describe the analytical solution yet. Moreover, observe that the error only decreases with order $\mathcal{O}(\Delta x)$

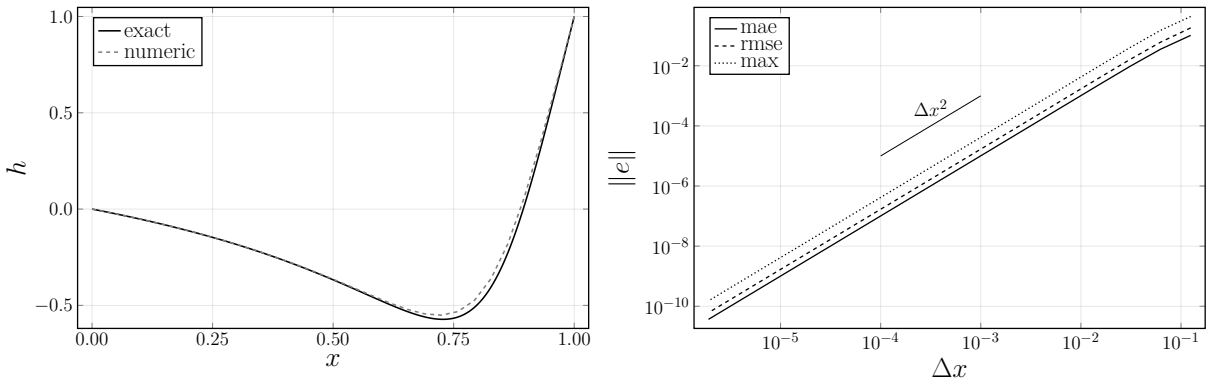

(a) The solution (b) The error

Figure B.1: (a) Analytical (solid black) and numerical (dotted grey) nondimensional bottom profiles for $b = 0.99$ and $m = 3$. The numerical solution is computed with $n = 30$ nodes. (b) Convergence of the error measured in the norms defined in equation (B.1.8).

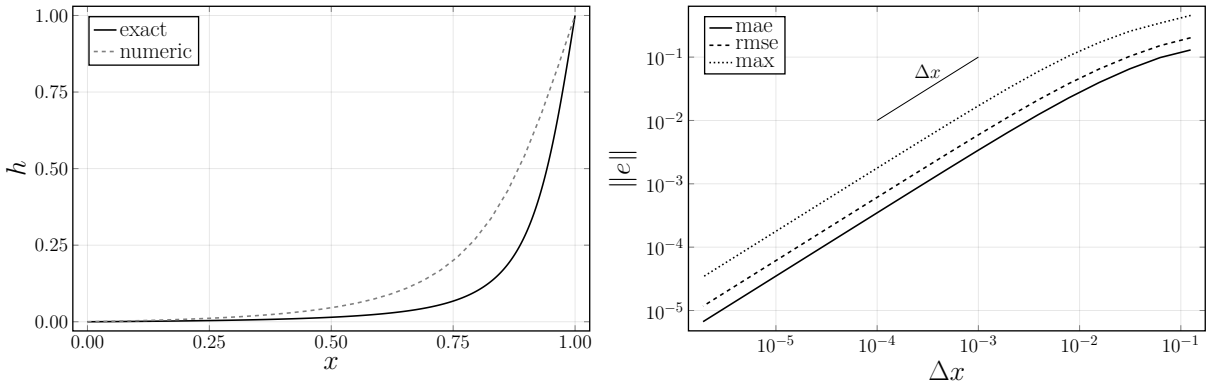

(a) The solution (b) The error

Figure B.2: (a) Analytical (solid black) and numerical (dotted grey) nondimensional bottom profiles for $b = 0.99$ and $m = 2$. The numerical solution is computed with $n = 30$ nodes. (b) Convergence of the corresponding error measured in the norms defined in equation (B.1.8).

here, while the theoretical convergence rate for linear elements is order $\mathcal{O}(\Delta x^2)$, as was found with the previous manufactured solution. It is expected that the slower convergence is caused by the nonvanishing source function f_s at the right boundary for $m = 2$. For higher values of m, the error decreases with order $\mathcal{O}(\Delta x^2)$.

B.1.3 The time-dependent problem

The resulting time-dependent equation is solved using the θ-method (Vuik *et al.*, 2018). Using the θ-method to discretise equation (B.1.2) in time yields

$$M\frac{\boldsymbol{h}^{n+1}-\boldsymbol{h}^n}{\Delta\tau} = \theta\boldsymbol{F}(\boldsymbol{h}^{n+1},\tau^{n+1}) + (1-\theta)\boldsymbol{F}(\boldsymbol{h}^n,\tau^n),$$

with $\theta \in [0,1]$. For $\theta = 0$ forward Euler is obtained, while for $\theta = 1$ backward Euler is acquired. Thus the θ-method can be seen as a linear combination of the forward and backward Euler methods. For $\theta = 1/2$ the scheme is called the Crank–Nicolson method, which is second-order accurate in time.

Continuing our somewhat unusual but mathematically convenient notation, we define the wanted quantity as $\boldsymbol{h} = \boldsymbol{h}^{n+1}$, the solution from the previous time step as $\boldsymbol{h}^{(1)} = \boldsymbol{h}^n$, the new time as $\tau = \tau^{n+1}$ and the previous time as $\tau^{(1)} = \tau^n$. The nonlinear equation can be written in the standard form as follows:

$$\boldsymbol{\mathcal{F}}(\boldsymbol{h},\tau) \equiv \theta\boldsymbol{F}(\boldsymbol{h},\tau) + (1-\theta)\boldsymbol{F}\big(\boldsymbol{h}^{(1)},\tau^{(1)}\big) - \frac{1}{\Delta\tau}M\big(\boldsymbol{h}-\boldsymbol{h}^{(1)}\big) = 0. \tag{B.1.9}$$

Again, the Newton-Raphson method is used to solve the nonlinear system. Neglecting the higher-order terms in the Taylor expansion of equation (B.1.9) and solving for the root of the resulting linear function shows that the following linear system needs to be solved:

$$\frac{\partial\boldsymbol{\mathcal{F}}}{\partial\boldsymbol{h}}(\boldsymbol{h}^-,\tau)\boldsymbol{\delta h} = -\boldsymbol{\mathcal{F}}(\boldsymbol{h}^-,\tau),$$

where $\boldsymbol{h}^-$ is the previous iterate of $\boldsymbol{h}$. The next iterate is then found using a relaxed Newton-Raphson step:

$$\boldsymbol{h} = \boldsymbol{h}^- + \omega\boldsymbol{\delta h}.$$

The value of ω is determined using Algorithm 1. Once the solution for a given previous time step $\boldsymbol{h}^{(1)}$ has sufficiently converged, we set $\boldsymbol{h}^{(1)} = \boldsymbol{h}$ and the process repeats itself. The solution has sufficiently converged whenever $\|\boldsymbol{\delta h}\|_\mathrm{max} < 10^{-8}$.

By direct computation, it follows that

$$\frac{\partial\mathcal{F}_i}{\partial h_j}(\boldsymbol{h}^-,\tau) = \theta\frac{\partial F_i}{\partial h_j}(\boldsymbol{h}^-,\tau) - \frac{1}{\Delta\tau}M_{ij}.$$

The term $\frac{\partial F_i}{\partial h_j}(\boldsymbol{h}^-)$ has already been computed in equation (B.1.6).

The only element matrix that needs to be derived is that of M_{ij} as the other element matrices and vectors have already been derived for the steady-state problem. From equation (B.1.3), it follows that

$$M_{ij} = \int_0^1 \varphi_i\varphi_j\,dx = \sum_{k=1}^{n_\mathrm{el}}\int_{e_k}\varphi_i\varphi_j\,dx = \sum_{k=1}^{n_\mathrm{el}} M^{e_k}.$$

Using the Holand & Bell theorem in $\mathbb{R}^1$ we can evaluate the element integral to obtain

$$M^{e_k} = \int_{e_k}\varphi_i\varphi_j\,dx = \frac{(x_{k+1}-x_k)}{6}(1+\delta_{ij}),$$

and the element matrix is therefore given by

$$M^{e_k} = \begin{bmatrix} M^{e_k}_{kk} & M^{e_k}_{k+1} \\ M^{e_k}_{k+1k} & M^{e_k}_{k+1k+1}\end{bmatrix} = \frac{(x_{k+1}-x_k)}{6}\begin{bmatrix}2 & 1\\ 1 & 2\end{bmatrix}.$$

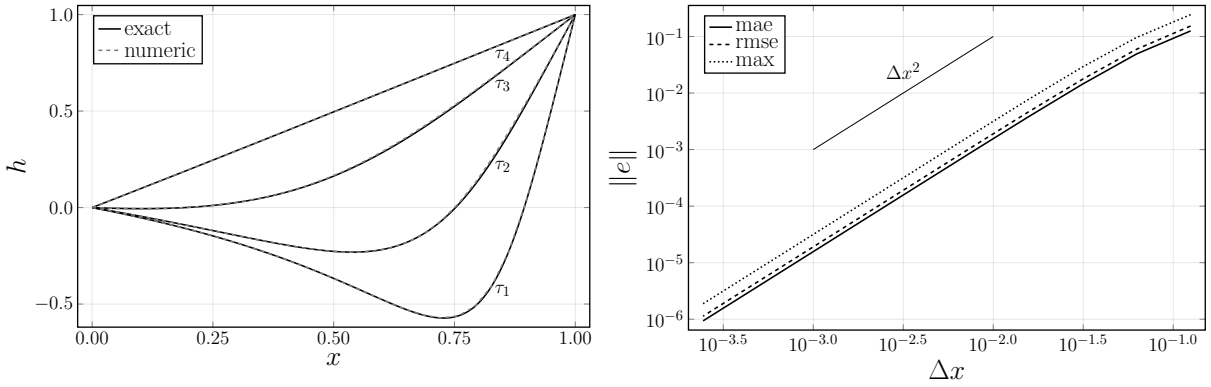

(a) The solution

(b) The error

Figure B.3: (a) Evolution of the analytical (solid black) and numerical (dashed grey) nondimensional bottom profiles for $b = 0.99$, $m = 3$, $\alpha = 2$, $n = 30$ and time step $\Delta t = 10^{-3}$. The solutions are shown at $\tau_1 = 0$, $\tau_2 = 0.02$, $\tau_3 = 0.15$ and $\tau_4 = 2$ and are almost almost indistinguishable. (b) Convergence of the error measured in the norms defined in equation (B.1.8).

Method of manufactured solutions: Time dependent

Similar to the steady-state case, a manufactured solution is used to test the numerical implementation of the derived schemes. The chosen time-dependent manufactured solution is

$$h_{\mathrm{m}}(x,\tau) = 1 + \frac{x-1}{\sqrt{1 + be^{-\alpha\tau}\big((1-x)^m - 1\big)}}, \tag{B.1.10}$$

with $\alpha > 0$. Substitution into the time-dependent PDE shows that the source function is given by

$$f_{\mathrm{s}}(x,\tau) = \frac{1}{2}be^{-\alpha\tau}\left(\frac{\alpha(x-1)\big((1-x)^m - 1\big)}{\big(1 + be^{-\alpha\tau}\big((1-x)^m - 1\big)\big)^{3/2}} - m(m-1)(1-x)^{m-2}\right). \tag{B.1.11}$$

In this thesis the Crank–Nicolson method is used, which corresponds to choosing $\theta = 1/2$. The error theoretically scales with $\|e\| = \mathcal{O}(\Delta t^2 + \Delta x^2)$ for $\theta = 1/2$. Whenever $\Delta t = \mathcal{O}(\Delta x)$, it follows that $\|e\| = \mathcal{O}(\Delta x^2)$.

Figure B.3 shows how the numerical and analytical bottom profiles evolve in time and, moreover, that the error indeed scales with $\|e\| = \mathcal{O}(\Delta x^2)$ as theoretically predicted. The bottom profile is initially given by the steady-state manufactured solution with $b = 0.99$ and $m = 3$, and evolves towards the linear equilibrium bottom profile (3.3.7).

B.2 The Helmholtz equation

In this section, the discretized Helmholtz equation is derived. The Helmholtz equation, which was derived under the assumption of periodic flow and includes the effects of viscosity and of a variable bottom, is given in coordinate invariant form by

$$\nabla \cdot \left[\frac{\Lambda(1 - h_{\mathrm{s}}^{\mathrm{b}} - h_{\mathrm{s}}^{\mathrm{r}})}{1 + i\frac{\hat{r}}{\omega(1-h_{\mathrm{s}}^{\mathrm{b}} - h_{\mathrm{s}}^{\mathrm{r}})}}\nabla\eta_{\mathrm{s}}^{\mathrm{r}}\right] + \omega^2\eta_{\mathrm{s}}^{\mathrm{r}} = i\omega\nabla\big[h_{\mathrm{s}}^{\mathrm{r}}\boldsymbol{U}_{\mathrm{s}}^{\mathrm{b}}\big] + f_{\mathrm{s}}, \tag{B.2.1}$$

see equation (5.2.11). Here, f_{s} is a source term added for generality. There is no water flow through the coast, hence the normal flow vanishes at the coastal boundary. Thus $\boldsymbol{u}_{\mathrm{s}}^{\mathrm{r}} \cdot \boldsymbol{n} = 0$ at $x = 0$ which implies using equation (5.2.10) that $\partial\eta_{\mathrm{s}}^{\mathrm{r}}/\partial n = 0$ at $x = 0$. For the seaward boundary, it is assumed that there are only outgoing waves, hence a Sommerfeld type boundary condition is prescribed (see equation (5.2.18)

for the analytical Sommerfeld radiation condition at infinity). For a fixed bottom without friction, a simple numerical non-reflective boundary condition is of the form

$$\frac{\partial \eta_{\mathrm{s}}^{\mathrm{r}}}{\partial n} - ik\eta_{\mathrm{s}}^{\mathrm{r}} = 0 \quad \text{on} \quad \Gamma_1, \tag{B.2.2}$$

with $k = \omega/c$ and Γ_1 is the semicircular seaward boundary. However, as pointed out by Ihlenburg (1998, p. 8), this numerical boundary condition is only satisfied approximately by the analytical solution:

$$\eta_{\mathrm{s}}^{\mathrm{r}} = \mathcal{O}\left(\frac{1}{\sqrt{R}}\right), \qquad \frac{\partial \eta_{\mathrm{s}}^{\mathrm{r}}}{\partial n} - ik\eta_{\mathrm{s}}^{\mathrm{r}} = \mathcal{O}\left(\frac{1}{\sqrt{R}}\right), \qquad R \to \infty.$$

Thus, a numerical solution satisfying boundary condition (B.2.2) does not converge to the true analytical solution satisfying the Sommerfeld radiation condition but, instead, to the exact solution satisfying boundary condition (B.2.2). Viscosity is added to the Helmholtz equation such that the seawards boundary is easier to implement. Because, if the waves generated in the centre of the domain dampen out quickly, then the boundary condition at the seaward side does not influence these waves. The used numerical boundary condition reads

$$\frac{\partial \eta_{\mathrm{s}}^{\mathrm{r}}}{\partial n} - i\omega\sqrt{\frac{1 + i\frac{\hat{r}}{\omega(1-h_{\mathrm{s}}^{\mathrm{b}}-h_{\mathrm{s}}^{\mathrm{r}})}}{\Lambda(1-h_{\mathrm{s}}^{\mathrm{b}}-h_{\mathrm{s}}^{\mathrm{r}})}}\,\eta_{\mathrm{s}}^{\mathrm{r}} = H_{\mathrm{b}} \quad \text{on} \quad \Gamma_2,$$

where on the RHS the function H_{b} is added for generality.

B.2.1 The Galerkin equations

Multiplying the Helmholtz equation (B.2.1) with a test function $\varphi(\boldsymbol{x})$, integrating over the spatial domain and application of integration by parts and the boundary conditions results in the weak form:

$$(\mathcal{W}_2) \;:\; \begin{cases} \text{Find } \eta_{\mathrm{s}}^{\mathrm{r}} \in H^1(\Omega) \text{ such that:} \\ \displaystyle\int_\Omega -\nabla\varphi \cdot \left(\frac{\Lambda(1-h_{\mathrm{s}}^{\mathrm{b}}-h_{\mathrm{s}}^{\mathrm{r}})}{1+i\frac{\hat{r}}{\omega(1-h_{\mathrm{s}}^{\mathrm{b}}-h_{\mathrm{s}}^{\mathrm{r}})}}\nabla\eta_{\mathrm{s}}^{\mathrm{r}}\right) + \omega^2\varphi\eta_{\mathrm{s}}^{\mathrm{r}}\,d\Omega + \int_{\Gamma_2} i\omega\sqrt{\frac{\Lambda(1-h_{\mathrm{s}}^{\mathrm{b}}-h_{\mathrm{s}}^{\mathrm{r}})}{1+i\frac{\hat{r}}{\omega(1-h_{\mathrm{s}}^{\mathrm{b}}-h_{\mathrm{s}}^{\mathrm{r}})}}}\varphi\eta_{\mathrm{s}}^{\mathrm{r}}\,d\Gamma \\ \qquad = \displaystyle\int_\Omega i\omega\varphi\nabla\cdot(h_{\mathrm{s}}^{\mathrm{r}}\boldsymbol{U}_{\mathrm{s}}^{\mathrm{b}}) + \varphi f_{\mathrm{s}}\,d\Omega + \int_{\Gamma_2} -\frac{\Lambda(1-h_{\mathrm{s}}^{\mathrm{b}}-h_{\mathrm{s}}^{\mathrm{r}})}{1+i\frac{\hat{r}}{\omega(1-h_{\mathrm{s}}^{\mathrm{b}}-h_{\mathrm{s}}^{\mathrm{r}})}}H_{\mathrm{b}}\varphi\,d\Gamma, \\ \text{for all } \varphi \in H^1(\Omega). \end{cases}$$

To obtain a finite system of equations it is assumed that $\eta = \sum_{j=1}^{n}\eta_j\varphi_j(\boldsymbol{x})$ and $\varphi = \varphi_i$. Substitution into the linear weak formulation of Helmholtz equation results in the Galerkin Equations:

$$\sum_{j=1}^{n}\eta_j\overbrace{\left(\int_\Omega -\frac{\Lambda(1-h_{\mathrm{s}}^{\mathrm{b}}-h_{\mathrm{s}}^{\mathrm{r}})}{1+i\frac{\hat{r}}{\omega(1-h_{\mathrm{s}}^{\mathrm{b}}-h_{\mathrm{s}}^{\mathrm{r}})}}\nabla\varphi_i\cdot\nabla\varphi_j + \omega^2\varphi_i\varphi_j\,d\Omega + \int_{\Gamma_2} i\omega\sqrt{\frac{\Lambda(1-h_{\mathrm{s}}^{\mathrm{b}}-h_{\mathrm{s}}^{\mathrm{r}})}{1+i\frac{\hat{r}}{\omega(1-h_{\mathrm{s}}^{\mathrm{b}}-h_{\mathrm{s}}^{\mathrm{r}})}}}\varphi_i\varphi_j\,d\Gamma\right)}^{S_{ij}}$$
$$= \underbrace{\int_\Omega i\omega\varphi_i\nabla\cdot(h_{\mathrm{s}}^{\mathrm{r}}\boldsymbol{U}_{\mathrm{s}}^{\mathrm{b}}) + \varphi_i f_{\mathrm{s}}\,d\Omega + \int_{\Gamma_2} -\frac{\Lambda(1-h_{\mathrm{s}}^{\mathrm{b}}-h_{\mathrm{s}}^{\mathrm{r}})}{1+i\frac{\hat{r}}{\omega(1-h_{\mathrm{s}}^{\mathrm{b}}-h_{\mathrm{s}}^{\mathrm{r}})}}H_{\mathrm{b}}\varphi_i\,d\Gamma}_{f_i},$$

where S_{ij} and f_i have been defined.

B.2.2 Linear triangular elements

Since the elements partition the domain and the boundary elements partition the boundary, it follows that

$$S_{ij} = \sum_{k=1}^{n_{\mathrm{el}}} S_{ij}^{e_k} + \sum_{k=1}^{n_{\mathrm{bel}}} S_{ij}^{be_k} \qquad \text{and} \qquad f_i = \sum_{k=1}^{n_{\mathrm{el}}} f_i^{e_k} + \sum_{k=1}^{n_{\mathrm{bel}}} f_i^{be_k}.$$

Linear triangular elements are used. The linear elements can be written as $\varphi_i(\boldsymbol{x}) = \alpha_i + \beta_i x + \gamma_i y$ and therefore $\nabla\varphi_i \cdot \nabla\varphi_j = \beta_i\beta_j + \gamma_i\gamma_j$. The node indices of element e_k are denoted with k_1, k_2 and k_3. The node indices of boundary element b_k are denoted with k_1 and k_2. Using Holand & Bell's theorem and Newton-Côtes quadratures it follows that

$$\begin{aligned}
S_{ij}^{e_k} &= \int_{e_k} -\frac{\Lambda(1-h_{\mathrm{s}}^{\mathrm{b}}-h_{\mathrm{s}}^{\mathrm{r}})}{1+i\frac{\hat{r}}{\omega(1-h_{\mathrm{s}}^{\mathrm{b}}-h_{\mathrm{s}}^{\mathrm{r}})}}\nabla\varphi_i\cdot\nabla\varphi_j + \omega^2\varphi_i\varphi_j\,d\Omega \overset{\text{NC\&HB}}{\approx} -(\beta_i\beta_j+\gamma_i\gamma_j)\frac{|\Delta_e|}{6}\sum_{p\in\{k_1,k_2,k_3\}}\frac{\Lambda\big(1-h_{\mathrm{s}}^{\mathrm{b}}(\boldsymbol{x}_p)-h_{\mathrm{s}}^{\mathrm{r}}(\boldsymbol{x}_p)\big)}{1+i\frac{\hat{r}(\boldsymbol{x}_p)}{\omega(1-h_{\mathrm{s}}^{\mathrm{b}}(\boldsymbol{x}_p)-h_{\mathrm{s}}^{\mathrm{r}}(\boldsymbol{x}_p))}} \\
&\qquad + \omega^2\frac{|\Delta_e|}{24}(1+\delta_{ij}), \\
S_{ij}^{be_k} &= \int_{be_k} i\omega\sqrt{\frac{\Lambda(1-h_{\mathrm{s}}^{\mathrm{b}}-h_{\mathrm{s}}^{\mathrm{r}})}{1+i\frac{\hat{r}}{\omega(1-h_{\mathrm{s}}^{\mathrm{b}}-h_{\mathrm{s}}^{\mathrm{r}})}}}\varphi_i\varphi_j\,d\Gamma \overset{\text{NC}}{\approx} i\omega\frac{\|\boldsymbol{x}_{k_2}-\boldsymbol{x}_{k_1}\|}{2}\sum_{p\in\{k_1,k_2\}}\sqrt{\frac{\Lambda\big(1-h_{\mathrm{s}}^{\mathrm{b}}(\boldsymbol{x}_p)-h_{\mathrm{s}}^{\mathrm{r}}(\boldsymbol{x}_p)\big)}{1+i\frac{\hat{r}(\boldsymbol{x}_p)}{\omega(1-h_{\mathrm{s}}^{\mathrm{b}}(\boldsymbol{x}_p)-h_{\mathrm{s}}^{\mathrm{r}}(\boldsymbol{x}_p))}}}\delta_{ip}\delta_{jp}, \\
f_i^{e_k} &= \int_{e_k} i\omega\varphi_i\nabla\cdot(h_{\mathrm{s}}^{\mathrm{r}}\boldsymbol{U}_{\mathrm{s}}^{\mathrm{b}}) + \varphi_i f_{\mathrm{s}}\,d\Omega \overset{\text{NC}}{\approx} \frac{|\Delta_e|}{6}\sum_{p\in\{k_1,k_2,k_3\}}\Big(i\omega h_{\mathrm{s}}^{\mathrm{r}}(\boldsymbol{x}_p)\big(U_{\mathrm{s}}^{\mathrm{b}}(\boldsymbol{x}_p)\beta_p + V_{\mathrm{s}}^{\mathrm{b}}(\boldsymbol{x}_p)\gamma_p\big) + \delta_{ip}f_{\mathrm{s}}(\boldsymbol{x}_p)\Big), \\
f_i^{be_k} &= \int_{be_k} -\frac{\Lambda(1-h_{\mathrm{s}}^{\mathrm{b}}-h_{\mathrm{s}}^{\mathrm{r}})}{1+i\frac{\hat{r}}{\omega(1-h_{\mathrm{s}}^{\mathrm{b}}-h_{\mathrm{s}}^{\mathrm{r}})}}H_{\mathrm{b}}\varphi_i\,d\Gamma \overset{\text{NC}}{\approx} -\frac{\|\boldsymbol{x}_{k_2}-\boldsymbol{x}_{k_1}\|}{2}\sum_{p\in\{k_1,k_2\}}\frac{\Lambda\big(1-h_{\mathrm{s}}^{\mathrm{b}}(\boldsymbol{x}_p)-h_{\mathrm{s}}^{\mathrm{r}}(\boldsymbol{x}_p)\big)}{1+i\frac{\hat{r}(\boldsymbol{x}_p)}{\omega(1-h_{\mathrm{s}}^{\mathrm{b}}(\boldsymbol{x}_p)-h_{\mathrm{s}}^{\mathrm{r}}(\boldsymbol{x}_p))}}H_{\mathrm{b}}(\boldsymbol{x}_p)\delta_{ip}.
\end{aligned}$$

The element matrix is formed by letting $i,j \in \{k_1,k_2,k_3\}^2$, the boundary element matrix is formed by letting $i,j \in \{k_1,k_2\}^2$, the element vector is formed by letting $i \in \{k_1,k_2,k_3\}$ and the boundary element vector by $i \in \{k_1,k_2\}$.

If the source function is $f_{\mathrm{s}} = i\omega Q\delta(\boldsymbol{x})$ as is the case in equation (5.2.11), then the above derivation of the element vector is not correct. Instead, it follows that

$$\int_{e_k}\varphi_i f_{\mathrm{s}}\,d\Omega = \begin{cases} i\omega Q\varphi_i(\boldsymbol{0}), & \text{if } \boldsymbol{0}\in e_k, \\ 0, & \text{else.}\end{cases}$$

Thus, we need to determine if the point source is located inside an element. Let the vertices of element e_k be given by $\boldsymbol{x}_{k_1}$, $\boldsymbol{x}_{k_2}$ and $\boldsymbol{x}_{k_3}$. A point $\boldsymbol{a}$ is located inside element e_k, if

$$\big|\Delta(\boldsymbol{x}_{k_1},\boldsymbol{x}_{k_2},\boldsymbol{a})\big| + \big|\Delta(\boldsymbol{a},\boldsymbol{x}_{k_2},\boldsymbol{x}_{k_3})\big| + \big|\Delta(\boldsymbol{x}_{k_1},\boldsymbol{a},\boldsymbol{x}_{k_3})\big| = \big|\Delta(\boldsymbol{x}_{k_1},\boldsymbol{x}_{k_2},\boldsymbol{x}_{k_3})\big|,$$

where $\big|\Delta(\boldsymbol{x}_{k_1},\boldsymbol{x}_{k_2},\boldsymbol{x}_{k_3})\big|$ denotes the area of the triangle with vertices $\boldsymbol{x}_{k_1}$, $\boldsymbol{x}_{k_2}$ and $\boldsymbol{x}_{k_3}$. Round off errors spoil the exact equality. Hence a small parameter ε is added to the RHS. The condition becomes

$$\big|\Delta(\boldsymbol{x}_{k_1},\boldsymbol{x}_{k_2},\boldsymbol{a})\big| + \big|\Delta(\boldsymbol{a},\boldsymbol{x}_{k_2},\boldsymbol{x}_{k_3})\big| + \big|\Delta(\boldsymbol{x}_{k_1},\boldsymbol{a},\boldsymbol{x}_{k_3})\big| \le \big|\Delta(\boldsymbol{x}_{k_1},\boldsymbol{x}_{k_2},\boldsymbol{x}_{k_3})\big| + \varepsilon.$$

B.2.3 The velocity field

Once the free surface $\eta_{\mathrm{s}}^{\mathrm{r}}$ is known then the velocity fields can be found using the equations:

$$U_{\mathrm{s}}^{\mathrm{r}} = \frac{\Lambda}{i\omega\big(1+i\frac{\hat{r}}{\omega(1-h_{\mathrm{s}}^{\mathrm{b}}-h_{\mathrm{s}}^{\mathrm{r}})}\big)}\frac{\partial\eta_{\mathrm{s}}^{\mathrm{r}}}{\partial x} \qquad \text{and} \qquad V_{\mathrm{s}}^{\mathrm{r}} = \frac{\Lambda}{i\omega\big(1+i\frac{\hat{r}}{\omega(1-h_{\mathrm{s}}^{\mathrm{b}}-h_{\mathrm{s}}^{\mathrm{r}})}\big)}\frac{\partial\eta_{\mathrm{s}}^{\mathrm{r}}}{\partial y}. \tag{B.2.3}$$

see equation (5.2.10). Here, we focus on $U_{\mathrm{s}}^{\mathrm{r}}$ but the FEM discretization of $V_{\mathrm{s}}^{\mathrm{r}}$ goes analogously. Multiplying equation (B.2.3) with $\varphi(\boldsymbol{x})$ and integrating over the domain yields the weak form:

$$\begin{cases} \text{Find } U_{\mathrm{s}}^{\mathrm{r}} \in H^0(\Omega) \text{ such that:} \\ \displaystyle\int_\Omega U_{\mathrm{s}}^{\mathrm{r}}\varphi\,d\Omega = \int_\Omega \frac{\Lambda}{i\omega\big(1+i\frac{\hat{r}}{\omega(1-h_{\mathrm{s}}^{\mathrm{b}}-h_{\mathrm{s}}^{\mathrm{r}})}\big)}\varphi\frac{\partial\eta_{\mathrm{s}}^{\mathrm{r}}}{\partial x}\,d\Omega, \\ \text{for all } \varphi \in H^0(\Omega). \end{cases}$$

Assuming that $\varphi(\boldsymbol{x}) = \varphi_i(\boldsymbol{x})$ and $U_{\mathrm{s}}^{\mathrm{r}} = \sum_{j=1}^{n} U_{\mathrm{s},j}^{\mathrm{r}} \varphi_j(\boldsymbol{x})$ yields the Galerkin equations:

$$\sum_{j=1}^{n} U_{\mathrm{s},j}^{\mathrm{r}} \underbrace{\int_{\Omega} \varphi_i \varphi_j \, d\Omega}_{S_{ij}} = \underbrace{\int_{\Omega} \frac{\Lambda}{i\omega\big(1 + i\frac{\hat{r}}{\omega(1-h_{\mathrm{s}}^{\mathrm{b}}-h_{\mathrm{s}}^{\mathrm{r}})}\big)} \varphi \frac{\partial \eta_{\mathrm{s}}^{\mathrm{r}}}{\partial x} \, d\Omega}_{f_i}.$$

The integral over the whole domain is the same as the sum over the elements. Assuming linear triangular elements, it follows that

$$S_{ij}^{e_k} = \int_{e_k} \varphi_i \varphi_j \, d\Omega = \frac{|\Delta_e|}{24}(1 + \delta_{ij}),$$

$$f_i^{e_k} = \int_{e_k} \frac{\Lambda}{i\omega\big(1 + i\frac{\hat{r}}{\omega(1-h_{\mathrm{s}}^{\mathrm{b}}-h_{\mathrm{s}}^{\mathrm{r}})}\big)} \varphi \frac{\partial \eta_{\mathrm{s}}^{\mathrm{r}}}{\partial x} \, d\Omega \approx \frac{|\Delta_e|}{6} \frac{\Lambda}{i\omega\big(1 + i\frac{\hat{r}(\boldsymbol{x}_i)}{\omega(1-h_{\mathrm{s}}^{\mathrm{b}}(\boldsymbol{x}_i)-h_{\mathrm{s}}^{\mathrm{r}}(\boldsymbol{x}_i))}\big)} \sum_{p \in \{k_1,k_2,k_3\}} \eta_{\mathrm{s}}^{\mathrm{r}}(\boldsymbol{x}_p)\beta_p.$$